

AN ABSTRACT OF THE THESIS OF

Brian D. Wichner for the degree of Doctor of Philosophy in Physics presented on June 16, 1998. Title: Conversion of Laser Phase Noise to Amplitude Noise in a Lummer-Gehrcke Interferometer and in Oxygen Gas.


Redacted for Privacy

Abstract Approved: _____

Cliff E. Fairchild

In order to observe laser phase noise, this noise must be converted to amplitude noise, which can be achieved using either an interferometer or an absorption resonance in an atomic/molecular vapor or gas. When phase noise is converted to amplitude noise, it is manifested as a heterodyne signal in the output of an optical square-law detector. Thus, phase noise is measured by optical heterodyne spectroscopy, or, equivalently, laser phase noise spectroscopy.

In recent work on diode laser noise spectroscopy of rubidium and oxygen, the observed spectroscopic lineshapes were not in total agreement with theoretical predictions. We have repeated the previous work on the oxygen A-band transitions, and we now find qualitative agreement with theory.

In addition, we have measured the diode laser noise spectrum of a Lummer-Gehrcke interferometer (LGI), comparing the heterodyne lineshape of a LGI transmission spectrum with a qualitative theory that we develop in this thesis.

A theory, from other workers, predicts the intensity fluctuations from a Doppler-broadened, two-level atomic/molecular system driven with a phase-diffusing laser field. We show that a simplified version of this theory, which ignores Doppler effects of the system, is a useful approximation to the complete theory, by comparing computer-generated heterodyne lineshapes of each, for a rubidium transition. We apply this approximate theory to an oxygen A-band transition, and compare these results with our experimental measurements.

For the experimental arrangement used in the present work, diode laser noise spectroscopy may also include effects of selective reflection, which is dealt with experimentally and theoretically.

Diode laser phase noise has practical importance in optical communications and atomic clocks.

Conversion of Laser Phase Noise to Amplitude Noise in a Lummer-Gehrcke
Interferometer and in Oxygen Gas.

By

Brian D. Wichner

A THESIS

Submitted to

Oregon State University

in partial fulfillment of
the requirements for the
degree of
Doctor of Philosophy

Presented June 16, 1998

Commencement June, 1999

Doctor of Philosophy thesis of Brian D. Wichner presented June 16, 1998

APPROVED:

Redacted for Privacy

Major Professor, representing Physics

Redacted for Privacy

Chair of Department of Physics

Redacted for Privacy

Dean of Graduate School

I understand that my thesis will become part of the permanent collection of Oregon State University libraries. My signature below authorizes release of my thesis to any reader upon request.

Redacted for Privacy

Brian D. Wichner, Author

Table of Contents

	Page
1. Introduction	1
1.1 Introduction and Background	1
1.2 Diode Laser Heterodyne Spectroscopy	2
1.3 Thesis Outline	4
2. Basic Principles and Theory of Diode Lasers	5
2.1 Introduction to Diode Lasers	5
2.2 Wavelength Tuning	8
2.3 Diode Laser Models	9
2.4 Optical Feedback	11
2.5 Diode Laser Noise	12
2.5.1 Diode Laser Noise Models	13
2.5.2 Types of Diode Laser Noise	14
2.5.3 Relaxation Oscillations and the Diode Laser Power Spectrum	19
3. Theory of Diode Laser Phase Noise and its Conversion to Amplitude Noise	23
3.1 Introduction	23
3.2 Mathematical Description of Phase Modulation	33
3.3 Using a Lummer-Gehrcke Interferometer to Measure Laser Phase Noise	37
3.3.1 Motivation	37
3.3.2 Lummer-Gehrcke Interferometer	38

Table of Contents (Continued)

	Page
3.4 Lummer-Gehrcke Heterodyning	42
3.5 Heterodyning with an Atomic/Molecular Vapor or Gas	43
3.5.1 Introduction	43
3.5.2 Heterodyne Theory for a Diode Laser Emission Obeying the Phase-Diffusing Model	46
3.6 Selective Reflection as a Possible Source of Optical Feedback	51
3.7 (Optional) Heterodyne Detection and the Correlation Function	54
4. Experimental Techniques	57
4.1 Diode Lasers	57
4.2 Diode Laser Mounting and Temperature Control	59
4.3 Optical Layout Including L Gl and the Oxygen Cell	60
4.4 Detector Circuit	66
4.5 Diode Laser Drive Circuit	68
4.6 Computer Control	71
4.7 Spectral Scanning Method	73
4.8 Radio Frequency Spectrum Analyzer	75
5. Experiment Results	80
5.1 Lummer-Gehrcke Interferometer Heterodyne Spectra	80
5.1.1 NIR Diode Laser Spectra	80
5.1.2 Visible Diode Laser Spectra	85

Table of Contents (Continued)

	Page
5.2 Oxygen Heterodyne Spectra	88
5.3 Oxygen Spectra for the case of a Diode Laser with Intentional Fresnel Feedback	103
5.4 Spectra of Diode Laser with Unintentional Fresnel Feedback	105
6. Summary and Conclusion	112
Bibliography	116
Appendices	119

List of Figures

Figure		Page
2.1	AlGaAs-type diode laser chip structure	5
2.2	Schematic view of the light output power versus current characteristics of a diode laser	7
2.3	760 nm diode laser emission spectrum showing primary and secondary modes.	10
2.4	RIN spectra for a GaAlAs diode laser, driven at 20% above threshold	15
2.5	Measured RIN of a GaAlAs diode laser versus drive current	17
2.6	Frequency noise spectra for a typical GaAlAs diode laser	18
2.7	Spectral lineshape calculated for a single-mode diode laser operating at 0.5 mW and 1 mW	22
3.1	Phasor representation of a) amplitude modulation, and b) frequency modulation.	27
3.2	Frequency-domain representation of the rotating vectors in Figure 3.1	29
3.3	Carrier and sidebands tuned across an absorption line	31
3.4	Carrier and sidebands for single-tone frequency modulation	35
3.5	Carrier and sidebands for simultaneous frequency and amplitude modulation	36
3.6	Lummer-Gehrcke Interferometer	38
3.7	LGI output spectra for several values of exiting beam number, calculated using equation 3.23.	41

List of Figures (Continued)

Figure		Page
3.8	Calculated transmission spectrum of oxygen	45
3.9a	Calculated heterodyne peak height and central minimum height of Rubidium with and without Doppler integration, versus spectrum analyzer frequency.	49
3.9b	Calculated heterodyne FWHM and center width of Rubidium with and without Doppler integration, versus spectrum analyzer frequency.	50
3.10	Schematic of selective reflection versus detuning	51
3.11	Graphical depiction of directional differences between specular and selective reflection	52
4.1	Schematic description of experimental apparatus, showing LGI	61
4.2a	Scheme used to monitor, in real-time, the emission spectrum of the diode laser	61
4.2b	Two examples of monitor output of the apparatus shown in Figure 4.2a. An emission spectrum for a 670 nm and a 760 nm diode laser is shown in the left and right figure, respectively.	62
4.3	Oxygen gas cell details	64
4.4	Measured transmission spectrum of LGI.	65
4.5	Photodetector description of apparatus circuit	67
4.6	Drive circuit for diode laser	69
4.7	Half a heterodyne lineshape showing spectral drift when the measurement process was paused for 500 seconds	76
4.8	Radio frequency spectrum analyzer	77
5.1	LGI heterodyne spectrum of the 760 nm diode laser	81
5.2	Diode laser emission spectra for heterodyne data of Figure 5.1	82

List of Figures (Continued)

Figure		Page
5.3	Apparatus used for measuring diode laser amplitude noise	83
5.4	Amplitude noise spectrum for a 670 nm diode laser, operating at a power level of 6.6 mW	84
5.5	Heterodyne spectra for a 670 nm diode laser, for two emission power levels	86
5.6	Diode laser emission spectrum for the case of Figure 5.5	87
5.7	Heterodyne spectrum showing two oxygen transitions, as noted in the figure	90
5.8	Previously reported heterodyne spectra for oxygen	92
5.9	Comparison of theory and experiment for heterodyne peak height	95
5.10	Comparison of theory and experiment for heterodyne FWHM	96
5.11	Comparison of theory and experiment for heterodyne center width	98
5.12	Comparison of theory and experiment for heterodyne central minimum height	99
5.13	Heterodyne lineshape peak height asymmetry	100
5.14	Apparatus for testing the presence of selective reflection effects	102
5.15	Amplitude noise spectra for two drive current values, of a 760 nm diode laser, subjected to optical feedback	104
5.16	Heterodyne lineshape of 760 nm diode laser with optical feedback	106
5.17a	Heterodyne lineshapes of oxygen with a relatively small amount of diode laser optical feedback	109
5.17b	Heterodyne lineshapes of oxygen with an increasing amount of diode laser optical feedback	109

List of Figures (Continued)

Figure		Page
5.17c	Heterodyne lineshapes of oxygen with slightly more diode laser optical feedback than in Figure 5.17b	110
5.17d	Heterodyne lineshapes of oxygen with slightly more diode laser optical feedback than in Figure 5.17c	110
5.17e	Heterodyne lineshapes of oxygen with slightly more diode laser optical feedback than in Figure 5.17d	111
5.17f	Heterodyne lineshapes of oxygen with slightly more diode laser optical feedback than in Figure 5.17	111

List of Appendices

	Page
A Lummer-Gehrcke Interferometer	120
A.1 Angle of Incidence of LGI	120
A.2 LGI Free Spectral Range	122
B LGI n-Beam Case	124
C Computer Program	133

List of Appendix Figures

Figure		Page
A.1	LGI angles	123
A.2	LGI free-spectral range versus plate thickness	124

Conversion of Laser Phase Noise to Amplitude Noise in a Lummer-Gehrcke Interferometer and in Oxygen Gas.

CHAPTER 1: INTRODUCTION

1.1 Introduction and Background

In previous work on diode laser noise spectroscopy of rubidium [McIntyre, et al., 1993] and O₂ [Fairchild, et al., 1993], the lineshapes observed by optical heterodyne spectroscopy were not in total agreement with theoretical predictions [McIntyre, et al., 1993, and Fairchild, et al., 1993]. We have repeated the previous work on the O₂ A-band transitions and we now find qualitative agreement with theory.

Several recent experiments have involved the use of stabilized tunable diode lasers to excite $X^3\Sigma_g^- \leftrightarrow b^1\Sigma_g^+$ (A-band, 760-70 nm) transitions in the O₂ molecule [Kroll, et al., 1987, Ritter, et al., 1987, Fairchild, et al., 1993, Goldstein, et al., 1993, McLean, et al., 1993, de Angelis, et al., 1996, Hilborn, et al., 1996, and Takubo, et al., 1996]. These transitions are forbidden by electric dipole selection rules, and are found to be magnetic dipole transitions [Garstang, 1962]. In all but two [Fairchild, et al., 1993, and McLean, et al., 1993] of these experiments, conventional absorption of laser light intensity was measured. However, in the earlier O₂ A-band work of Fairchild, et al., and McLean, et al., the principal quantity measured was the signal due to heterodyning between the laser center frequency component and its frequency noise sidebands. The resultant beat

frequency signal is also referred to as "conversion of phase noise to intensity noise" [Camparo, 1998]. The present experiment extends earlier investigations to include detailed measurements of heterodyne lineshapes. The oxygen A-band transitions are two-level transitions, as opposed to the multilevel nature of the rubidium transitions investigated in the work of McIntyre, et al. [1993]. The heterodyne theory developed using a phase diffusing field model (PDM) of laser noise [Anderson, et al., 1990] assumes a two-level transition. If a multilevel atom or molecule is involved then the effects of optical pumping must be considered [McIntyre, et al., 1993]. The emission of the diode laser used for oxygen measurements is expected to contain phase noise (frequency noise), but comparatively small intensity noise [Yabuzaki, et al., 1991]. Our heterodyne spectra measurements with oxygen provide a good test of the PDM heterodyne theory. We also perform heterodyne spectroscopy with a nonconventional interferometer, namely a Lummer-Gehrcke interferometer.

1.2 Diode Laser Heterodyne Spectroscopy

Several years ago, a new type of high-resolution spectroscopy, using a diode laser, was reported [Yabuzaki, et al., 1991]. In the course of using a diode laser for simple absorption spectroscopy, it was observed that the diode laser beam became noisy when it was transmitted through a resonant vapor. This excess noise had also been observed by other workers [Haslwanter, et al., 1988, and Ritsch, et al., 1990]. It was noted [Yabuzaki, et al., 1991] that the diode laser was very stable even during the excess noise events. Thus, this intensity noise was

found to be a response of the atoms to the laser field. Generally, the amount of the intensity noise in the emission of a diode laser is very low compared with its phase noise. The resonant medium through which the laser beam propagates, converts phase noise to intensity noise [Yabuzaki, et al., 1991, and Camparo, 1998]. The process of this conversion is the basis for heterodyne spectroscopy. If the frequency of the laser field is near that of a resonance transition of an absorbing vapor or gas, particularly where the absorption profile has the largest slope, the phase noise of the laser field will cause rapid variations of the intensity of the transmitted light. This intensity variation is understood by realizing that a laser field, with phase noise, can be considered to undergo random changes of frequency, so that the field rapidly jumps in and out of resonance with the absorbing medium. In a very simple case the laser frequency would change abruptly from its central value to a value resonant with the atomic medium. During the short time the field is resonant with the medium, an atomic coherence, equivalent to an induced macroscopic polarization, is induced in the medium. The laser frequency then jumps back to its central value, and the atomic polarization then decays at a rate determined by the dephasing time for the transition of the resonance. The laser field, and the forward radiation field from the induced dipole moment, each at a different frequency, will co-propagate and mix on the surface of a square-law photodetector, which measures the intensity of the total mixed field. The intensity varies at the difference (beat) frequency of the laser and the dipole field. This frequency, typically in the radio-frequency regime, is measured by a radio frequency spectrum analyzer (RFSA).

Heterodyne spectroscopy has been performed by externally introducing a phase modulation to a laser [Bjorkland, et al., 1983, Silver, 1992, and Elliott, et al., 1988]. When the intrinsic phase noise of the diode laser is utilized, the complete term to describe the latter situation may be "diode laser noise heterodyne spectroscopy".

1.3 Thesis Outline

Chapter 2 begins with an introduction to diode lasers. A description is given of the characteristics of diode laser noise. The noise model of the diode laser, the phase diffusion model, is introduced. In Chapter 3, an introduction is given to the mathematical description of amplitude and phase modulation, and how this description relates to the noise of the diode laser. A Lummer-Gehrcke interferometer is introduced and described. Heterodyne interferometry is discussed in terms of the Lummer-Gehrcke interferometer and an atomic resonant medium. Heterodyne theory based on the phase diffusion model for the laser field is described. Finally, a brief description of selective reflection is given.

Chapter 4 describes all the aspects of the experimental techniques and the apparatus. Details of the equipment used are given. Chapter 5 summarizes the experimental results, and compares these with the theory described in Chapter 3. Chapter 6 summarizes the activities and results of this thesis.

CHAPTER 2: BASIC PRINCIPLES AND THEORY OF DIODE LASERS

2.1 Introduction to Diode Lasers

Diode lasers, often called semiconductor lasers, basically consist of a p-n junction with an optically transparent active region where electronic recombination occurs. For a diode laser, the active region is also an optical cavity where photons are created during this recombination process. Figure 2.1 is a

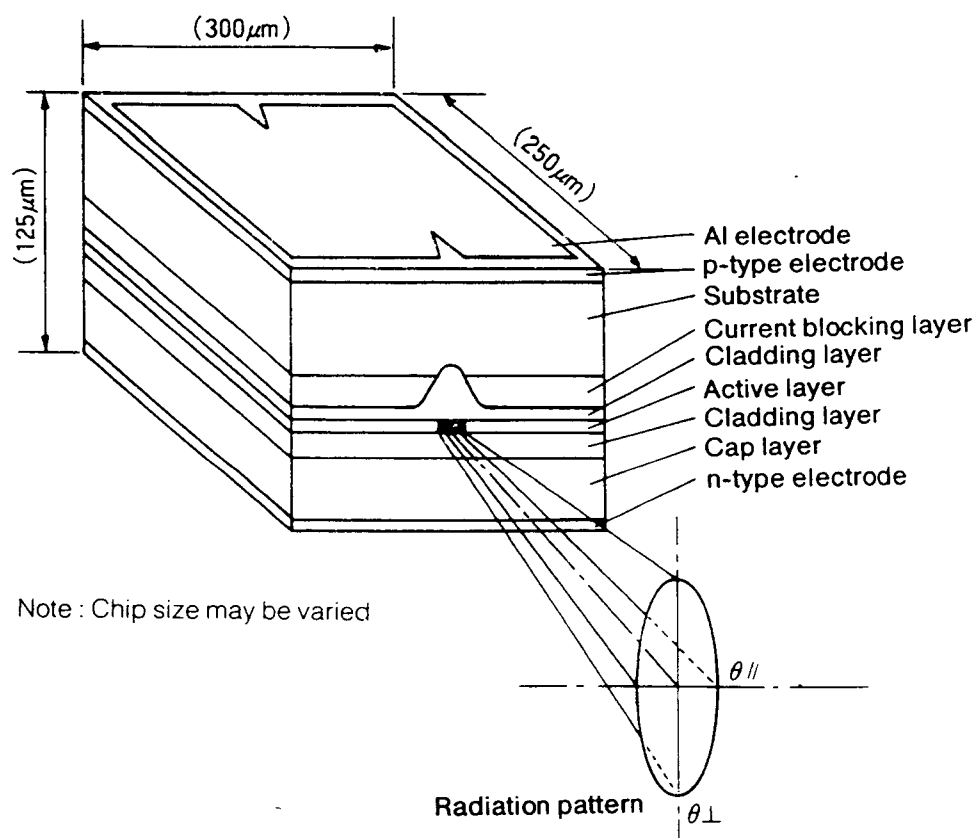


Figure 2.1 AlGaAs-type diode laser chip structure (Sharp Corp., Laser Diode User's Manual, 1988)

schematic of the diode laser chip structure, showing details of the composite materials and the radiation pattern. This cavity, by way of multiple reflections of light from the end-faces (facets), and stimulated emission by electron-hole pairs, produces the amplification necessary for lasing. The lasing radiation is emitted at both facets of the cavity, which are cleaved plane surfaces of the semiconductor. The rear facet of the optical cavity emits part of the total radiation, which impinges on a built-in photodiode. This photodiode can be utilized as an indicator of real-time lasing intensity.

The front facet of the cavity is the "working end" of the diode laser. The radiation is emitted from this very small-dimension surface, causing this radiation to diffract through a relatively large angle, necessitating the use of collimating lenses.

For most of our work, we used AlGaAs-type diode lasers. An InGaAlP-type visible diode laser was also used. Both types of lasers are a heterojunction structure, and operate on the index-guided principle. These two types of lasers have similar characteristics, therefore, only AlGaAs-type lasers are explicitly mentioned in the following discussion.

For the AlGaAs-type diode lasers, some general numbers that are useful can be realized: A typical diode laser cavity is about 0.3 mm long. The index of refraction of the cavity is approximately 3.6. The reflectivity of the cavity end-faces may be around 30 percent, depending on whether anti-reflection coatings are applied. The linewidths of free-running diode lasers are typically in the range from 10 to 100 MHz.

A very important characteristic of a diode laser is its threshold current value, I_{th} . Drive currents below I_{th} are not sufficient to maintain a minimum carrier density required for lasing. These low currents will result in emitted light from the cavity, but this light is merely a result of spontaneous emission, as for the case of light-emitting diodes. The coherent, intense quality of laser emission is only achieved when the current is above I_{th} . Beyond this threshold the light power rapidly increases linearly with increasing drive current, as shown in Figure 2.2. A common value for the slope of the stimulated emission part of the curve is 0.5 mW/mA.

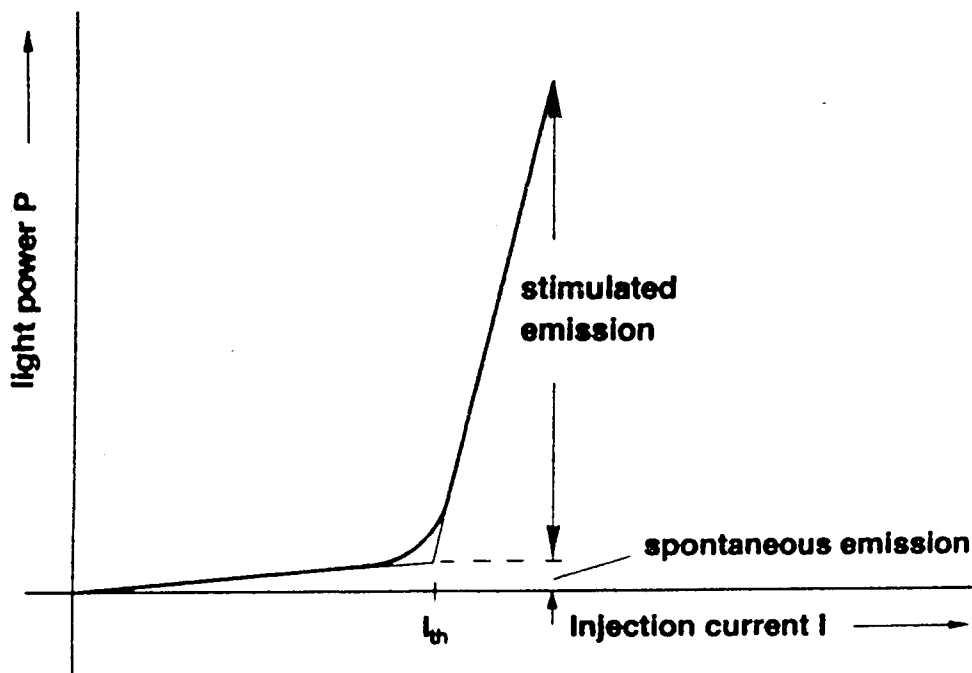


Figure 2.2 Schematic view of the light output power versus current characteristics of a diode laser (Petermann, 1988).

2.2 Wavelength Tuning

AlGaAs-type diode lasers are readily available in many wavelengths, over the range of approximately 635 nm to 1000 nm. The diode laser bandgap is engineered for a specific target wavelength by varying the type and amount of material alloyed to the basic GaAs crystal. Typically, this target wavelength is reached only within a few nanometers for each specific diode laser that is built. Subsequently, each diode laser can be fine-tuned to a more precise wavelength by adjusting the diode laser current, temperature, or both. Conversely, a stabilized wavelength is only achieved by careful control of the temperature and current. Roughly speaking, the change in frequency per change on temperature is -20 GHz/K . The change in frequency per change in drive current is -3 GHz/mA .

The diode laser wavelength's dependence on temperature is due to the temperature-dependence of the optical path length of the cavity. Also, temperature affects the wavelength-dependence of the gain curve. These two temperature dependencies are very different from each other. For AlGaAs-type lasers, the optical path length changes about 0.06 nm/K , while the gain curve changes about 0.25 nm/K [Wieman, et al. 1991]. This temperature-dependence mismatch results in, unfortunately, discontinuous wavelength tuning with temperature. The spectrally-shifting gain curve creates these discontinuities when the laser jumps from one longitudinal mode to the next. These jumps are called mode-hops, and they are discussed in the next section.

Diode laser wavelength is tunable by current because the current affects the diode laser temperature. Also, the current directly affects the diode laser's carrier density, which affects the cavity's index of refraction, resulting in changes to the cavity's optical path length.

2.3 Diode Laser Modes

Several laser modes exist within the gain curve of a diode laser. The distribution of the intensity of the lasing modes depends on the spectral location of the modes relative to the gain curve. A single-mode diode laser has a narrow gain curve that ideally supports only one mode. In reality, more than one mode will be present in the emission of any real laser.

Figure 2.3 is an example of an emission spectrum of a 760 nm, index-guided diode laser, sold as a single-mode device. For this spectrum, the operating conditions of the laser were less than ideal resulting in secondary modes that are clearly observable. The frequency separation of these modes is the free spectral range (FSR) of the diode laser. The FSR is given by $\Delta\nu = c/2nL$, where c is the speed of light, n is the index of refraction of the cavity, and L is the length of the cavity. The FSR of diode lasers usually lies in the range of 50 - 150 GHz.

The ratio of the magnitude of the intensity of the primary mode to the intensity of the second-most intense mode, is called the side-mode-suppression ratio (SMSR). The value of this ratio indicates whether the laser is a "good" single-

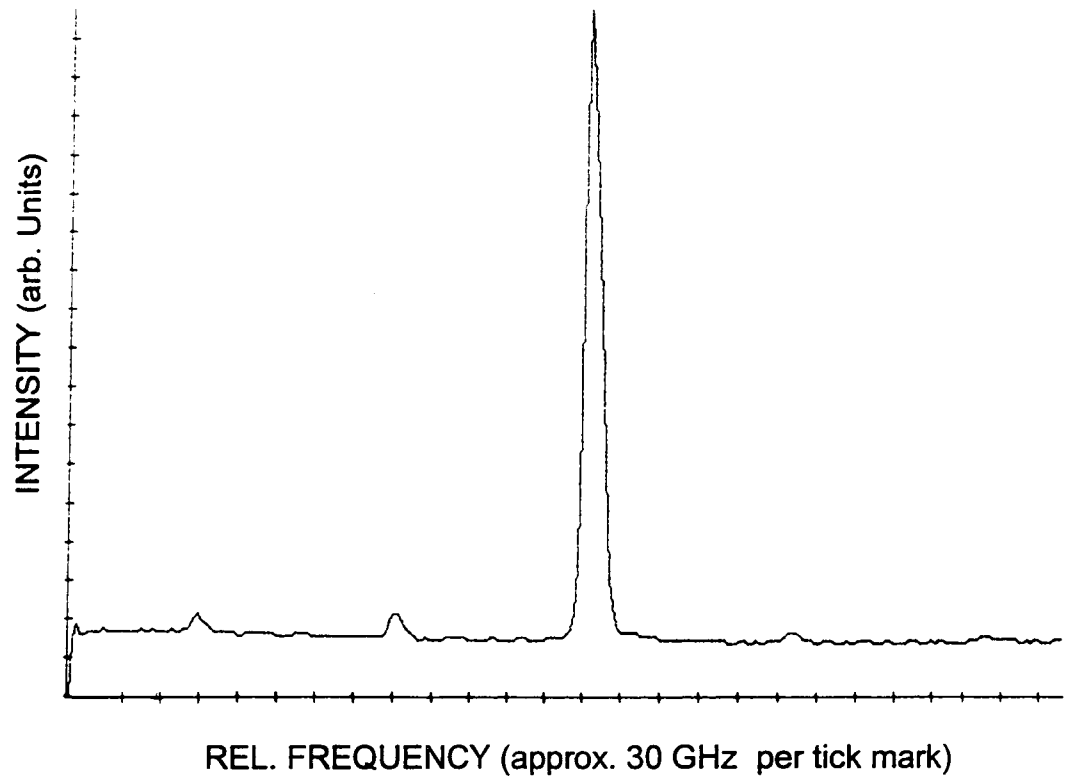


Figure 2.3 760 nm diode laser emission spectrum showing primary and secondary modes. The free spectral range is 150 GHz.

mode laser. Good single-mode diode lasers may have a SMSR as high as 100. For our experiments, as will be seen in Chapters 4 and 5, we operate the 760 nm diode laser, of Figure 2.3, in a single mode, with an SMSR of approximately 60.

After consideration of the single mode lasing characteristics, one must be aware that this single mode operation is highly dependent on a current and temperature combination, for reasons explained in the previous section. Indeed, a single mode oscillation will quickly digress to a multimode condition with perhaps only a slight change in the diode laser's drive current, temperature, or

both. Then after a bit more change in this current and/or temperature, the laser may once again operate in a (quasi) single-mode. This latter mode may be at a different wavelength than the first. If so, then what has been described is a mode-hop. Mode-hops may be jumps of one or more than one FSR of the laser. These jumps greatly inhibit the usefulness of diode laser's wavelength tuning utility, since the wavelength ranges within these jumps may not be accessible. These wavelength-tuning gaps are unique for each specific laser. Thus sheer luck plays a large part in the procurement of these lasers for many wavelength-specific experiments.

In addition to mode-hops, the diode laser may lase with comparable intensity in two modes simultaneously. This condition is normally unstable, and is usually the transient condition of a mode-hop, but with careful control of laser current and temperature, two-mode operation can persist indefinitely.

2.4 Optical Feedback

Optical feedback of the laser field into the laser cavity has significant consequences for the operation of the diode laser. These consequences may be beneficial or detrimental. Quite often, carefully controlled feedback is used to drastically narrow the linewidth of the laser, operate on a specific laser mode, or tune to a specific frequency [Wieman, et al. 1991, Kitching, et al., 1994].

Unintentional feedback can dramatically degrade the spectral characteristics of the laser.

The literature [Tkach, et al., 1986, Petermann, 1988] classifies the relative magnitude of diode laser feedback into a four-regime hierarchy. Regime I is weak feedback that may broaden or narrow the spectral width, depending on the parameters of the feedback. Regime II may also result in line narrowing, but in general, mode hopping and multiple cavity modes will exist. Regime III is similar to regime II, but there is more feedback, and greater line narrowing. Finally, diode laser operation in regime IV guarantees highly degraded optical performance, with spectral linewidths the order of 10 GHz with very large amounts of intensity noise.

2.5 Diode Laser Noise

The spectral emission of diode lasers has neither constant frequency nor constant intensity. The coherence length may be as short as a meter, depending on many factors, including current and temperature stability of the diode laser, mode stability, and the factors mentioned earlier in this chapter. Even under ideal operating conditions, the diode laser emission contains noise. For this ideal case, the primary source of noise originates from spontaneous emission, producing both intensity and frequency fluctuations.

2.5.1 Diode Laser Noise Models

This section gives a brief review of the various statistical models of diode laser noise found in the literature [See, for example, Raymer, et al., 1979, Elliott, et al., 1988, Georges, 1980, Dixit, et al., 1980, and Ritsch, et al., 1990]. The work of this thesis is only concerned with the phase-diffusion field model (PDM), described below. For completeness, other models are briefly described, namely, the thermal/chaotic field model, and the real Gaussian field model.

For a diode laser exhibiting only phase noise (no amplitude noise) the laser E-field may be represented by the equation

$$E(t) = (1/2)E_0 \exp[-i\omega_0 t + i\phi(t)], \quad 2.1$$

where ω_0 is a well-defined center frequency, $E_0 \exp[-i\phi(t)]$, E_0 is a constant, and $\phi(t)$ is a fluctuating phase. For the PDM, $\phi(t)$ is a Gaussian random variable, with zero mean, giving a field correlation function,

$$\langle E(t_1)E(t_2) \rangle = E_0^2 \exp[-\Gamma(t_1 - t_2)], \quad 2.2$$

where Γ is the laser linewidth. The thermal/chaotic field model [Mollow, 1968] takes the amplitude to be a complex random variable, with the phase being constant. This model is closely approached by the radiation from a thermal source of independent oscillators, or the radiation generated by a laser operating on several independent modes. The real Gaussian field model [Elliott, et al., 1988] is similar to the thermal/chaotic model, but the amplitude is considered a real Gaussian variable.

2.5.2 Types of Diode Laser Noise

As mentioned above, diode lasers often emit light in more than a single mode. Even so-called single mode lasers under optimum conditions will have a finite amount of power distributed into secondary modes. Each of these lasing modes has its own intensity noise characteristics, and so it is important to know whether the full laser spectrum is detected or just a single mode. Ironically, the intensity noise of the superposition of all the modes is usually a great deal smaller than the noise for only a single mode. This situation is referred to as mode partition noise [Petermann, 1988].

In order to explain the significance of mode partition noise, a quantity is defined that relates intensity noise power to the mean power of the laser. This quantity is called the relative intensity noise, or RIN. An example of mode partition noise, in terms of the RIN, for a quasi single-mode laser, is shown in Figure 2.4 [Petermann, 1988]. For this diode laser, with a SMSR of more than 20, driven 20% above threshold, the RIN of the dominant mode alone is very high at the lower frequency-end of the spectrum. The RIN decreases more than three decades towards the higher frequency end of the spectrum. The RIN of the total (all modes) laser emission trends the other way, starting with a rather small RIN at the lower end of the spectrum. Thus the laser would have to be considered to have a much higher RIN for applications that only utilized the dominant mode. For instance, in spectroscopy, the dominant mode may be tuned within the

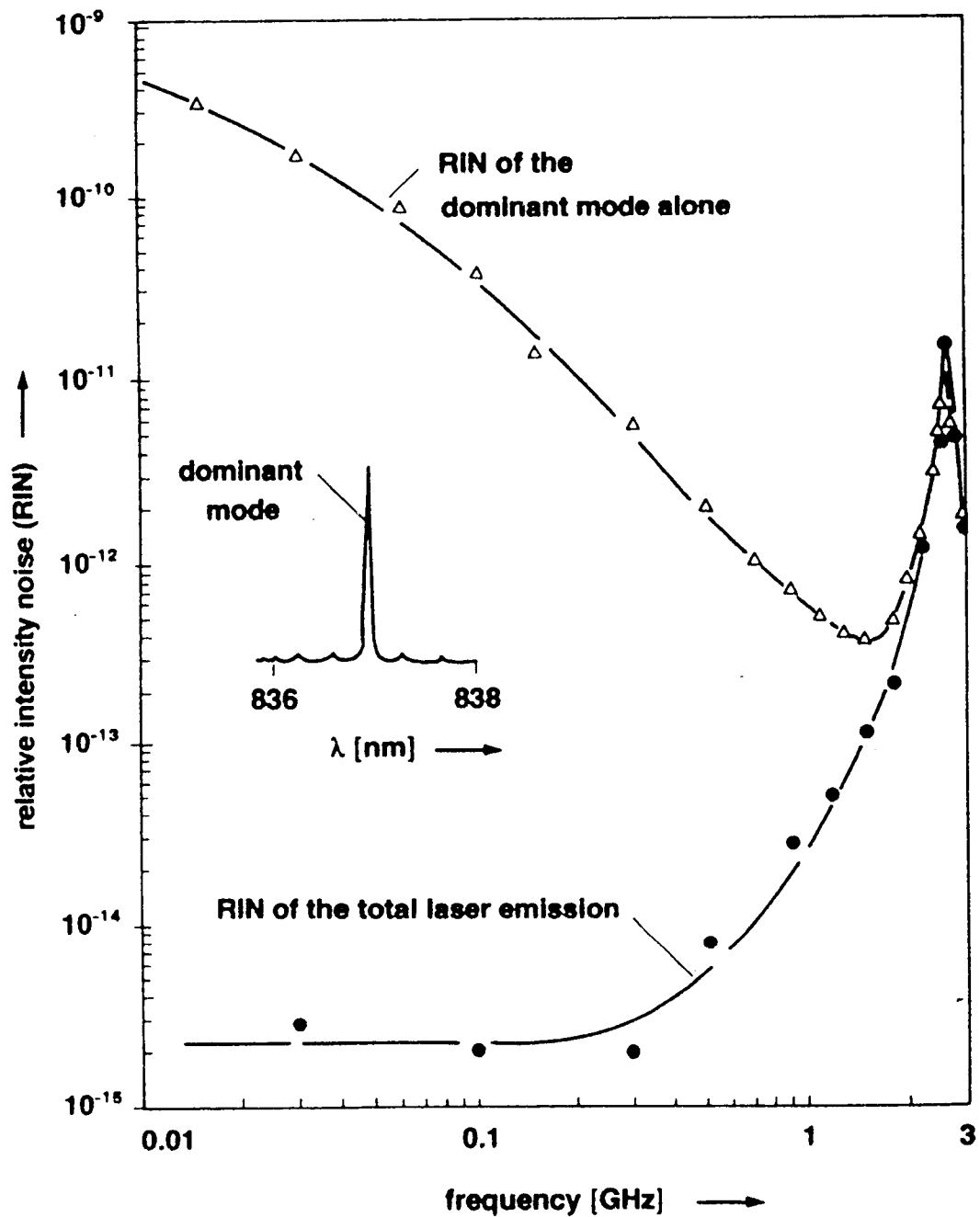


Figure 2.4 RIN spectra for a GaAlAs diode laser, driven at 20% above threshold. The side-mode intensity is less than about 5% of the dominant mode (Petermann, 1988).

absorption envelope of an atomic transition but the secondary modes would be completely detuned from the line by perhaps 150 GHz.

If the SMSR is relatively high, then the lower curve in Figure 2.4, describing the total laser emission, can be used to describe the diode laser emission, even if only the dominant mode is considered.

The total (integrated across the frequency spectrum) RIN varies greatly with the drive current of the diode laser. A maximum RIN is reached at a drive current slightly greater than the threshold current. Then as the current is increased, the RIN decreases several orders of magnitude as soon as the drive current increases to one and a half times threshold, shown in Figure 2.5.

Frequency noise is more prevalent than intensity noise under steady-state operating conditions for the 760 nm diode laser used in the experiments. The frequency noise almost entirely determines the spectral linewidth [Yabuzaki, et al., 1991], for noise spectra far from the relaxation oscillation frequency, first described in the following section. The frequency noise spectrum for a typical diode laser is shown in Figure 2.6 [Yamamoto, 1991]. The local maxima are relaxation oscillations.

Both frequency and intensity noise are essentially introduced by the same spontaneous emission noise events, thus it follows that they are highly correlated [Petermann, 1988]. However, this is not the case for diode lasers experiencing an increased level of noise due to feedback. In this case the resulting "noise" from the feedback is actually a manifestation of rapid fluctuations of the power spectrum of the laser. This does not give rise to a high level of correlation

between frequency and intensity modulation, though the feedback simultaneously increases both.

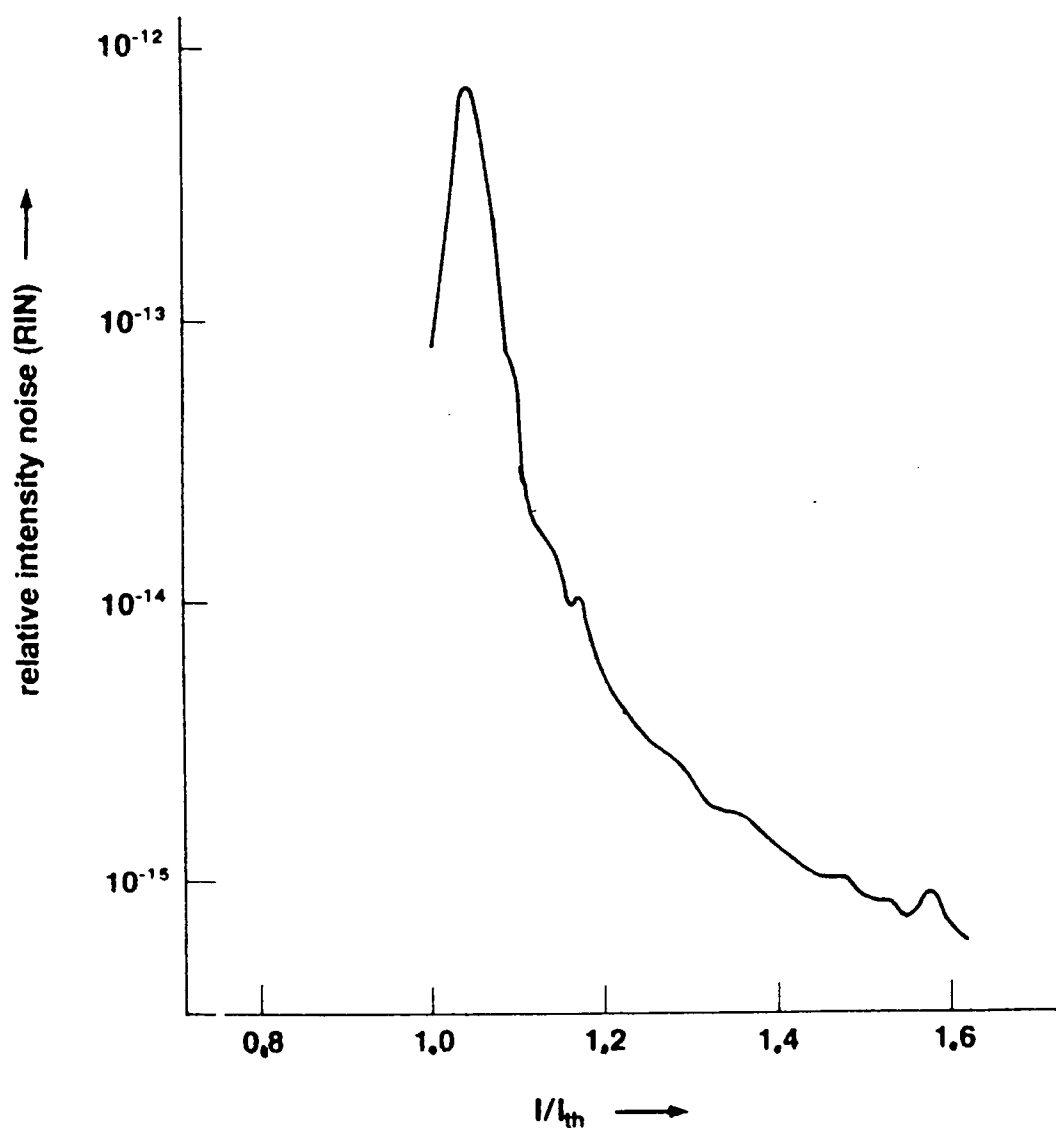


Figure 2.5 Measured RIN of a GaAlAs diode laser versus drive current (Petermann, 1988).

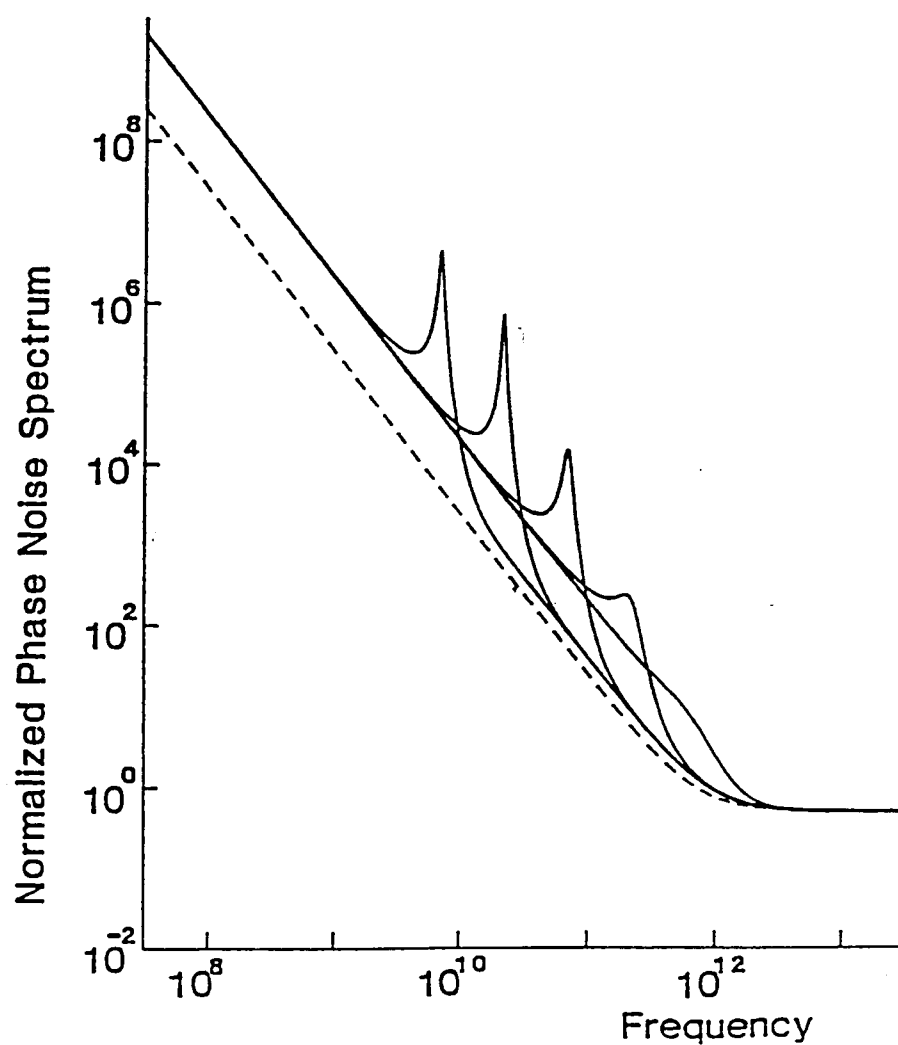


Figure 2.6 Frequency noise spectra for a typical GaAlAs diode laser. The solid curves show different cases of drive current, and the dashed curve is similar to the behavior of a diode laser obeying the phase diffusing model (Yamamoto, et al., 1991)

2.5.3 Relaxation Oscillations and the Diode Laser Power Spectrum

For the diode laser, the two quantities of interest are the number of photons in the cavity, S , and the number density of carriers, n . Two rate equations for these quantities are [Petermann, 1988],

$$\frac{dS}{dt} = S(R_{st} - \tau_{ph}^{-1}) + R_{sp} \quad 2.3$$

and,

$$\frac{dn}{dt} = \frac{I}{eV} - R(n) - \frac{R_{st}}{V} S \quad 2.4$$

where R_{sp} is the number of spontaneously generated photons per unit time of a given laser mode, τ_{ph} is the photon lifetime, R_{st} is a stimulated emission coefficient, $R(n)$ is the recombination rate, I is the injection current, and V is the volume of the active region.

Since the spontaneous emission noise exists across a large frequency range, it can be considered to be a white noise source. A Gaussian distribution may be used to describe its spectral probability density. Equation (2.3) is modified to account for this noise source by adding a term, $F(t)$, that represents a Langevin noise source with zero mean value;

$$\frac{dS}{dt} = S(R_{st} - \tau_{ph}^{-1}) + R_{sp} + F(t) \quad 2.5$$

Laser linewidth varies inversely with output power as predicted by the modified Schawlow-Townes formula [Schawlow, et al., 1958]. However, this power dependence for diode lasers must be modified further by the simple multiplicative factor $(1+\alpha^2)$, where α is called the linewidth enhancement factor [Henry, 1982]. α is defined as the ratio of real refractive index fluctuations to imaginary refractive index fluctuations in the active region. Henry showed that the increased linewidth is due to the strong coupling between phase and intensity noise.

The diode laser linewidth is given by

$$\delta\nu = \frac{\pi\hbar\nu n_{sp}}{P_{tot}(2\pi\tau_p)}(1+\alpha)^2 \quad 2.6$$

where ν is the lasing frequency, τ_p is the photon lifetime in the cavity, P_{tot} is the total emission power, and n_{sp} is the spontaneous emission factor given by

$$n_{sp} = \{1 - \exp[(h\nu + E_v - E_c)/kT]\}^{-1} \quad 2.7$$

where E_v and E_c are the valence and conduction band quasi-Fermi levels, k is the Boltzmann constant, and T is the temperature [Cartaleva, 1994, and Fleming, et al., 1981].

The spectral lineshape of diode lasers includes sidebands first recognized as relaxation oscillations by Vahala, et al. [1983], and expressed as part of the spectral profile by van Exter, et al. [1992]. Relaxation oscillations (RO's) occur due to an initial perturbation in the number of carriers and/or photons in the laser cavity. Although RO's are a transient effect in gas lasers, they are a steady-state condition for diode lasers. If the carrier density momentarily exceeds a threshold value this will cause an excess of photons also exceeding a threshold. These extra photons consume enough carriers to reduce the carrier population to below the threshold level. This depleted condition of carriers results in a decreased number of photons to below the threshold value. Due to this lowered photon population the carrier density recovers enough to once again surpass the threshold value. This cycle repeats, resulting in a ringing at the relaxation oscillation frequency. RO frequencies are typically between 1.5 and 5 GHz.

The RO frequency increases with increasing drive current of the diode laser. Temperature decreases will also increase the RO frequency. The square of the RO frequency varies linearly with laser power, with a slope of approximately 2 GHz²/mW [van Exter, et al., 1992, Figure 6]. Also, higher-order RO's exist, but their intensity drops considerably from one order to the next. Agrawal, et al. [1993, Figure 6.14] determines the spectral lineshape of a diode laser using rather detailed expressions for the laser field. Figure 2.7 shows this result. Notice

the key feature is that the relaxation oscillation peaks move away from the central frequency as the laser power increases.

The fraction of power that is contained in the RO's varies greatly with the specific laser, feedback and other operating conditions. For example, Wieman, et al. [1991] has found this power fraction to be of the order of 1/1000 for near-infrared (NIR) diode lasers and as much as 1/10 for the relatively new visible diode lasers.

The RO peaks display an asymmetry in height; the low frequency RO peak is larger than the upper frequency peak. Vahala, et al. [1982] believed this asymmetry to be the result of the coherence between amplitude and phase fluctuations. The intensity of the RO peaks' asymmetry has been correlated with the linewidth enhancement factor α [van Exter, et al., 1992].

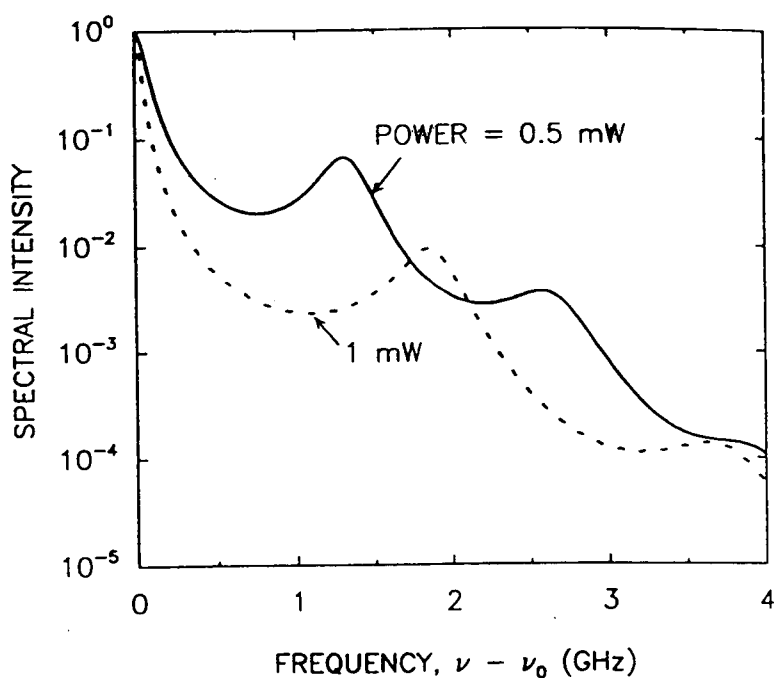


Figure 2.7 Spectral lineshape calculated for a single-mode diode laser operating at 0.5 mW and 1 mW (Agrawal, et al., 1993)

CHAPTER 3: THEORY OF DIODE LASER PHASE NOISE AND ITS CONVERSION TO AMPLITUDE NOISE

3.1 Introduction

In this chapter, we investigate the behavior of a diode laser field with phase noise as it propagates through an interferometer, or an atomic medium, during which the frequency of the laser is spectrally scanned across either a transmission resonance of the interferometer, or an absorption line of the medium. Specifically, we are interested in the spectral behavior of the intensity of the transmitted field, which is measured by a square-law photodetector.

In general, we may write our laser electric field as

$$E(t) = E_0(t) \cos[\omega_L t + \phi(t)] \quad 3.1$$

where ω_L is the laser center frequency, $\phi(t)$ is a time-dependent phase noise, and $E_0(t)$ is assumed to vary little in an optical period $2\pi/\omega_L$. The photodetector will, in general, measure an intensity which we separate into its time-independent and time-dependent parts. As explained in Chapter 4, we use a radio frequency spectrum analyzer (RFSA) to measure the time-dependent part of the intensity. Because optical frequencies are too high ($\sim 10^{14}$ Hz) for any detector to follow, any contributions to a time-dependent intensity must come from $E_0(t)$, $\phi(t)$, or both. In our work, $E_0(t)$, and $\phi(t)$ are the amplitude noise, and phase noise, respectively, of our diode laser. In Chapter 5, $E_0(t)$, and $\phi(t)$ are analyzed in the

frequency domain, which gives their spectra, primarily in the radio-frequency range (10^6 - 10^9 Hz).

As above, consider $E_0(t)$ and $\phi(t)$ to have frequencies in the radio frequency regime. By squaring equation 3.1, and taking the time-average over an optical period, as a square-law photodetector does when measuring intensity, we obtain $I(t) \sim (E_0(t))^2$. As long as $\phi(t)$ varies slowly during the optical period the factor $\phi(t)$ is not in this final result. This indicates that one can directly measure the time-dependence of $E_0(t)$, the amplitude noise, but not that of $\phi(t)$, the phase noise.

The 760 nm diode laser used for the primary experimental work described here should exhibit phase noise only [Yabuzaki, et al., 1991], and so we now set $E_0 = \text{constant}$. Since this phase noise cannot be measured directly, we must convert it into amplitude noise in order to detect it. There are several ways of performing this conversion, and the simplest way is using a two-beam interferometer, explained as follows.

The laser field, after passing through a two-beam interferometer, can be written

$$E(t, \tau) = E_0 \{ \cos[\omega_L t + \phi(t)] + \cos[\omega_L(t - \tau) + \phi(t - \tau)] \} \quad 3.2$$

where τ is the time delay of one beam relative to the other introduced by the interferometer, i.e., $\tau = \Delta L/c$, where ΔL is the optical pathlength difference between the two branches of the interferometer, and c is the speed of light.

Squaring and time-averaging equation 3.2 results in a time-dependent intensity due to the phase noise;

$$I_{\text{det}}(t, \tau) = I_0/2 \{1 + \cos[-\omega_L \tau + \Delta\phi(t, \tau)]\} \quad 3.3$$

where $\Delta\phi(t, \tau) = \phi(t) - \phi(t - \tau)$, and I_0 is E_0^2 . This process of mixing two fields with different phases, and thus converting phase noise to amplitude noise, is a type of heterodyne detection. In this thesis, this process will be called simply "heterodyning".

We now determine the heterodyne intensity, $I_{\text{det}}(t, \tau)$, as a function of the relative phase delay, $\omega_L \tau$, introduced by the interferometer. Using an angle-sum trigonometric identity, equation 3.3 becomes,

$$I_{\text{det}}(t, \tau) = I_0/2 \{1 + [\cos(\Delta\phi)\cos(\omega_L \tau) - \sin(\Delta\phi)\sin(\omega_L \tau)]\} \quad 3.4$$

Next, we expand $\cos(\Delta\phi)$ and $\sin(\Delta\phi)$,

$$I_{\text{det}}(t, \tau) = I_0/2 \{1 + [(1 - \Delta\phi^2/2! + \Delta\phi^4/4! - \dots)\cos(\omega\tau) + \\ - (\Delta\phi - \Delta\phi^3/3! + \Delta\phi^5/5! - \dots)\sin(\omega\tau)]\} \quad 3.5$$

Let us assume our laser is not very noisy so that $\Delta\phi$ is small. We then ignore all $\Delta\phi$ -terms which are higher order than one;

$$I_{\text{det}}(t, \tau) = I_0/2 \{1 + [\cos(\omega_L \tau) - \Delta\phi(t, \tau)\sin(\omega_L \tau)]\}. \quad 3.6$$

As ω_L is scanned, as described in the first paragraph of this section, the first two terms of equation 3.6 yield the characteristic two-beam interference pattern for a perfectly monochromatic light source, i.e., $\Delta\phi = 0$. When $\omega_L \tau = 2m\pi$, where m is an integer, an interferometer transmission maximum is obtained. At these values of ω_L the third term in equation 3.6 goes through zero, changing sign. However, a RFSA measures *magnitudes* of the Fourier components of $\Delta\phi$;

therefore, the signal measured by a RFSA is always positive definite, and simply vanishes when $\omega_L \tau = 2m\pi$. Thus, as the laser is tuned through an interferometer resonance, the RFSA signal yields a spectrum termed an “m-shape”.

We now treat the more general case of a multiple beam interferometer, or an atomic/molecular vapor or gas. To do so, we introduce the Fourier spectrum of the phase noise, $\Delta\phi(t, \tau)$. We first use a graphical representation to illustrate the character of the phase noise spectrum of the laser field, and in the following section we rigorously develop more general expressions of the noise spectra, modeling the noise as a modulation.

To obtain a graphical representation of phase modulation, we first examine the graphical representation of amplitude modulation. A single-frequency amplitude modulated laser electric field can be written

$$E_{AM}(t) = (1 + 2M\cos\Omega t)\cos\omega_L t \quad 3.7$$

where M is a modulation index (the factor 2 is for notational convenience), Ω is the modulation frequency and ω_L is the laser field central, or *carrier*, frequency. Rearranging equation 3.7,

$$E_{AM}(t) = \cos\omega_L t + M \cos[(\omega_L + \Omega)t] + M \cos[(\omega_L - \Omega)t] \quad 3.8$$

We can represent equation 3.8 graphically by using rotating vectors, or phasors, as in Figure 3.1a. The resultant phasor rotates with a constant angular velocity, ω_0 , but its magnitude varies cyclically.

A single-frequency phase modulated field can be written

$$E_{PM}(t) = \cos(\omega_L t + M \cos \Omega t) \quad 3.9$$

where M is a modulation index, and Ω is the modulation frequency. Equation 3.9 is much more complicated than equation 3.7, so we will start with the phasor representation in order to find a simplified expression for equation 3.9. At this point, we note that in order to implement the phasor representation for phase modulation, we have $\Omega \ll \omega_L$, and $M \ll 1$, as in our work. With these conditions on Ω and ω_L , the phasor representation is shown in Figure 3.1b. By inspection, it can be seen that this phasor picture is the same as the one in Figure 3.1a, for amplitude modulation, with the only difference being that one of the smaller phasors is flipped π radians. The resultant phasor of the two small phasors is

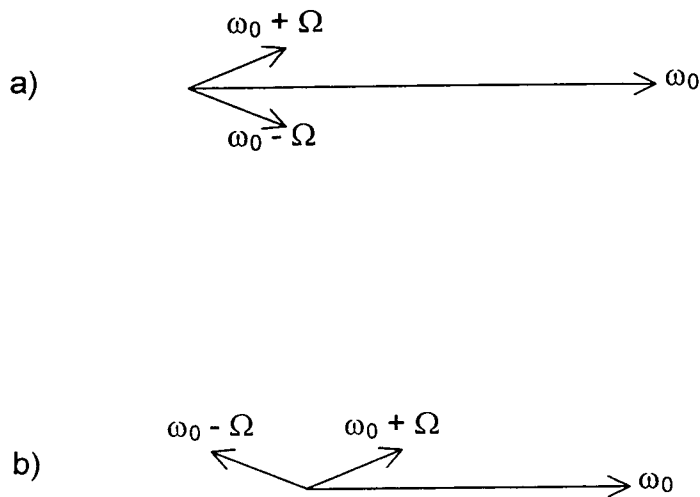


Figure 3.1 Phasor representation of a) amplitude modulation, and b) frequency modulation. These phasors are rotating vectors that rotate with the angular frequency noted on each vector.

orthogonal to the large phasor at all times. This orthogonality contributes to a cyclically varying angular frequency of the final resultant phasor. This is only an approximation based on the fact that Ω is much smaller than ω_0 , otherwise this phasor picture gives us simultaneous phase and amplitude modulation. However, with this approximation, the phasor representation of Figure 3.1b tells us that we can write equation 3.9 as

$$E_{PM}(t) = \cos\omega_L t + M_+ \cos[(\omega_L + \Omega)t] - M_- \cos[(\omega_L - \Omega)t] \quad 3.10$$

where the coefficients of the second and third term are labeled differently for generality (This is justified since equation 3.10 is based on the approximate phasor model in Figure 3.1b, whereas equation 3.8 is exact, so we have no leeway in assigning our choice of coefficients.). Here, M_+ and M_- are positive, constant amplitudes.

Equations 3.8 and 3.10 are represented in the frequency domain by the schematic model shown in Figure 3.2. The vertical lines represent the frequencies and magnitudes, including some phase information, of the Fourier components of the field. For instance, in Figure 3.2b, the central frequency component at ω_0 has the largest magnitude of the three terms shown, and is called the carrier frequency. The other two frequency components, at $\omega_0 + \Omega$ and $\omega_0 - \Omega$, are called the upper and lower sidebands, respectively. The lower sideband is shown to be equal in magnitude with the upper sideband, but these two fields differ in phase by π radians. The case in Figure 3.2a is similar, but both sidebands are in phase with each other. We relate this schematic model with equation 3.8 and 3.10 as follows. The carrier frequency is the first term of

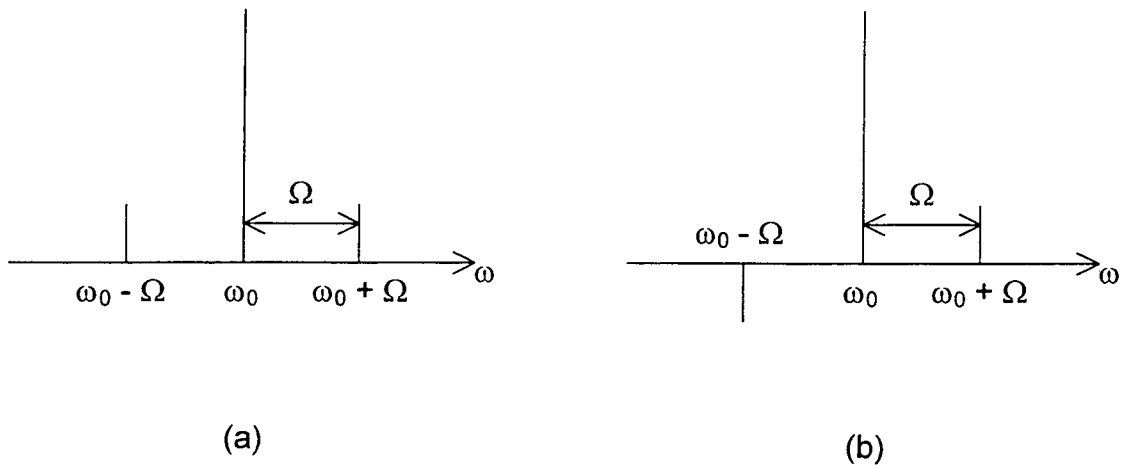


Figure 3.2 Frequency-domain representation of the rotating vectors in Figure 3.1, for a) amplitude modulation, and b) frequency modulation.

equations 3.8 and 3.10, with unity magnitude, and the upper and lower sidebands are the second and third term, respectively. The coefficients of the second and third terms, M_+ and M_- are equal. Equations 3.8 and 3.10 represent figures 3.2a and 3.2b, respectively.

The field of equation 3.8 is squared, and time-averaged by a detector, resulting in a heterodyne signal. However, squaring, and time-averaging the field of equation 3.10 gives a heterodyne signal of zero, as expected, since $M \ll 1$,

and we ignore terms involving M_+M_- , M_+^2 , and M_-^2 . However, if the coefficients, M_+ and M_- are no longer equal, then we will get a heterodyne signal. For instance, if the upper sideband is selectively transmitted through an interferometer, more than the lower sideband, then $M_+ > M_-$. This is the crucial principle underlying heterodyning detection.

In the remainder of this section, we show how a heterodyne m-shape is produced as the laser field frequency, represented by the carrier/sideband picture, is scanned across a resonance feature. We use the term “beating”, referring to the resultant difference frequency one gets when mixing two frequency fields.

The discrete, single-sideband model introduced above is useful because of how we measure the heterodyne signal; we use a RFSA that is set at a specific, tuned frequency, Ω . As above, to a first approximation (the character of this approximation is explained at the end of this section), we consider the laser field to consist of a principle, or carrier, frequency, and an upper and lower sideband. Each sideband is separated from the carrier by the frequency of the tuned spectrum analyzer, Ω . These three frequency bands will beat with each other as they are mixed on a photodetector. The possible beat combinations are the beating of the carrier with either of the two sidebands. It is important to note that the carrier will beat with both the upper and the lower sideband, and the beat frequency will be the same for both cases. However, there is an opposite phase between these two beats, since the upper and lower sidebands are out of phase by π radians. Opposite phase causes these sideband beats to cancel.

The upper part of Figure 3.3 depicts the carrier and a pair of sidebands as they are scanned across an atomic/molecular absorption line. The lower part of the Figure shows the resulting heterodyne lineshape at every point during the scan. We now explain how we arrive at this result.

As the laser field's frequency is adjusted so the three frequency bands begin to move into the absorbing feature, in Figure 3.3, the upper sideband will be

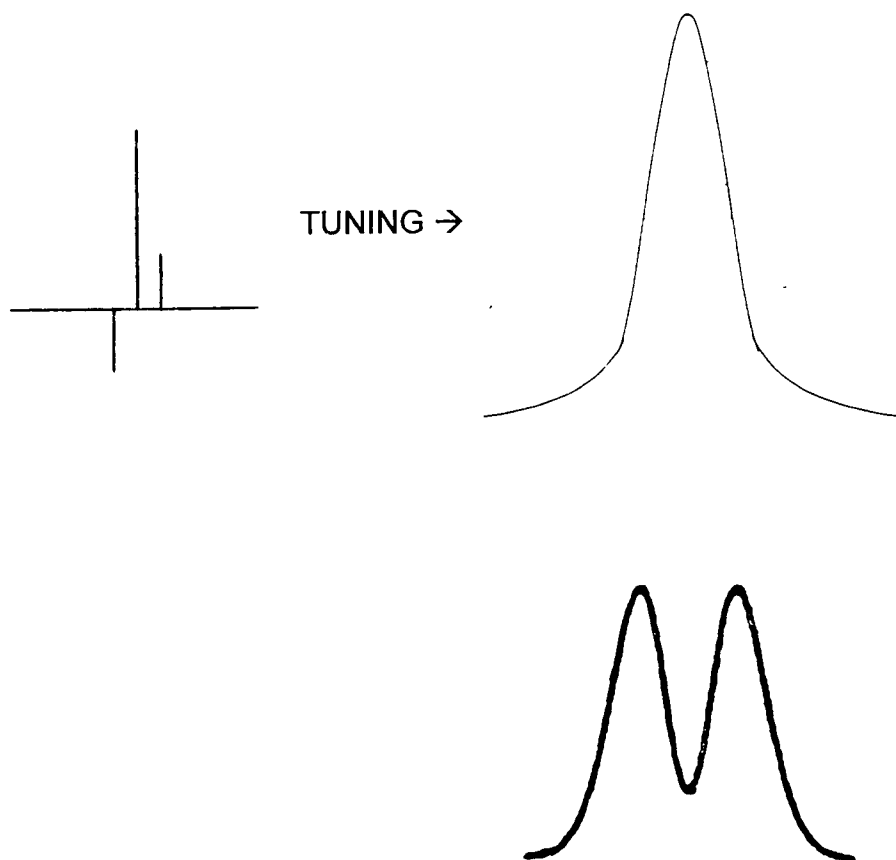


Figure 3.3 Carrier and sidebands tuned across an absorption line (top) give the heterodyne m-shape (bottom).

attenuated more than the lower sideband, and the sideband beats can no longer cancel. A resulting net beat signal becomes a heterodyne signal when the two beating frequency bands mix on the surface of a square-law photodetector. The photodetector converts the light intensity into a photocurrent. An oscilloscope or spectrum analyzer can measure this photocurrent which includes the beat frequency. As the laser continues its scan into the absorbing feature, the heterodyne signal continues to grow as the imbalance of the sideband magnitudes increases. As the scan takes the laser frequency near the center of the absorption, the two sidebands begin to experience similar attenuation, and the heterodyne signal falls to zero at line center. The scan continues into the far side of the absorption feature, and the sideband imbalance resumes, again giving a heterodyne signal until the laser is scanned past the absorption region. The heterodyne lineshape from the above sequence is clearly an m-shape. A similar situation occurs if the carrier and sidebands are tuned across an interferometer transmission resonance instead of an absorption resonance.

In the example above, only the first-order pair of sidebands, at $\omega_L \pm \Omega$ is considered. However, as we will see in the following section, a Fourier analysis of equation 3.9 yields sidebands at $\omega_L \pm 2\Omega$, $\omega_L \pm 3\Omega$, $\omega_L \pm 4\Omega$, and so on. The RFSA, operating as a tuned receiver, will respond to the modulation frequency, and all harmonics that are multiplicative factors of this frequency. As an example, if the spectrum analyzer is tuned to receive a modulation frequency of 10 MHz then it will measure *all* components of 10 MHz, including the second harmonic of the 5 MHz Fourier component, the third harmonic of the 3.33 MHz component,

and so on. However, the even-numbered harmonics do not contribute to the overall heterodyne signal of interest, due to a detail of the nature of frequency modulation; every even-numbered sideband pair is comprised of sidebands that are in phase with each other. Thus these pairs contribute to the heterodyne signal without the need for a spectrally absorbing feature. Being independent of the spectral feature of interest, these sideband pairs produce a background signal. Typically, the magnitudes of the sideband harmonics quickly diminish as their frequency moves away from the carrier frequency, so their contribution to the heterodyne signal is negligible.

3.2 Mathematical Description of Phase Modulation

If the amplitude or frequency of a sinusoidal function has time dependence, the resulting signal is best described in terms of a Fourier series of frequency components [Cuccia, 1952, Rowe, 1965, and Black, 1953]. Repeating equation 3.1, for a laser field,

$$E(t) = E_0(t) \exp[i(\omega_L t + \phi(t))] \quad 3.11$$

Here, we set $E_0(t) = E_0 = \text{constant}$. For notational clarity, let ω_L in equation 3.1 be written ω_0 .

In order to develop a mathematical description of phase modulation, we begin with the case of no amplitude modulation and a sinusoidally modulated phase:

$$\phi(t) = \beta \sin \omega_m t \quad 3.12$$

where β is the modulation index and ω_m is the modulation frequency. (In section 3.1, ω_m was called Ω). For the present case, equation 3.11 is written

$$E(t) = E_0 \exp[i(\omega_0 t + \beta \sin \omega_m t)] \quad 3.13$$

or,

$$E(t) = E_0 \exp[i\beta \sin \omega_m t] \exp i\omega_0 t \quad 3.14$$

keeping in mind that E_0 is a constant. The first exponential factor can be written as a complex Fourier series,

$$\exp[i\beta \sin \omega_m t] = \sum_{n=-\infty}^{\infty} C_n \exp[in\omega_m t] \quad 3.15$$

where the Fourier coefficients are,

$$C_n = \frac{\omega_m}{2\pi} \int_{-\frac{\pi}{\omega_m}}^{\frac{\pi}{\omega_m}} \exp[i\beta \sin \omega_m t] \exp[-in\omega_m t] dt \quad 3.16$$

The solution of the integral in equation 3.16 yields Bessel functions for the Fourier coefficients;

$$C_n = J_n(\beta) \quad 3.17$$

So finally we have

$$E(t) = E_0 \sum J_n(\beta) \exp[i(\omega_0 + n\omega_m)t] \quad 3.18$$

Equation 3.18 is the general expression for single-tone frequency modulation. By inspection, it can be observed that equation 3.18 is composed of a carrier and an infinite number of sideband pairs, as shown in Figure 3.4. All neighboring sidebands are separated by ω_m . Notice the odd-numbered lower side bands are phase inverted. This results from the equation [Cuccia, 1952, appendix has a nice treatment of Bessel functions in the context of modulation theory]

$$J_{-n}(\beta) = (-1)^n J_n(\beta) \quad 3.19$$

Also, the magnitude of the sidebands decrease as they move farther away from the carrier. The character of this sideband spectrum depends on the modulation frequency and index. Supplee, et al. [1994] review the effects of these parameters on frequency modulation spectroscopy.

Although frequency noise dominates amplitude noise in diode lasers, the noise modulation effects due to their coexistence can be realized by investigating the results of replacing E_0 in equation 3.13 with

$$E_0(t) = (1 + M \cos \omega t) E_0 \quad 3.20$$

In order to simplify the analysis, the cosine term adds an amplitude modulation of the same frequency as the frequency modulation.

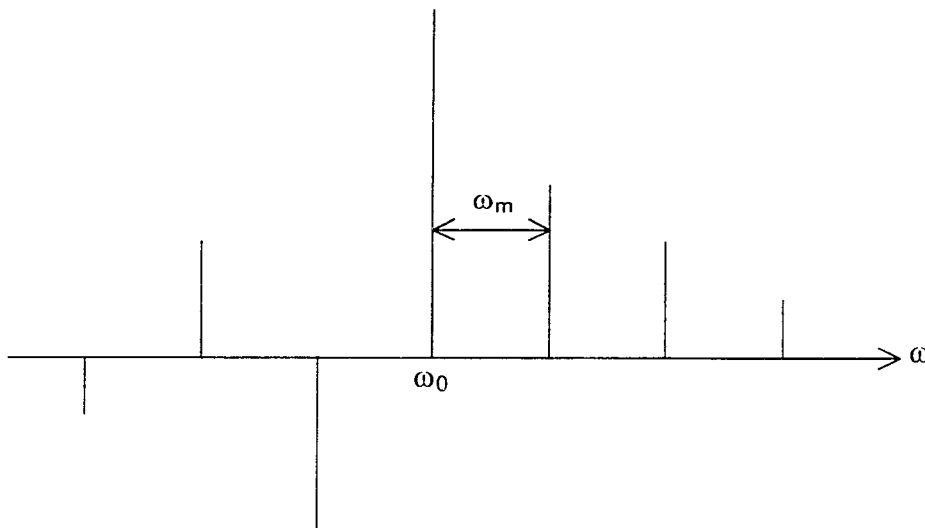


Figure 3.4 Carrier and sidebands for single-tone frequency modulation

Realizing that

$$\exp[i\beta \sin \omega_m t] = \sum_{n=-\infty}^{\infty} J_n(\beta) \exp[in\omega_m t] \quad 3.21$$

Equation 3.18 can be written in a final form;

$$\begin{aligned} E(t) = E_0 \{ & \sum_{n=-\infty}^{\infty} J_n(\beta) \exp i(\omega_0 + n\omega_m)t + \\ & \frac{M}{2} \sum_{n=-\infty}^{\infty} J_n(\beta) \exp i(\omega_0 + (n+1)\omega_m)t + \\ & \frac{M}{2} \sum_{n=-\infty}^{\infty} J_n(\beta) \exp i(\omega_0 + (n-1)\omega_m)t \} \end{aligned} \quad 3.22$$

This spectrum is shown in Figure 3.5. There is now a lack of symmetry between the upper and lower sidebands. The upper sidebands will always be greater on average than the lower sidebands. Some of the spectra of optical heterodyning display this asymmetry, as will be seen in Chapter 5 of this thesis.

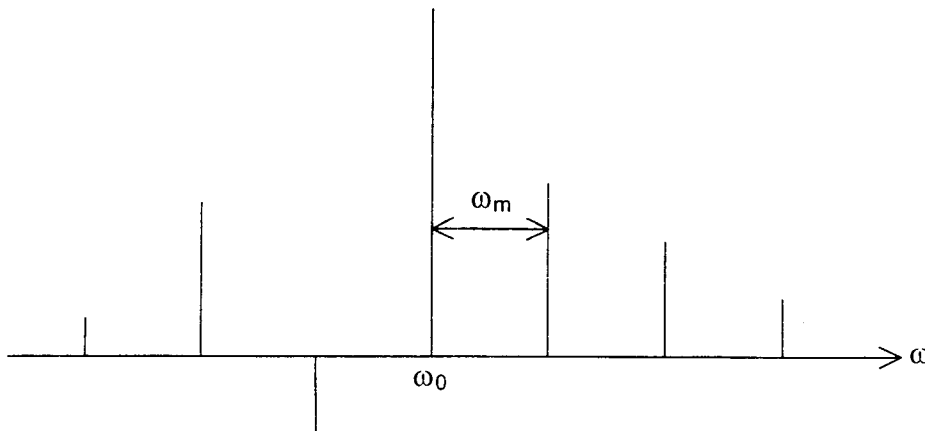


Figure 3.5 Carrier and sidebands for simultaneous frequency and amplitude modulation.

3.3 Using a Lummer-Gehrcke Interferometer to Measure Laser Phase Noise

3.3.1 Motivation

For a laser emission obeying the phase-diffusing field model presented in section 2.5.1, theory predicts a heterodyne lineshape to be the double-peaked m-shape, presented in section 3.1. Also, the peaks of the m-shape are predicted to be of equal height, a condition for which we will use the term “symmetric”. Earlier heterodyne work with rubidium [McIntyre, et al., 1993, and McIntyre, private communication] resulted in asymmetric m-shapes. It was noted [McIntyre, et al., 1993] that this asymmetry was largely attributed to the multilevel nature of the transitions they were working with, though another cause for asymmetry is the presence of amplitude noise in the laser emission. This rubidium example begins to illustrate the difficulties that arise when heterodyning with an atomic or molecular medium. Complications include optical pumping of ground-state hyperfine levels, homogeneous and inhomogeneous broadening mechanisms of the atomic/molecular gas or vapor, and selective reflection. Therefore, our work begins with the simplest case of heterodyning, using an interferometer.

We have seen (section 3.1) that a heterodyne lineshape of an interferometer is a symmetric m-shape, if the laser noise is described by the phase-diffusing model (PDM), i.e. amplitude noise is not present. In anticipation of the more complicated heterodyne work with molecular oxygen, we investigate the character of our diode laser emission, which we will later use for the oxygen

work, by using this laser for interferometer heterodyning. To see if this diode laser's emission obeys the PDM, we look for symmetric m-shapes.

A final concern with the character of the diode laser emission is that we want to ensure that this emission is not affected by any parts of the experiment external to the diode laser, such as optical feedback. For this reason we avoid using a Fabry-Perot interferometer, which has been known to result in asymmetric m-shapes [McIntyre, personal communication], perhaps because a properly aligned Fabry-Perot interferometer will reflect light back into the laser cavity. Below, we describe the interferometer that we use.

3.3.2 Lummer-Gehrcke Interferometer

A Lummer-Gehrcke interferometer (LGI) is a multiple-beam interferometer. It is a rectangular slab of quartz with a prism optically fused to one of the larger surfaces of the plate, as illustrated in Figure 3.6. A beam of light enters the

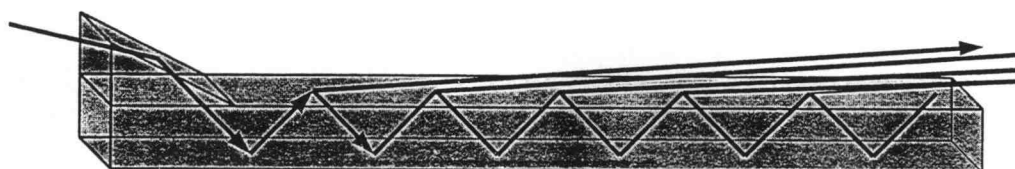


Figure 3.6 Lummer-Gehrcke interferometer

vertical face of the prism, at an angle far from orthogonal to this surface, thus avoiding any possibility of optical feedback into the diode laser. The beam is then internally reflected from the diagonal face of the prism. Subsequently, the beam enters the slab and repeatedly internally reflects from the top and bottom surfaces, as a result of (almost) total internal reflection. The function of the prism is to allow the beam to enter the slab at less than the critical angle so that total internal reflection can occur.

For proper interferometric operation to occur, the beam in the slab must be internally reflected at slightly less than the critical angle, resulting in a small fraction of the beam exiting the slab (transmission at the interface) at every reflection. Concomitant with the multitude of internal reflections is a number of exiting beams, each one phase-delayed consecutively from the next. The phase delay is a result of the additional distance the internal beam travels during the next two internal reflections.

The exiting beams emerge from both the top and bottom surface of the LGI at a near-grazing angle, though only one surface is utilized. Exiting the surface of the plate, all the beams are parallel to one another, requiring a converging lens, or beam divergence, so the exiting beams overlap and interfere with each other on a screen or detector.

The intensity distribution of the interference pattern of the LGI, at the detector, is given by [Born and Wolf, 1965]

$$I(\delta) = \frac{1 + G_p \sin^2 \frac{p\delta}{2}}{1 + F \sin^2 \frac{\delta}{2}} (1 - \Re^p)^2 \quad 3.23$$

where

$$F \equiv \frac{4\Re}{(1 - \Re)^2} \quad 3.24$$

and

$$G_p \equiv \frac{4\Re^p}{(1 - \Re^p)^2} \quad 3.25$$

δ is the phase difference between successive beams, \Re is the reflectivity inside the plate interface, p is the number of exiting beams, and I is the intensity at the detector with the LGI removed. The finesse, f , is defined as the ratio of the separation of adjacent fringes to their FWHM, and $f = (\pi/2)F^{1/2}$. Figure 3.7 shows the plotted spectrum of equation 3.23 for several different values of p . It is similar to an Airy function modified by the sinusoid in the numerator. The result is the occurrence of subsidiary maxima between the usual Airy maxima. These subsidiary peaks diminish as the number of exiting beam contributions increases. As p approaches infinity, equation 3.23 approaches the usual Airy transmission function associated with the common Fabry-Perot Etalon.

In Appendix A, some useful relations are derived for the LGI.

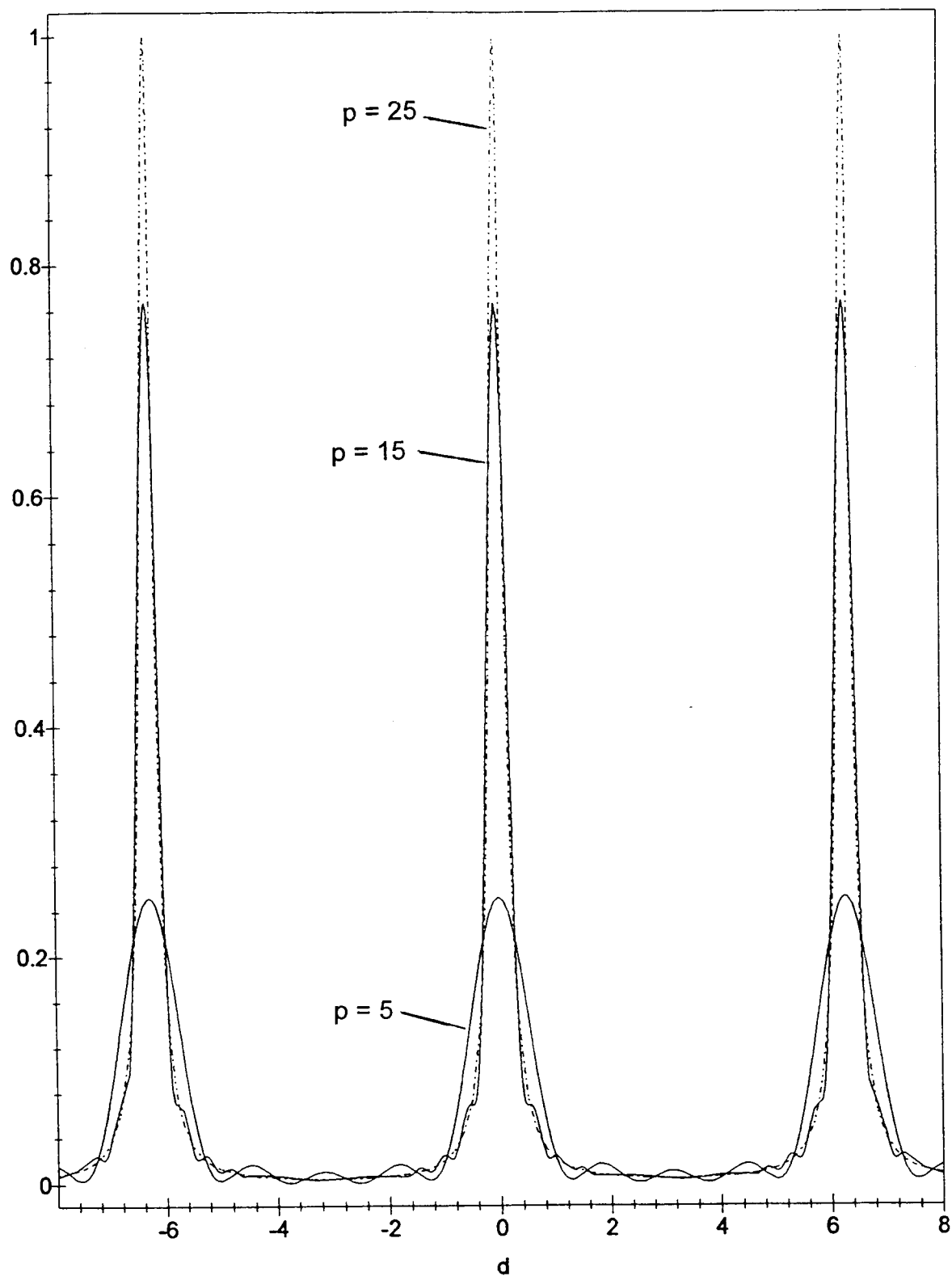


Figure 3.7 LGI output spectra for several values of exiting beam number, calculated using equation 3.23.

3.4 Lummer-Gehrcke Heterodyning

A simplifying approach to analyzing the LGI heterodyne spectrum is the two-beam approximation. In this case, only two of the many exiting beams of the LGI are considered, and we can use the results of section 3.1. Thus, a LGI heterodyne spectrum is the symmetric m-shape, centered at the LGI transmission resonance. The center of this m-shape, the central minimum, goes to zero in this approximation. In other words, at exact resonance the heterodyne signal is zero.

We now treat the case of a general number of interfering beams of a LGI. In principle, we can predict a heterodyne spectrum for the LGI using equation 3.23, by replacing δ with $\delta + \Delta\phi$, where $\Delta\phi = \Delta\phi(t)$ carries a time dependence that can be measured by a spectrum analyzer. However, this approach is mathematically non-trivial, since $\Delta\phi$ represents a Fourier series of very many terms. In Appendix B a treatment of a general number of LGI beams is given. The resulting heterodyne intensity equation is very similar to equation 3.6, indicating that the many-beam case also gives the result of a double-peaked heterodyne m-shape centered at resonance. Quantitative predictions of the relative magnitudes of the peak heterodyne intensity and the central minimum intensity would require the incorporation of a proper diode laser noise model, such as the PDM, along with the transmission function of the LGI. This analysis is beyond the scope of this thesis, but it is a topic for future research. For our work now, the usefulness of the qualitative theoretical predictions of symmetric m-shapes is enough to allow

us to characterize the emission of our diode laser and to ensure that it obeys the phase-diffusion model.

3.5 Heterodyning with an Atomic/Molecular Vapor or Gas

3.5.1 Introduction

By using a diode laser for heterodyne spectroscopy of an atomic or molecular medium, one takes advantage of the frequency noise that is always present in these lasers. External frequency modulation of the laser injection current is not needed.

A heterodyne signal is produced as the diode laser field jumps in and out of resonance with an atomic line. The condition for macroscopic dipole polarization is much more favorable as the laser field's frequency approaches resonance. When this incident field jumps into resonance, a polarization is set up in the medium that oscillates at $\omega_{\text{medium}} = (\Delta E/\hbar)$, where ΔE is the energy of the atomic line transition and \hbar is Planck's constant. When the diode laser field jumps out of resonance, the polarization that was set up in the medium originally, oscillating at ω_{medium} , continues to "ring", albeit with an exponentially decaying amplitude due to dephasing mechanisms such as collisions. The polarization field and the present incident laser field beat with one another as they mix at the surface of a photodetector.

As a manifestation of phase noise, the optical field of a diode laser jumps around in frequency space. A typical diode laser linewidth of 100 MHz implies a coherence length of several meters. This is long enough to enable a perfectly coherent wave train to encompass the entire length of a gas cell filled with an atomic or molecular medium. The medium will experience a new single-frequency coherent field as the diode laser jumps to a new frequency. A requirement for heterodyning of the atomic medium is that the lifetime of the macroscopic polarization be at least as long as the coherence time of the laser, so that the polarization field and incident laser field can coexist.

As discussed in the first part of this chapter, section 3.1, an atomic or molecular absorption line will give us a heterodyne m-shape. The character of this m-shape, such as the width, central minimum value, and peak value, is predicted by the phase-diffusing model (PDM) theory of Cooper, et al. [1990]. With this theory, the profile as a function of laser detuning is dependent on the spectrum analyzer frequency, the natural linewidth of the medium, and the laser linewidth.

One may realize a familiarity in the description above of the process of heterodyning with an atomic medium to that of coherent transient experiments, such as optical nutation and free induction decay [Sargent, et al., 1974, Brewer, et al., 1972, Yong-qing, et al., 1996, Dube, et al., 1996, and Brewer, et al., 1976]. The crucial comparison is the beating of the incident field with the field of the induced polarization of the sample. A difference is that heterodyning with a diode laser gives the needed frequency shifts into and out of resonance automatically.

There is no need to Stark shift the sample into or away from resonance, or to modulate the laser frequency externally.

The molecular oxygen absorption lines we are working with are in the electric dipole forbidden $b^1\Sigma_g^+(v'=0) \leftarrow X^3\Sigma_g^-(v''=0)$ band known as the A-band of oxygen [Babcock, et al., 1948, Kroll, et al., 1987, Ritter, et al., 1987]. This band is shown in Figure 3.8. The transitions then are primarily magnetic dipole [Garstang, 1962], yielding a very small linestrength of about 9×10^{-10} . This is readily calculated from the Ladenburg relation [Corney, 1977];

$$f = \frac{4\epsilon_0 m_e c \lambda_0^2}{8\pi e^2 \tau_n} \quad 3.26$$

where m_e is the electron mass, e is the electron charge, c is the speed of light, λ_0 is the resonance wavelength, ϵ_0 is the permittivity, and τ_n is the natural lifetime of

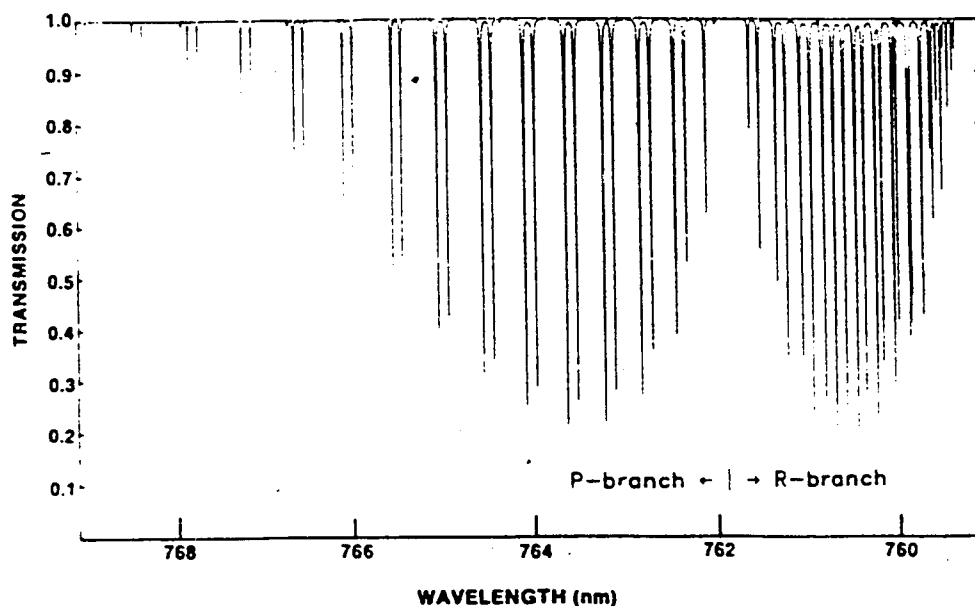


Figure 3.8 Calculated transmission spectrum of oxygen (Kroll, et al., 1987).

the transition, (approximately 10 seconds). These A-band transitions are two level transitions, which the PDM-based heterodyne theory assumes. This theory also assumes that the only dephasing mechanism of the absorption medium is the natural lifetime decay, neglecting consideration of interatomic collisions. In the case of the forbidden oxygen A-band transitions, the natural lifetime is so great that the dominant dephasing mechanism is interatomic collisions. In the next section we discuss the PDM heterodyne theory, and show that sum of collision broadening and natural broadening can replace just natural broadening, in the theory.

3.5.2 Heterodyne Theory for a Diode Laser Emission Obeying the Phase-Diffusing Model

The PDM-based heterodyne theory is based on the development of a phase-diffusing laser field as it propagates through a resonant two-level medium [Cooper, et al., 1990]. The theory considers the inhomogeneous Doppler broadening of the medium. As the modified laser field is incident on a square-law photodetector, a heterodyne signal is predicted by the theory, and measured by a tuned-frequency RFSA. This heterodyne signal is integrated over the Doppler distribution of the medium. A final step in the development of the theory is a Fourier transform from the time domain to the frequency domain.

In the theory, the parameters needed to predict the heterodyne spectra are the spectrum analyzer frequency, ω , the laser detuning from the atomic resonance, Δ , the natural linewidth of the atomic medium, γ , and the laser

linewidth, Γ . In our work with oxygen, with very long lifetime transitions, the collision linewidth is dominant over the natural linewidth, and Doppler broadening. Therefore we add the collision linewidth to the natural linewidth, as Schuurmans shows when he introduces interatomic collisions to his calculation of the polarization of a gas [Schuurmans, 1980], and use this resulting parameter in the theory.

In this thesis we apply an incomplete PDM-based heterodyne theory to our oxygen work; we ignore Doppler broadening. This is justified because, as mentioned in the previous paragraph, we include collision broadening instead. The following equation is the theoretical heterodyne intensity with no Doppler broadening [J. Cooper, private communication]:

$$\begin{aligned}
 I(\Delta) \propto & \frac{\Gamma}{\gamma[\Delta^2 + (\Gamma + \gamma)^2]} \left\{ \frac{(\gamma + \Gamma)}{[(\omega + \Delta)^2 + (\gamma + \Gamma)^2]} + \frac{(\gamma + \Gamma)}{[(\omega - \Delta)^2 + (\gamma + \Gamma)^2]} \right\} + \\
 & - \frac{\Gamma[(\gamma + \Gamma)^2(2\Gamma + \gamma) - \Delta^2(4\Gamma + 3\gamma)]}{[\Delta^2 + (\gamma + \Gamma)^2]^2[\Delta^2 + (\gamma + 2\Gamma)^2]} \left\{ \frac{(\gamma + \Gamma)}{[(\omega + \Delta)^2 + (\gamma + \Gamma)^2]} + \frac{(\gamma + \Gamma)}{[(\omega - \Delta)^2 + (\gamma + \Gamma)^2]} \right\} + \\
 & - \frac{\Delta\Gamma[(\gamma + \Gamma)(5\Gamma + 3\gamma) - \Delta^2]}{[\Delta^2 + (\gamma + \Gamma)^2]^2[\Delta^2 + (\gamma + 2\Gamma)^2]} \left\{ \frac{(\omega - \Delta)}{[(\omega - \Delta)^2 + (\gamma + \Gamma)^2]} - \frac{(\omega + \Delta)}{[(\omega + \Delta)^2 + (\gamma + \Gamma)^2]} \right\} \quad 3.27
 \end{aligned}$$

In Chapter 5 we set γ equal to the collision linewidth, and compare our experimental results with the theoretical results of this equation.

We now show that equation 3.27, which was derived without integrating over a Doppler distribution, may only modify the theoretical results slightly, even for

the case of Doppler broadening dominant over collision broadening. For this case we use a rubidium transition with a natural linewidth of 6 MHz. At room temperature the Doppler width is 570 MHz, and collisional broadening can be neglected because the vapor pressure is very low. Figure 3.9 compares several characteristics of a single peak of the heterodyne m-shape, using parameters for rubidium, predicted by the theory with and without the Doppler integration. In the case without Doppler integration, the Doppler linewidth is used for γ instead of the natural linewidth. In doing this, Doppler broadening is considered by the theory but the Doppler frequency distribution is ignored. Peak heights and central minimum heights for the cases with Doppler and without Doppler considerations, shown in Figure 3.9a, are normalized to unity at zero RFSA frequency. In Figure 3.9b, both cases of FWHM are set equal at zero RFSA frequency, as is also the situation for both cases of center width.

Differences between considering Doppler integration or not, shown in Figure 3.9, are noticeable, but not drastic. There is much more work involved in producing the plots from the theory that includes the Doppler distribution compared to simply using equation 3.27. So one may seriously consider whether the slightly-increased accuracy is worth the extra effort .

The usefulness of equation 3.27 for the case with rubidium, in the previous paragraph, gives us confidence of the validity of using this equation for theoretical comparisons with our oxygen data, since Doppler consideration are less important for oxygen than rubidium.

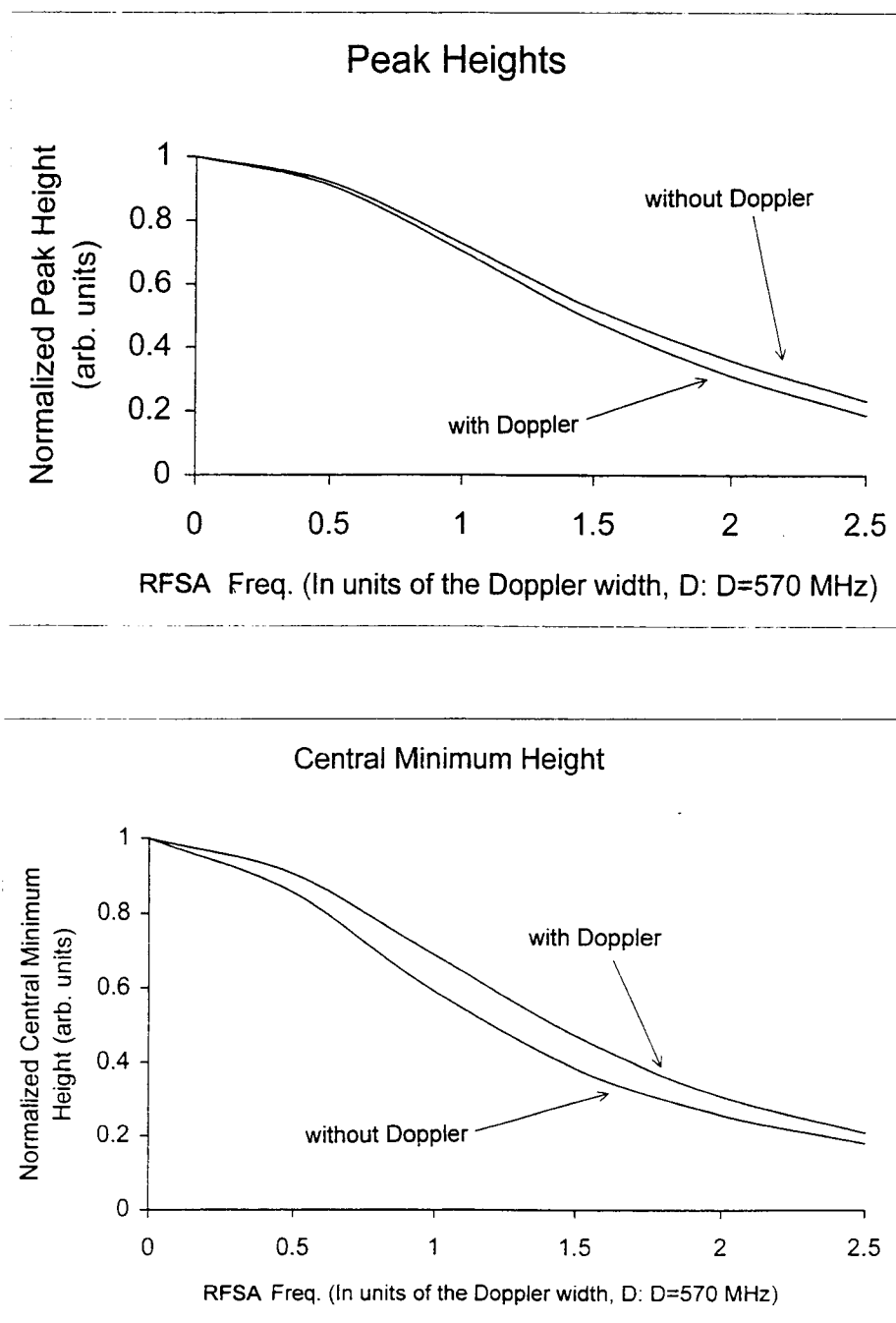


Figure 3.9a Calculated heterodyne peak height (top) and central minimum height (bottom) of rubidium with and without Doppler integration, versus spectrum analyzer frequency.

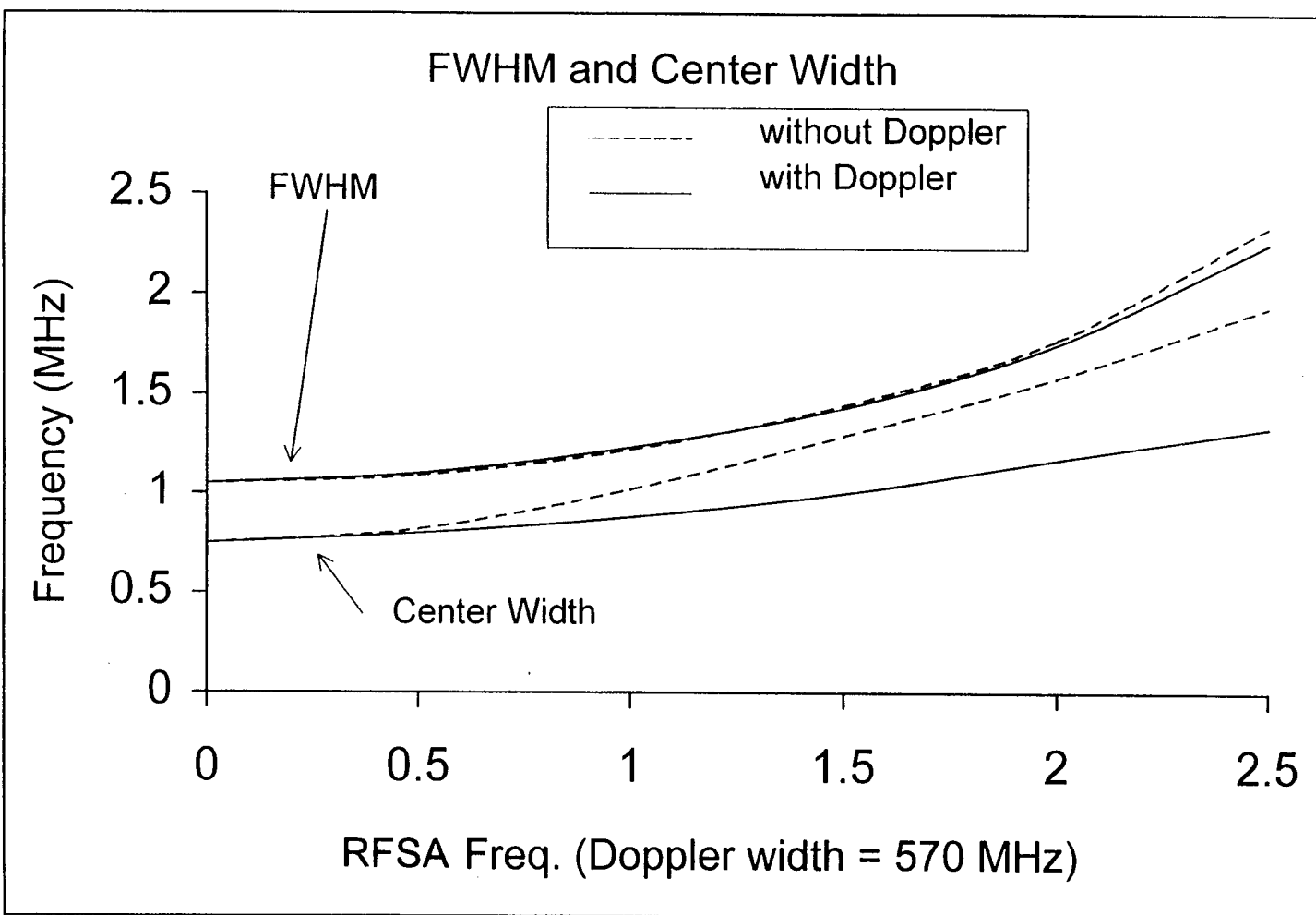


Figure 3.9b Calculated heterodyne FWHM and center width of rubidium with and without Doppler integration, versus spectrum analyzer frequency.

3.6 Selective Reflection as a Possible Source of Optical Feedback.

In our work with oxygen gas, we shine the diode laser beam into a gas cell which has quartz end-windows, as fully explained in Chapter 4. This arrangement can produce unwanted optical feedback into the diode laser from reflections from the gas itself, by a phenomenon called selective reflection (SR) [Schuurmans, 1980]. When light is incident on the interface between a dielectric and an atomic medium, the Fresnel reflectivity of the interface changes as the light frequency is tuned across an atomic resonance. This resonance modification of the reflectivity occurs mostly within a few GHz of line center, as shown in Figure 3.10.

The spectral dependence of SR is double-peaked at resonance, resembling a heterodyne m-shape. Therefore, feedback into the diode laser, from SR, can increase amplitude and phase noise, enhancing the heterodyne m-shape peaks

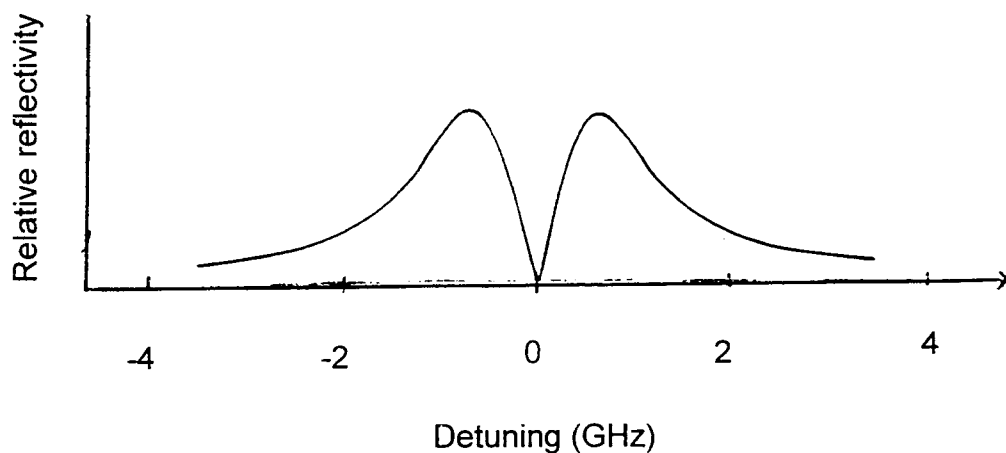


Figure 3.10 Schematic of selective reflection versus detuning.

beyond what they would be if the only phase noise in the laser emission were from the unperturbed laser. Thus, SR, if present, will be a complication in comparisons between our measurements and the PDM-based heterodyne theory. However, as discussed in Chapter 4, null results of experimental tests for the presence of selective reflection effects allow us to ignore SR in our present work.

As described in Chapter 4, even though the end-windows of our oxygen cell are tilted to prevent Fresnel reflection from traveling back in the direction of the laser, SR creates a backward wave that travels back towards the incident beam, regardless of the angle of incidence on the reflecting surface. This situation is depicted in Figure 3.11.

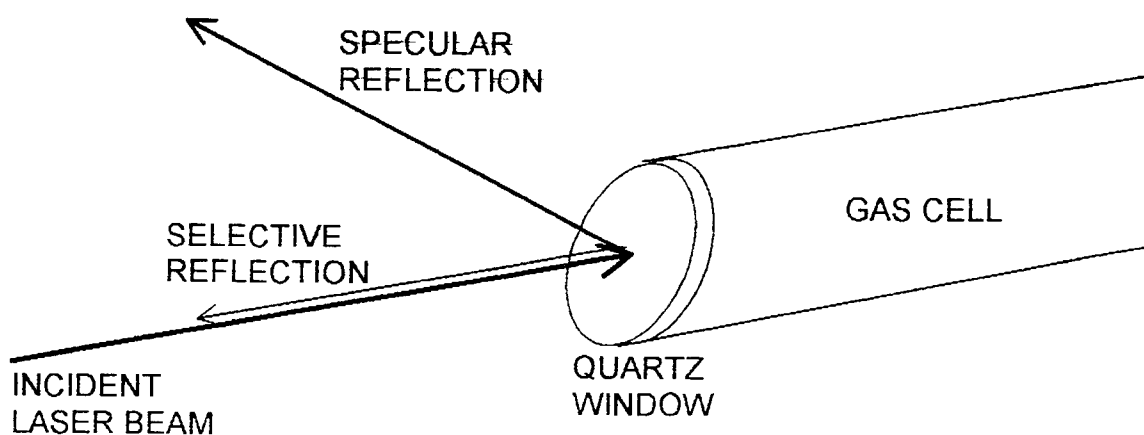


Figure 3.11 Graphical depiction of directional differences between specular and selective reflection.

In the work of this thesis, there is no way to ensure that selective reflection is not fed back into the diode laser. An optical isolator could be placed between the laser and the oxygen cell's front window, but reflections from the optical isolator will occur without the use of anti-reflection coatings designed for the wavelength for which the optical isolator is used. For the present work, an optical isolator designed for the proper wavelengths was not available for our use.

For the interested reader, the following is a brief survey of recent work on SR.

The concept of SR has been known since the early part of the twentieth century [Wood, 1909]. A significant milestone of SR was made much later by Cojan [1954] when he observed sub-doppler features in the selective reflectance and related these to interactions of the atomic medium with the window (wall collisions). Arguably, the beginning of the modern age of SR studies began with the work of Woerdman, et al. [1975], and Schuurmans [1980]. Schuurmans and Woerdman carried out detailed studies of the sub-doppler characteristics of SR and demonstrated that they originate in the interruption of the optical dipole phase by atom-wall collisions, and to the subsequent transient response of ground-state atoms departing from the surface. Current research in SR involves its use as an investigative tool to study atom-surface interactions [Ducloy, et al., (1991)], the study of SR in the dense atomic vapor regime [Guo, et al., 1996], SR as a powerful spectroscopy tool [Wang, et al., 1997], SR as a function of incidence angles [Nienhuis, et al., 1988], SR as a function of incident intensity [Friedberg, et al., 1990], and SR in a pump-probe scheme [Schuller, et al., 1991].

To this end, Wang, Gallagher, and Cooper profoundly state the following [Wang, et al., 1997]: "Selective reflection was first observed at the beginning of the century, but it remains a complicated phenomenon for atomic physics theory. A seemingly simple SR experiment may involve many physical processes that are interleaved in the observations, making it a challenge to obtain an accurate theoretical model."

3.7 (Optional) Heterodyne Detection and the Correlation Function

In this section, heterodyne detection is explained in terms of the correlation function, which may be more familiar to the reader than heterodyning. In the present case, the correlation function is used to measure the degree of coherence of a laser field.

Essentially, optical heterodyning is the process of mixing light at a detector. The light being mixed may have originated from the same light source, perhaps passing through an interferometer, or the light may originate from different sources altogether, as in the case of the application of a local oscillator. The process of detection squares and time-averages the sum of the fields of light that are mixed. The individual fields, in general, have different amplitudes, frequencies, and phase.

An application of the utility of heterodyne detection is the measurement of the degree of coherence of a light source, such as the laser [Pedrotti, et al., 1993]. A simple way of illustrating this point is to analyze the situation of a partially

coherent laser beam travelling through an interferometer. For simplicity, this interferometer's output consists of only two beams. These two output beams can be described by the complex fields \mathbf{E}_1 , and \mathbf{E}_2 , respectively, and let \mathbf{E}_2 be time-delayed by the interferometer, with respect to \mathbf{E}_1 . These fields then mix at a photodetector. The photodetector squares and time-averages the sum of the fields, to give the intensity,

$$I = \langle (\mathbf{E}_1 + \mathbf{E}_2) (\mathbf{E}_1^* + \mathbf{E}_2^*) \rangle, \quad 3.28$$

assuming the fields have identical polarization. Expanding,

$$I = \langle |\mathbf{E}_1|^2 + |\mathbf{E}_2|^2 + (\mathbf{E}_1 \mathbf{E}_2^* + \mathbf{E}_1^* \mathbf{E}_2) \rangle, \quad 3.29$$

or,

$$I = I_1 + I_2 + 2 \operatorname{Re} \langle \mathbf{E}_1 \mathbf{E}_2^* \rangle, \quad 3.30$$

where I_1 and I_2 are the intensities of the individual fields. The third term of equation 3.30 represents the interference of the two fields. The interferometer introduces a time delay, τ , between the two fields. The interference term of equation 3.30 forms the basis of what is called the correlation function, γ ,

$$\gamma \equiv \langle \mathbf{E}_1(t) \mathbf{E}_2^*(t - \tau) \rangle. \quad 3.31$$

If both fields, \mathbf{E}_1 and \mathbf{E}_2 , are identical except for their phase at the detector, then γ is called the autocorrelation function.

It is easily demonstrated that heterodyne detection measures the correlation function, if the fields are written (compare to equation 3.2),

$$E_1 = E_0 \exp\{i[\omega t - \varphi(t)]\} \quad 3.32$$

$$E_2 = E_0 \exp\{i[\omega(t - \tau) - \varphi(t - \tau)]\}. \quad 3.33$$

This implies that the interferometer delays one beam relative to the other, without dissimilar attenuation. This loss of generality does not change the character of the results below, but merely simplifies notation.

For optical frequencies, we use equations 3.32 and 3.33 in equation 3.30 to get

$$I(t) = I_1 + I_2 + 2E_0^2 \operatorname{Re} \{ \exp\{i[-\omega\tau + \varphi(t) - \varphi(t - \tau)]\} \} \quad 3.34$$

or,

$$I(t) = I_{DC} + I_0 \cos [-\omega\tau + \Delta\varphi(t, \tau)] \quad 3.35$$

where the change in phase in time τ is $\varphi(t, \tau) \equiv \varphi(t) - \varphi(t - \tau)$, I_{DC} is the constant, time-independent part of the intensity, and I_0 is the amplitude of the varying part of the intensity due to the interference. $\Delta\varphi$ is a function of both t and τ , since the change in phase is clearly dependent on the path difference delay, and the phase of the source is a function of time. Note that equation 3.35 is the same as equation 3.6.

CHAPTER 4: EXPERIMENTAL TECHNIQUES

The work of this thesis involves several experimental configurations, depending on the type of measurements performed. The experimental technique for heterodyne spectroscopy with a LGI, and the similar technique used for work with oxygen, will be discussed in this chapter. Direct AM noise measurements use a technique that is different from FM noise detection, and this is also discussed in the present chapter. Major parts of the experimental apparatus include a diode laser, diode laser drive current control system, diode laser temperature control system, the photodiode detection system, the oxygen cell, the LGI, data acquisition and control of the experiment by a computer, the radio frequency spectrum analyzer, and various beam-steering optics and focusing lenses. The present chapter describes the apparatus and its components.

4.1 Diode Lasers

For the oxygen work, a near-infrared (NIR) diode laser is used. This free-running diode laser is a 10 mW, index-guided, GaAlAs device (Sharp model LT031MDO), emitting at 758 nm at room temperature (this model is sold as a nominal 750 nm device). It has a measured free-spectral range of 150 GHz. The laser cavity is AR coated on the forward face, and reflection-coated on the rear

face [Sharp Corp., 1988]. The diode laser package, a TO-5 can, has a glass window through which the laser emits. The current threshold of the laser is 32 mA, and the operating current for the data presented in this thesis is within the range from 45 to 56 mA.

The linewidth of the diode laser was never measured, but it is assumed to be in the range 10-100 MHz for the conditions of operation used in the experiments.

The LGI work, reported in this thesis, utilized the diode laser described above, and also a visible diode laser. This visible diode laser is a Toshiba TOLD9215, 675 nm, 10mW laser, with a current threshold of 35 mA. Its free-spectral range was measured to be 100 GHz.

A particular 758 nm diode laser was used for all of the oxygen work presented in this thesis. This laser could be wavelength-tuned through six oxygen absorption lines without mode-hopping, which led to the following activities and assumptions: 1) We were able to spectrally map the oxygen lines which we measured. By comparing our measured spectral map with the well-known spectrum of the A-band of oxygen, we identified which transitions we were studying. 2) The original, measured heterodyne spectra are in terms of diode laser drive current. By knowing the diode laser drive current at every absorption line (diode laser temperature held constant), the spectral distance between absorption lines, and the change of diode laser emission frequency with respect to change of diode laser drive current, we can analyze the heterodyne spectra in terms of frequency detuning from the absorption lines. This is explained further in section 4.7. 3) A lack of diode laser mode-hopping near an absorption line being

investigated helps to ensure that mode-partition noise (chapter 2) can be neglected since this type of noise is only significant when the SMSR decreases, occurring near a mode-hop.

4.2 Diode Laser Mounting and Temperature Control

The diode laser mount has several crucial functions aside from the obvious role of physically holding the laser in place. The mount allows control of the operating temperature of the laser, and accommodates beam collimation of the laser.

The diode laser mount used in the experiments of this thesis is a Light Control Instruments, model 700 series, Temperature Controlled Mount. (This mount now exists only under the name of Newport Corporation). The mount incorporates internal temperature control circuitry, interfaced with an external temperature controller. The laser temperature detection uses a 10 k Ω thermister, mounted close to the diode laser, connected to a feedback/control circuit that controls the current flowing in two 16.8 watt thermo-electric modules (peltier coolers). These modules can heat or cool the laser, depending on the direction of current flow. The feedback/control circuit is a Light Control Instruments (now Newport Corporation) model 325 temperature controller. This controller has a temperature stability of .005 degrees centigrade over a 10 to 30 minute period, and a stability of .01 degrees over a 24 -hour period, as advertised in the manual.

Prior to being placed in the diode laser mount, the diode laser is inserted into a small diode laser holder that allows control of the collimation of the linearly polarized beam. This holder, an Optima Precision CDL 3600 Kit, incorporates a small lens assembly that has an adjustable proximity to the front face of the diode laser, thus controlling the focus of the beam. For the measurements reported in this thesis, the focus was set to approximately 3 meters. The cross-section of the beam was slightly elliptical. The lens system can compensate for astigmatism, but this wasn't done to any precision, since the heterodyne work, reported in this thesis, has no particular dependence on the intensity profile of the laser beam.

Finally, the diode laser mount acts as a heat-sink, which is crucial for diode laser operation, for several reasons. The heat-sink helps support thermal stability of the diode laser by increasing the heat capacity of the diode laser/heat-sink system. Also, a diode laser without sufficient heat sinking will operate at elevated temperatures, which can greatly shorten the lifetime of the laser.

4.3 Optical Layout Including LGI and the Oxygen Cell

The complete apparatus, with a LGI, is shown in Figure 4.1. For oxygen heterodyning, the LGI is replaced by the oxygen cell. To monitor the laser for stable single mode operation, a small fraction of the laser beam is focused into a

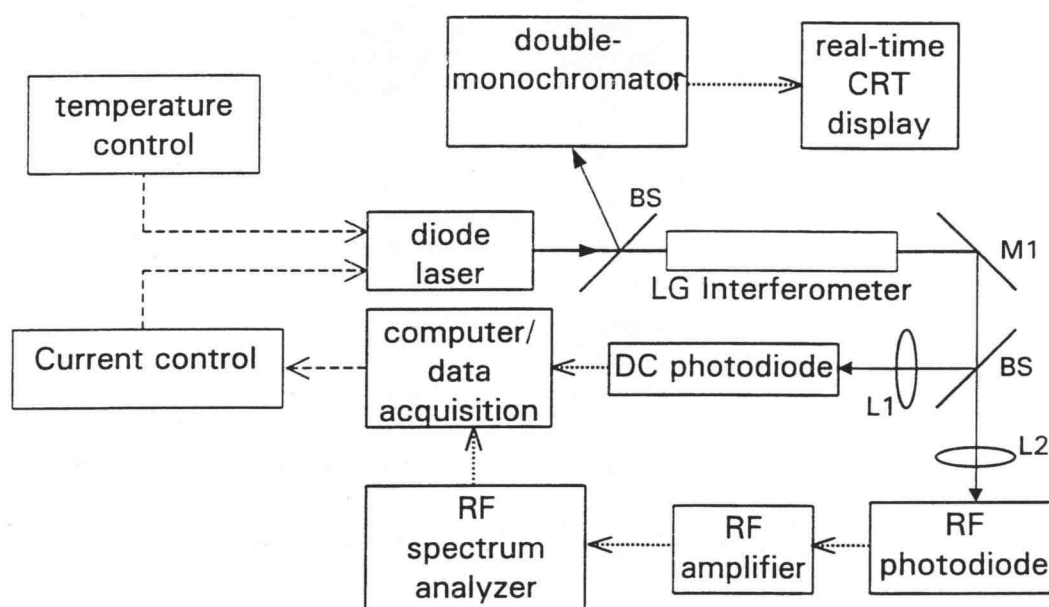


Figure 4.1 Schematic description of experimental apparatus, showing LGI.

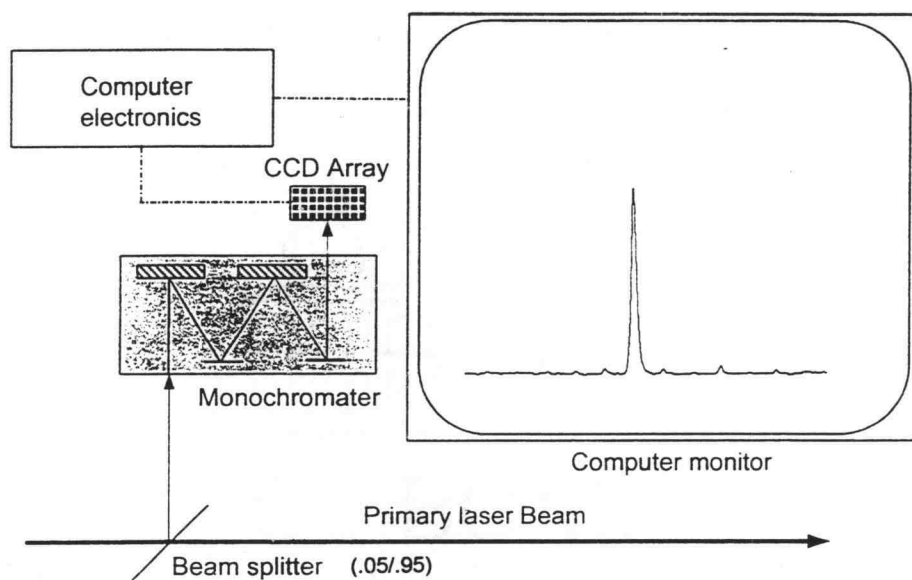


Figure 4.2a Scheme used to monitor, in real-time, the emission spectrum of the diode laser.

1/2-meter double monochromator, using a beam-splitter closely positioned to the diode laser. This is shown in Figure 4.2a. The spectral resolution of the monochromator is .01 nm (~ 10 GHz at 750nm), which is sufficient to detect individual laser-mode peaks. The monochromator used is Oriel Corporation, model 77200. After setting the diode laser to a desired emission wavelength, the monochromator is set to focus the laser light in the center of a CCD array detector. The computer-interfaced CCD array data is displayed, real-time, on a CRT. This array detects a total frequency width of 850 GHz, which is equivalent to approximately five free spectral ranges of the diode laser. The resolution observable on the CRT is approximately 30 GHz per centimeter of screen, along the horizontal axis. Examples of the output of this system are shown in Figure 4.2b, for pure single mode operation with the 750 nm diode laser, and the multi-mode emission of a 670 nm diode laser.

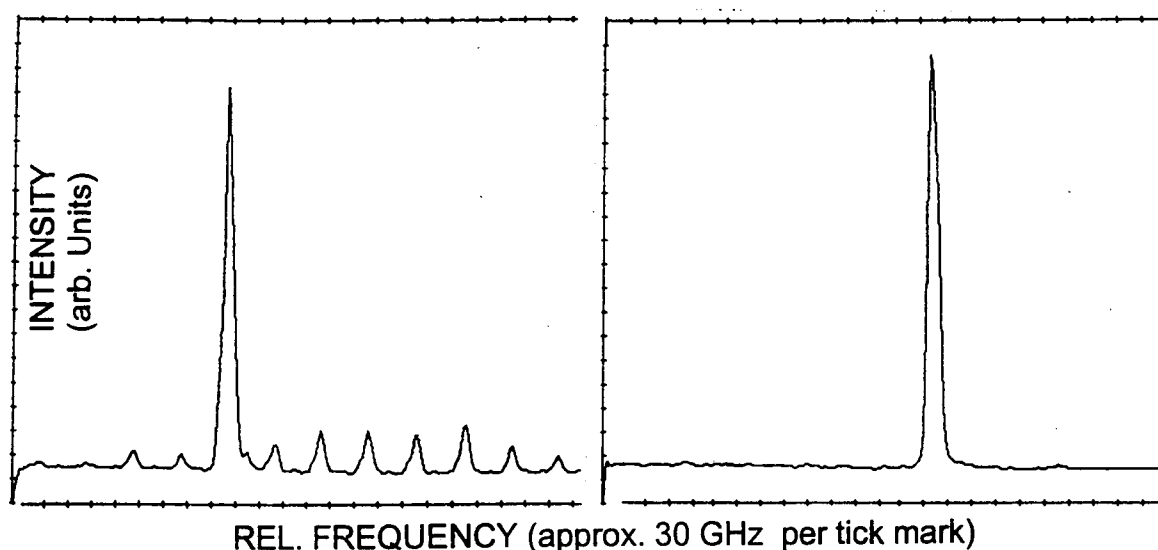


Figure 4.2b Two examples of monitor output of the apparatus shown in Figure 4.2a. An emission spectrum for a 670 nm and a 760 nm diode laser is shown in the left and right figure, respectively.

Depending on the type of experiment, the laser beam either encounters a LGI, or an oxygen cell. In both cases, after travelling through the LGI or the oxygen cell, the beam encounters a beam-steering mirror, that guides it into a wedged, uncoated, quartz window, acting as a beam-splitter. The wedge-shape prevents etaloning, by diverting second-surface reflections away from the primary optical axis. From the wedged window, the transmitted beam is focused onto an RF-measuring photodiode, and the reflected beam is focused onto a DC-measuring photodiode.

The following measures were made to eliminate the possibility of optical feedback into the diode laser, from components in the optical path. The wedged windows at each end of the five-centimeter-diameter, two-meter-long gas cell, are tilted about 5° , so that neither surface can specularly reflect laser light back into the diode laser. These windows are 7° wedges; that prevent etalon interference. For the same reason, these end-windows are mounted out-of-parallel with each other, by a small angle of several degrees. Details of the oxygen cell are shown in Figure 3.3. All optical elements are intentionally adjusted out of the plane perpendicular to the optical axes of the system. This includes the photodiode windows, and the photodiode elements (p-n junction surface) themselves.

The physical dimensions of the LGI are 13 cm long, and 0.45 cm thick. The transmission function of the LGI, with a free spectral range of 33 GHz and a finesse of 10, was measured by scanning a 760 nm diode laser across two fringes, by a scanning method that is explained in section 4.7, and section 5.1.

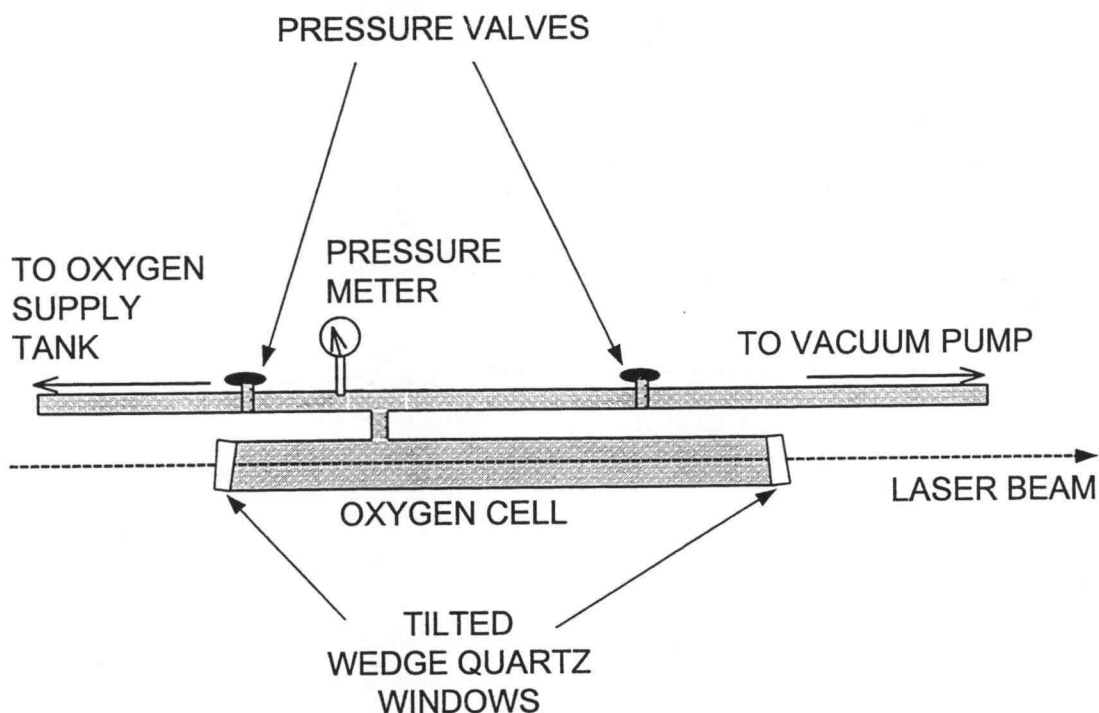


Figure 4.3 Oxygen gas cell details.

This measured transmission spectrum, as shown in Figure 4.4, agrees with the theory presented in section 3.3 (compare with Figure 3.7), except a ghost fringe, about 2 GHz away from the main fringe, is observed in this spectrum. A longitudinal curvature in the slender LGI, although not directly observed, may be responsible for this aberration. The intensity of the ghost fringe is approximately one-tenth that of a principal fringe. Although the ghost can be observed in the

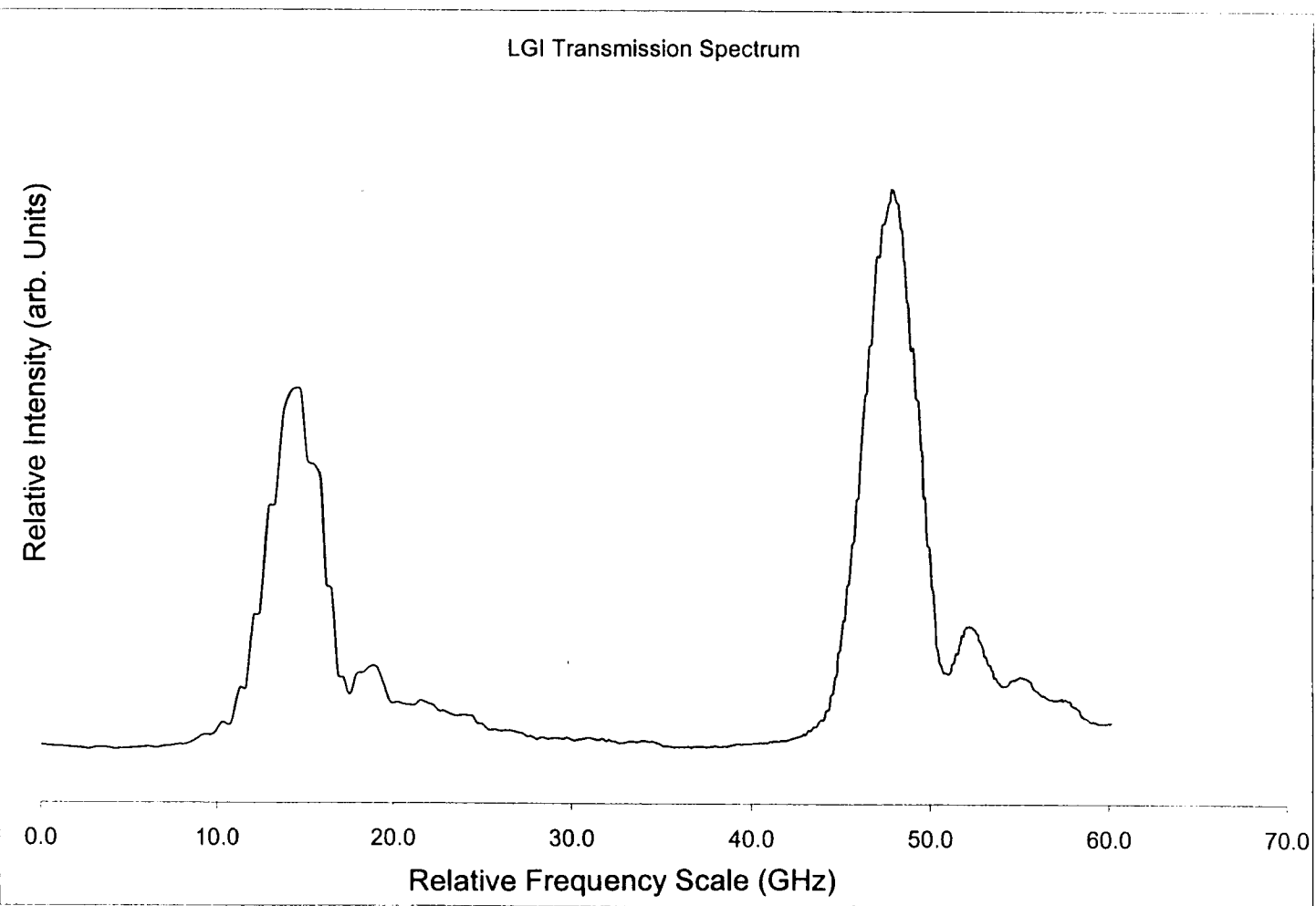


Figure 4.4 Measured transmission spectrum of LGI. The fringe magnitudes of the two shown are unequal due to laser intensity considerations during the scanning.

heterodyne spectra, its presence did not effect our measurements. Further details concerning the LGI are covered in section 3.3, and appendix A.

4.4 Detector Circuit

The complete detector circuit consists of three photodiodes, as shown schematically in Figure 4.5. Two photodiodes are the RF and DC detectors, respectively. The third detector is the on-board photodiode built-in to the diode laser. This detector measures the photocurrent resulting from the intensity of the laser emission. It is used for real-time monitoring of the laser power.

As indicated in Figure 4.1, a beamsplitter guides the laser light into two electronically independent photodiodes, one for radio-frequency (RF) measurement of signal noise, and the other to measure the time-independent (DC) component of light intensity. The DC photodiode is a Thor Labs (Model DET2-SI) detector, with an active area of 1 mm-squared. To achieve a spectral resolution of approximately 80 MHz, an aperture of 100 microns is placed in front of each photodiode, during the current tuning of diode laser frequency through a LGI transmission resonance. The DC photodiode is operated in a reverse-bias mode at 22 volts. For oxygen work, the RF photodiode is a 3 GHz, Antel Optronics' Model AR-S1 ultra high speed photodetector. It is reverse-biased at 100 volts. This fast photodiode, as it will be called in this paper, has an active

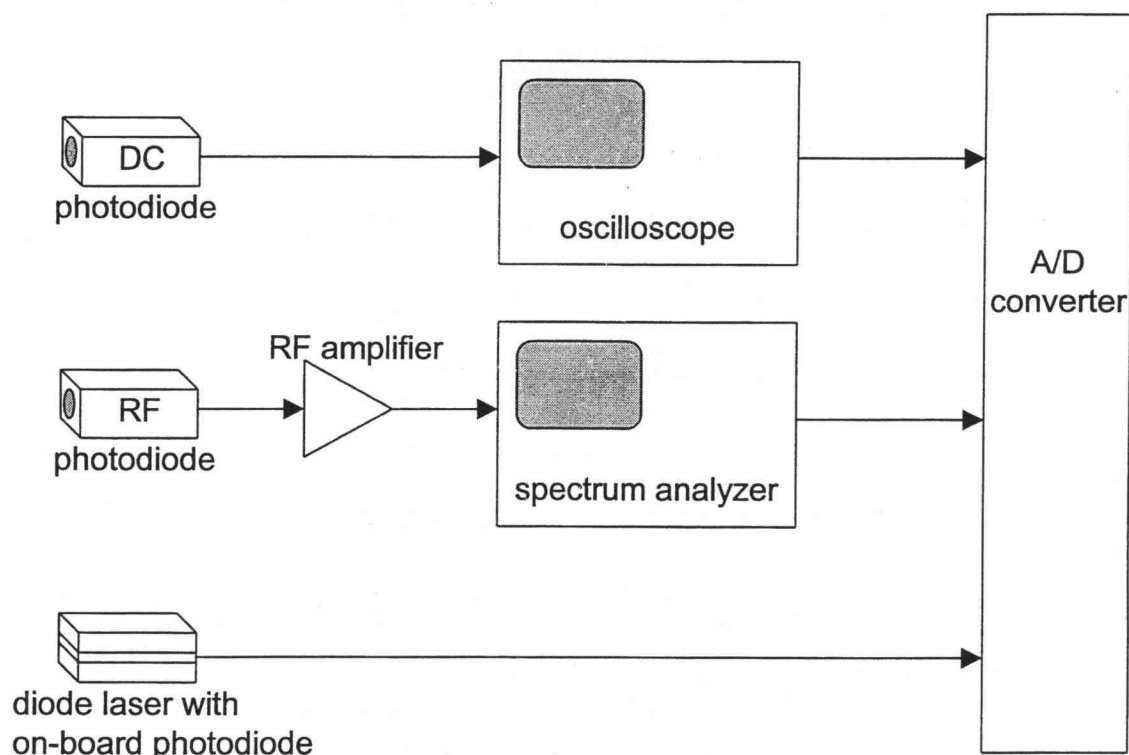


Figure 4.5 Photodetector description of apparatus circuit

area of .25 square millimeters. For LGI measurements, the RF photodiode is the same type that is used for the DC detection, since the light intensity of the LGI output is too small for the Antel to measure. Using the slower Thor labs detector means that our LGI heterodyne measurements are limited to spectrum analyzer frequencies less than about 20 MHz. Also, the RF detector is placed about 10 cm away from the output end of the LGI.

Because the light output of the LGI, intercepted by the RF detector, is too small to measure a heterodyne signal, we use an RF amplifier, indicated in Figure 4.1, for all LGI measurements. This amplifier has a gain of approximately ten.

The photocurrent of the RF photodiode is measured as a voltage drop across the 50-ohm input resistance of a radio frequency spectrum analyzer (Hewlett-Packard, model 8500 series). During heterodyne measurements, the spectrum analyzer is operated as a tuned receiver, measuring a single Fourier component of the heterodyne noise spectrum. Desired RF frequencies are those which avoid local radio and television broadcasting and other local sources of spurious RF signals. The photocurrent of the DC photodiode is measured as a voltage drop across a 10 k-ohm resistor. Subsequently, both RF and DC information are stored in a computer, via a computer A/D board, for processing later. To ensure avoidance of optical feedback into the diode laser, both photodiodes are mounted so that the angle between the axis (normal to the photodiode surface) and the incident optical path is about 5° .

It was discovered, by trial and error, that the roles of the two photodiodes, RF and DC, could not be accomplished by a single photodiode. Apparently, any electronic coupling of the RF spectrum analyzer input with the oscilloscope input will result in the addition of large amounts of unwanted noise across the radio spectrum, indicated on the spectrum analyzer. To this end, much effort was made at having two photodiodes intercept the same part of the L-G spectrum.

4.5 Diode Laser Drive Circuit

The drive circuit is a very rudimentary circuit that allows minimal control over the diode laser. Designed with the philosophy, "the simpler the better", nonlinear

circuit components, and contact switches, were avoided to help ensure that damaging current or voltage transients into the diode laser would not be possible. Typically, a diode laser drive circuit is designed to allow slow turn-on of the operating current. In this section, the procedure used to bring the diode laser to the chosen operating current is described.

The drive circuit is shown in Figure 4.6. Two large, 12 volt, rechargeable batteries power the circuit. The laser drive circuit's independence of the utility-power line circuit helps to ensure that no artifacts, such as noise harmonics from

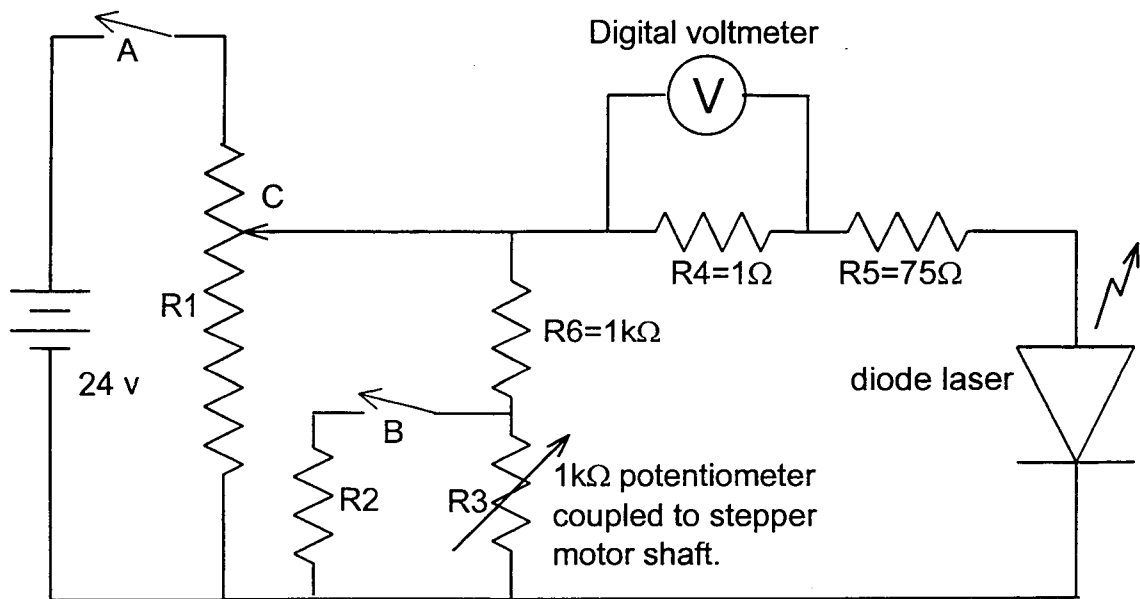


Figure 4.6 Drive circuit for diode laser.

virtually anything in the lab or building, are present in the laser current. The resistor, R_1 , is a 1200 k Ω , rheostat. When the circuit is off, R_1 is adjusted so the contact at point C is at the grounded end of R_1 , making the voltage at point C, V_C , equal to zero. The current to the diode laser is safely turned on in two steps: First, switch A is closed, with $V_C = 0$. Second, V_C is slowly turned up, using R_1 , until the desired diode laser current is reached. The turn-off procedure is the reverse of the turn-on procedure. The value of R_1 is unchanged while operating the diode laser during experiments.

After the desired diode laser current is achieved with adjustments to R_1 , the value of a potentiometer, R_3 , is changed to make fine adjustments to the laser current, as may be the case for current-tuning to a particular laser wavelength. The laser current can be scanned over a fixed range, roughly 45 to 55 mA, by repetitively changing the resistance of R_3 . R_3 is a rotational potentiometer, and its shaft is mechanically coupled to the shaft of a computer-controlled stepper motor. Thus the resistance of R_3 is controllable by a computer, and, therefore, so too is the diode laser current. Details of the correlation of current changes with data acquisition are deferred to a later section.

The value of R_2 determines the range of the current scan of the diode laser. Further, the resolution of the heterodyne spectra is related to the current scan range since the smallest change to the diode laser current is limited by the stepper motor's smallest rotation angle. For all our work using this drive circuit, only two current ranges were used, so R_2 is fixed at 100 Ω for a current range of

2 mA, centered at 50 mA. When switch B is open, R2 is effectively infinite, giving a current range of 10 mA, centered at 50 mA.

The diode laser current is monitored by a voltmeter in parallel to a $1.00\ \Omega$ resistor, R4 in Figure 4.6. This digital voltmeter is an inexpensive, battery-powered unit with high input impedance. R5, and R6 are current-limiting resistors that have fixed values.

Adjusting laser current by the computer-operated stepper motor control of the potentiometer resistance, R3, maintains drive-circuit isolation by avoiding the typically used ramping function generator that is coupled into the circuit via an FET or BJT.

4.6 Computer Control

An 80286, IBM-compatible personal computer is used for experiment control and data acquisition, using a Data Translation computer I/O board. The I/O board allows analog-to-digital conversion, digital-to-analog conversion, and direct output of digital voltage levels. Using the A/D conversion, the photodiode information from the experiment is entered into the computer and stored. The direct output of the computer board is used to control the steps and direction of the stepper motor.

A single computer program is used to set the diode laser current parameters for a spectral scan, spectral resolution parameters, and type of data acquisition. A value for the center of the diode laser current range is manually chosen by

properly adjusting the resistor R1, as explained in the previous section. Then the lower and upper limits of the current range are chosen, by using the computer program. The program determines the number of stepper motor steps that corresponds to the desired current range of the diode laser. Also, several parameters that determine spectral resolution, and data averaging statistics, are established using the program. The choices for data acquisition method, using the program, include spectral scanning by changing the current of the diode laser, and digitally recording the spectra analyzer's CRT output. Using the computer program, the spectral scanning is automatically performed over the entire scanning range, or the scanning can be done manually, one stepper-motor step at a time. In either case, a data acquisition sequence consists of a stepper motor step, followed by a wait, and then input to the computer of DC and RF photocurrent data.

All spectroscopic data, and diode laser parameters, for a scan are stored in a single computer file on the computer's hard drive. Later, the files are copied, and stored in an 80586-type personal computer, where the data is analyzed using spreadsheet-type software.

During a scan, the computer screen displays real-time spectra, and the rotation step number of the stepper motor, corresponding to the diode laser drive current.

Details of the computer program are in Appendix C.

4.7 Spectral Scanning Method

We will now describe the method used for scanning the diode laser through oxygen A-band absorption lines, and the slightly different procedure used when scanning the diode laser across an LGI resonance.

For oxygen spectroscopy, the diode laser's wavelength is temperature-tuned to the region near an absorption line to be studied. For the specific diode laser used, the temperature of the laser was heated to about 39°C. The diode laser frequency is then scanned across the absorption line, by current-tuning, while the temperature is held constant. The current tuning method, and data acquisition sequence are explained in the previous section. The limit of the spectral range of the scan is approximately .12 nm (60 GHz at 760 nm), or .01 nm (5 GHz), if switch B (Figure 4.6) is opened or closed, respectively.

For LGI spectroscopy, the methods used are the same as for oxygen work, except that the combination of diode laser temperature and current are chosen so that atmospheric oxygen absorption lines are avoided.

From analysis of the circuit in Figure 4.6, it is realized that a linear change in the value of R3 results in a nonlinear change to the diode laser drive current. Thus, the diode laser current is nonlinear in stepper motor steps. For a scan range of 20 GHz, the minimum optical frequency change per stepper motor step, occurring at the high-current end of a scan, is approximately 10 MHz. The step size for the low-current end of the scan is approximately 200 MHz. Overall, laser stability averages ± 0.025 GHz at any point during the scan.

At the data analysis stage, RF and DC signal strength, measured as a function of non-linear diode laser current, is converted to RF and DC signal strength as a function of linear frequency of the diode laser. The conversion is performed by utilizing the known frequency separation of two measured O₂ A-band absorption lines, the same two lines that are investigated in chapter 5, with diode laser intensity data obtained from the onboard diode laser photodiode. In order to perform this conversion, the diode laser frequency is assumed to vary linearly with the laser intensity, which, in turn, varies linearly with the laser current [Wieman, et al., 1991]. This linearization procedure takes advantage of the fact that the 760 nm diode laser used in the work of this paper can be wavelength-adjusted to encompass two atomic transitions with a separation that is less than our scanning range, without including a mode-hop, as pointed out in section 4.1. By counting the number of stepper motor steps between the two lines, the corresponding frequency separation gives a conversion factor that allows conversion from step number to frequency.

In addition to the linearization of the horizontal axis, described above, the vertical scale must also be modified. As the diode laser's drive current is increased to increase its wavelength during a scan, the output power also increases. As a result, the measured RF and DC signal strength have a direct spectral dependence due to the changing laser power. To eliminate this direct effect of varying laser power, the final spectra are the plots of RF and DC signal strength data respectively divided by the onboard photodiode intensity data, versus frequency.

The spectral stability of our diode laser circuit was measured by configuring the drive circuit to the high-resolution capability. Then, when scanning near the peak of an absorption line, the scan process was paused for 500 seconds. Once the scan is continued, a shift in the spectrum, which represents the spectral drift, is measured. An example of this process is displayed in the spectrum of Figure 4.7. The net drift is around 0.2 MHz per second. For most of the spectra shown in this thesis, the absorption line was scanned in a period of less than a minute, and so the drift during a scan may be approximately 10 MHz. This is a small fraction of the line's FWHM, so spectral distortion should be negligible.

4.8 Radio Frequency Spectrum Analyzer

A spectrum analyzer (SA) allows a measured signal to be analyzed in frequency space. The SA generates an oscilloscope-type display, with the vertical axis measuring signal strength, and the horizontal axis measuring frequency. A radio frequency spectrum analyzer (RFSA) is a SA that functions in the radio frequency part of the electromagnetic spectrum, defined as the range from zero to several GHz. The type of SA we used in our work is the swept-tuned variety. It works on the principle of heterodyne detection, similar to a FM radio receiver. Shown in Figure 4.8, the SA consists of a local oscillator, which is mixed, or heterodyned, with the input signal. The local oscillator frequency is swept over the frequency range of the SA by an internally generated ramp waveform. This frequency ramping allows different input frequencies to be

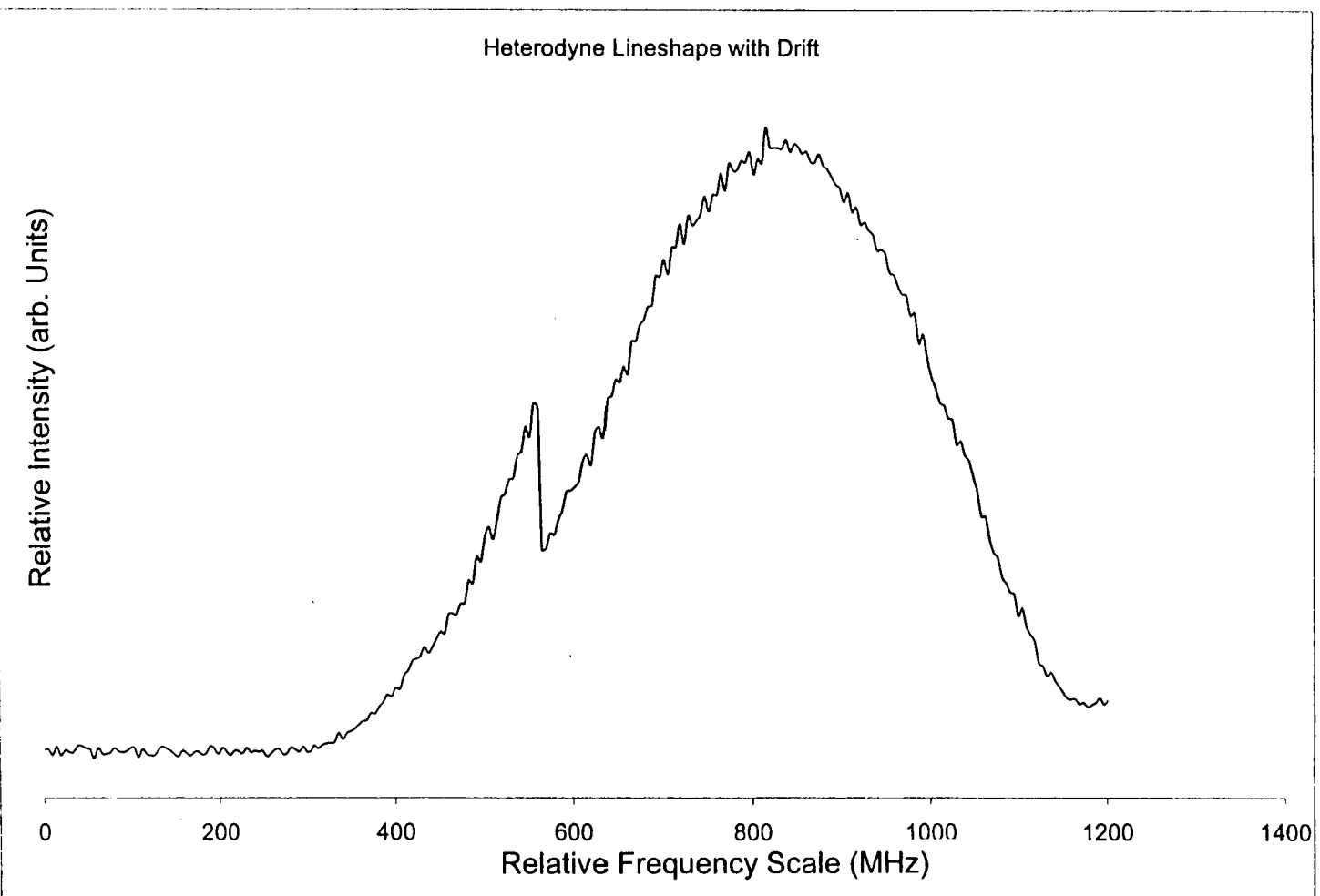


Figure 4.7 Half a heterodyne lineshape showing spectral drift when the measurement process was paused for 500 seconds.

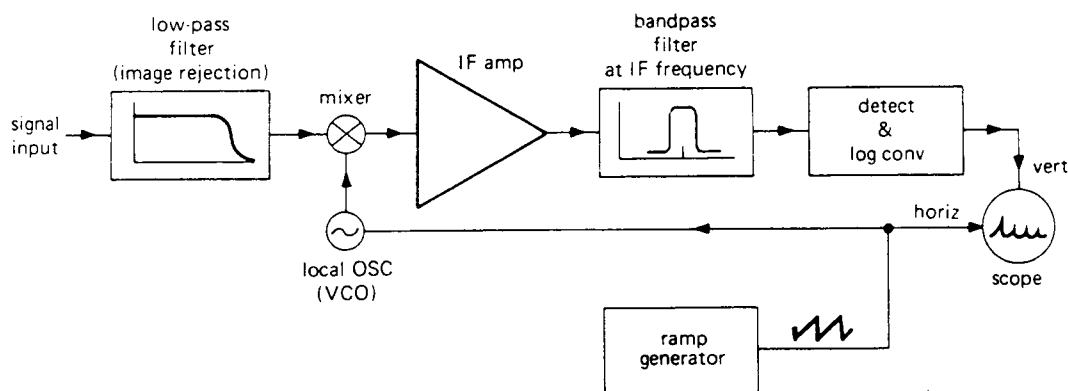


Figure 4.8 Radio frequency spectrum analyzer.

successively mixed. The resulting heterodyne signal is only amplified if it is within the bandpass range of the SA's fixed-frequency intermediate frequency (IF) amplifier. The idea behind this scheme is to use a mixer and local oscillator to shift the input signal, with a variable frequency, to a fixed IF frequency where all amplification and selectivity are concentrated. A low-pass filter at the input stage is needed, for image-frequency (local oscillator plus IF) rejection. The output of the SA is a vertical deflection on the CRT, and a proportional voltage on an external jack.

Typically, and in our case, the bottom 1% of the SA spectrum range is not useable: Low frequency sources from the electronics within the SA abound, with

intensities relatively much stronger than what is usually measured at higher frequencies. This results in a finite-width delta function at zero-frequency on the SA scale.

The SA used in our work is a model HP 8500. It incorporates different RF sections, or modules, depending on the frequency with which we chose to work. The three RF sections had a range from zero to 110 MHz, zero to 1250 MHz, and zero to 2100 MHz, respectively.

Depending on the type of measurements, the SA was operated in one of two different modes: 1) Full spectral range, and 2) Fixed frequency. The full spectral range gives spectra that are the full width of the RF section in use. These spectra were useful for measuring noise of the diode laser emission, and for various diagnostics and system checks. The latter involved checking for unwanted optical external-cavity resonance due to feedback, and RF noise from an outside sources, such as a local radio station. Noting the frequencies of outside source noise enabled us to avoid performing measurements near these frequencies. Also, any optical cavity resonance would appear on the SA CRT as a narrow spike with a frequency determined by the round-trip condition of the cavity, given by $\nu = c / 2L$, where c is the speed of light, and L is the cavity length. The SA can also detect the harmonics of this resonant frequency. For our optical setup, typical resonant frequencies were of the order of 10^7 Hz. When a cavity is observed, something is done to alleviate it, like tilting an optical component, as described in section 4.3.

For heterodyne spectroscopy measurements, the SA was operated in fixed-frequency mode, like a tuned receiver. As explained in the paragraph above, tuned frequencies are chosen to avoid those of local radio and television broadcasting and other sources of spurious RF signals.

The RF spectrum analyzer sensitivity was always set to the highest level which does not clip the signal at the largest value of a scan.

CHAPTER 5: EXPERIMENT RESULTS

5.1 Lummer-Gehrcke Interferometer Heterodyne Spectra

5.1.1 NIR Diode Laser Spectra

When measuring LGI heterodyne spectra, the temperature of the 760 nm diode laser is chosen to ensure that the emission is spectrally far from any atmospheric oxygen absorption lines. The diode laser's emission is scanned over a 55 GHz range, by varying the laser's drive current between 45 and 55 mA.

Figure 5.1 shows a LGI heterodyne spectrum of the NIR diode laser, along with the DC transmission spectrum. The RFSA was tuned to 5 MHz, with a bandwidth of .3 MHz. Figure 5.2 shows the laser's emission spectrum for these conditions, indicating that the diode laser was operating in a single mode.

These m-shapes are symmetric, and the central minimum goes to zero, indicating that the emission of this diode laser obeys the phase-diffusing model. On the high-frequency side of each large m-shape, there is a small m-shape attributable to the ghost of the LGI, explained in section 4.3.

The m-shape height symmetry shown in Figure 5.1, indicates an absence of amplitude noise. If any amplitude noise is present in the diode laser emission, then the m-shape will exhibit asymmetry in the height of its peaks, which has

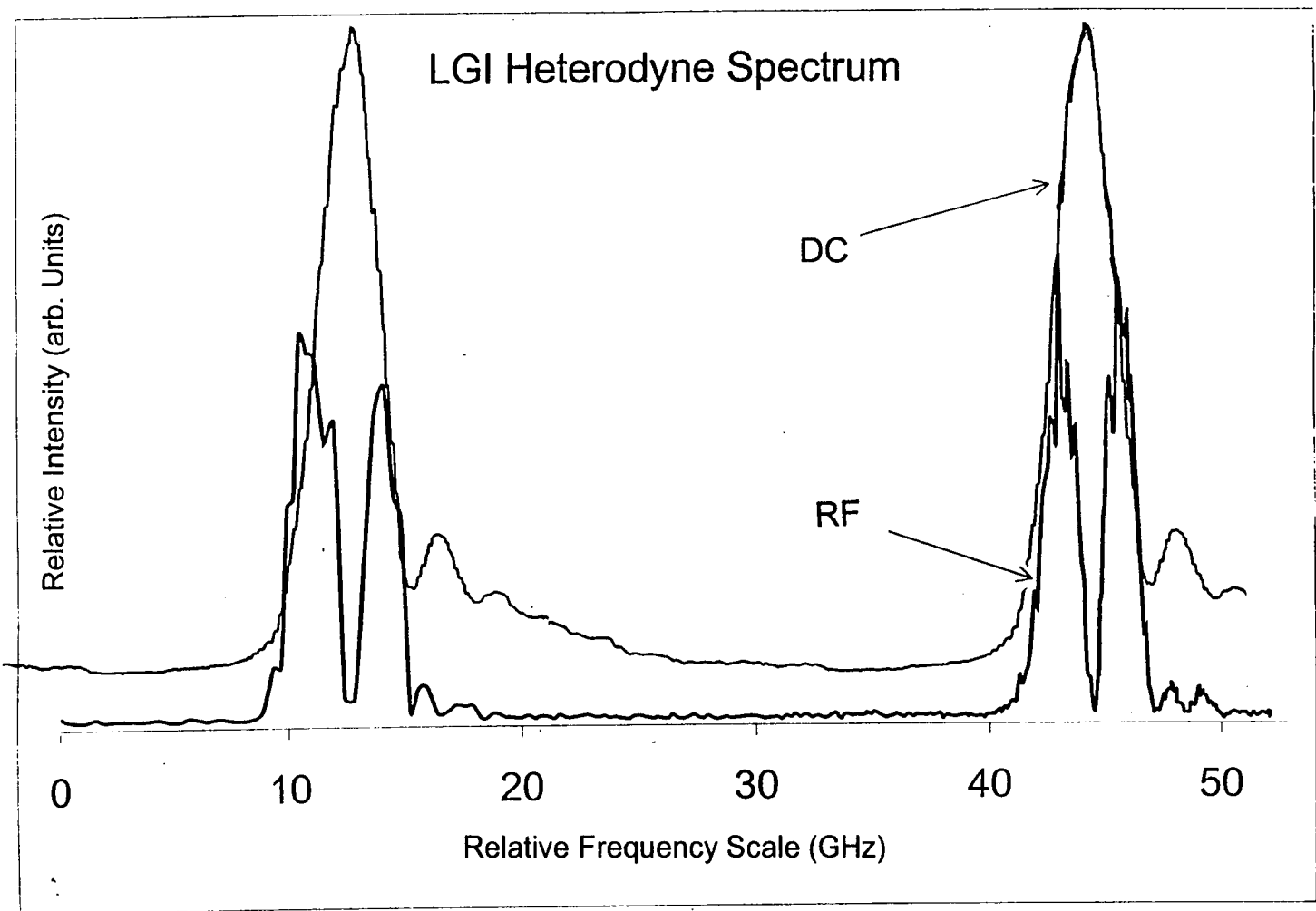


Figure 5.1 LGI heterodyne spectrum of the 760 nm diode laser. The DC transmission spectrum is shown for reference

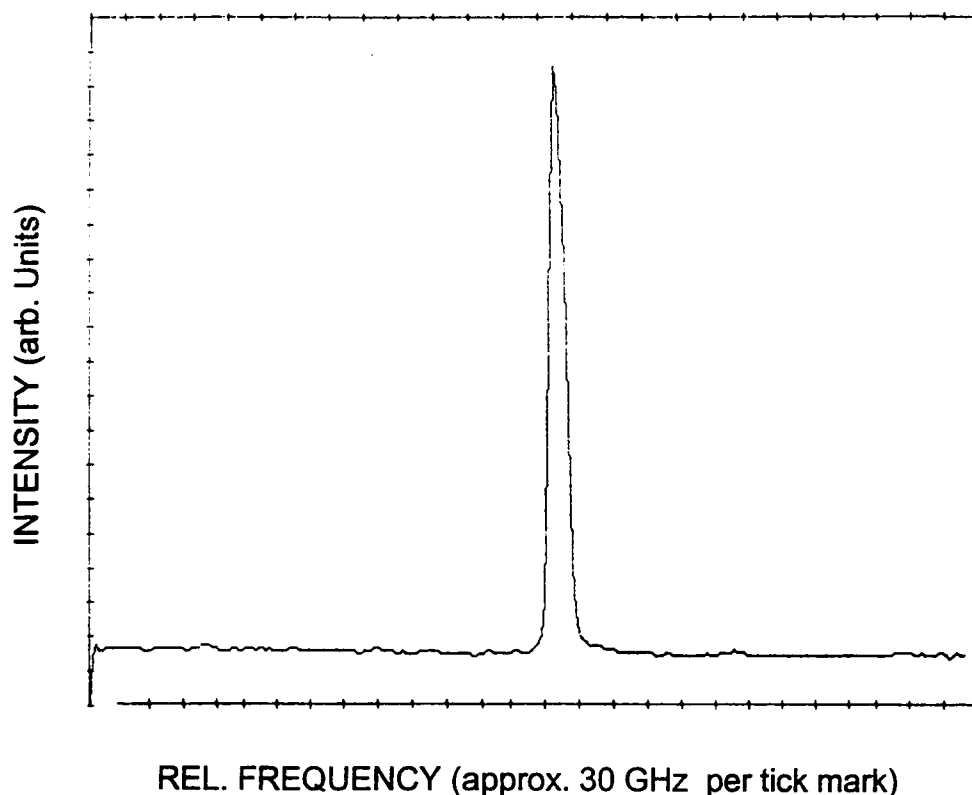


Figure 5.2 Diode laser emission spectra for the heterodyne data shown in Figure 5.1.

been reported for heterodyne spectra, with an amplitude-noisy diode laser, of a Fabry-Perot cavity [McIntyre, private communication].

We have performed measurements of amplitude noise for the 760 nm diode laser which was used for the heterodyne data presented here, using the setup shown in Figure 5.3, and we found no measurable amplitude noise over the frequency range from 0 to 3 GHz. To verify our capability to measure amplitude noise, the amplitude noise for a 670 nm diode laser, operating at a power level of 6.6 mW, was measured by the same method as for the 760 nm diode laser. The result is shown in Figure 5.4. This measured noise spectrum extends from 0 to 3

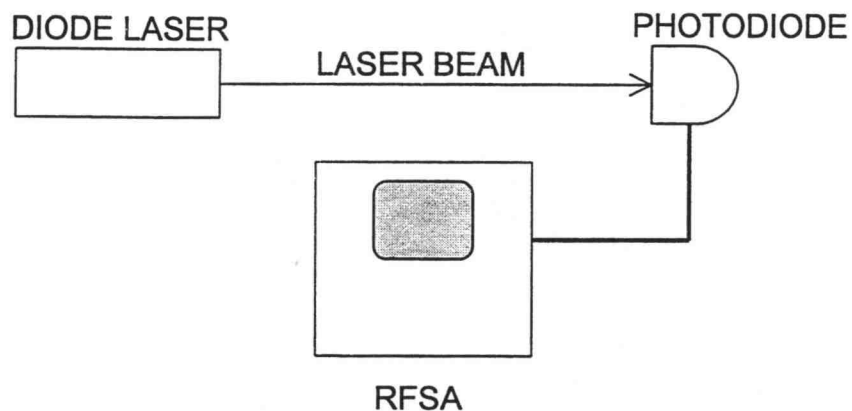


Figure 5.3 Apparatus used for measuring diode laser amplitude noise.

GHz, although Figure 5.4 only shows the range from 1.4 to 1.8 GHz, where the only nonzero signal occurred.

The large peak in the amplitude noise distribution is at the possible relaxation oscillation (RO) frequency of this diode laser. The large difference between the amount of amplitude noise for the 760, and 670 nm, diode lasers was expected, as noted at the end of section 2.5.3.

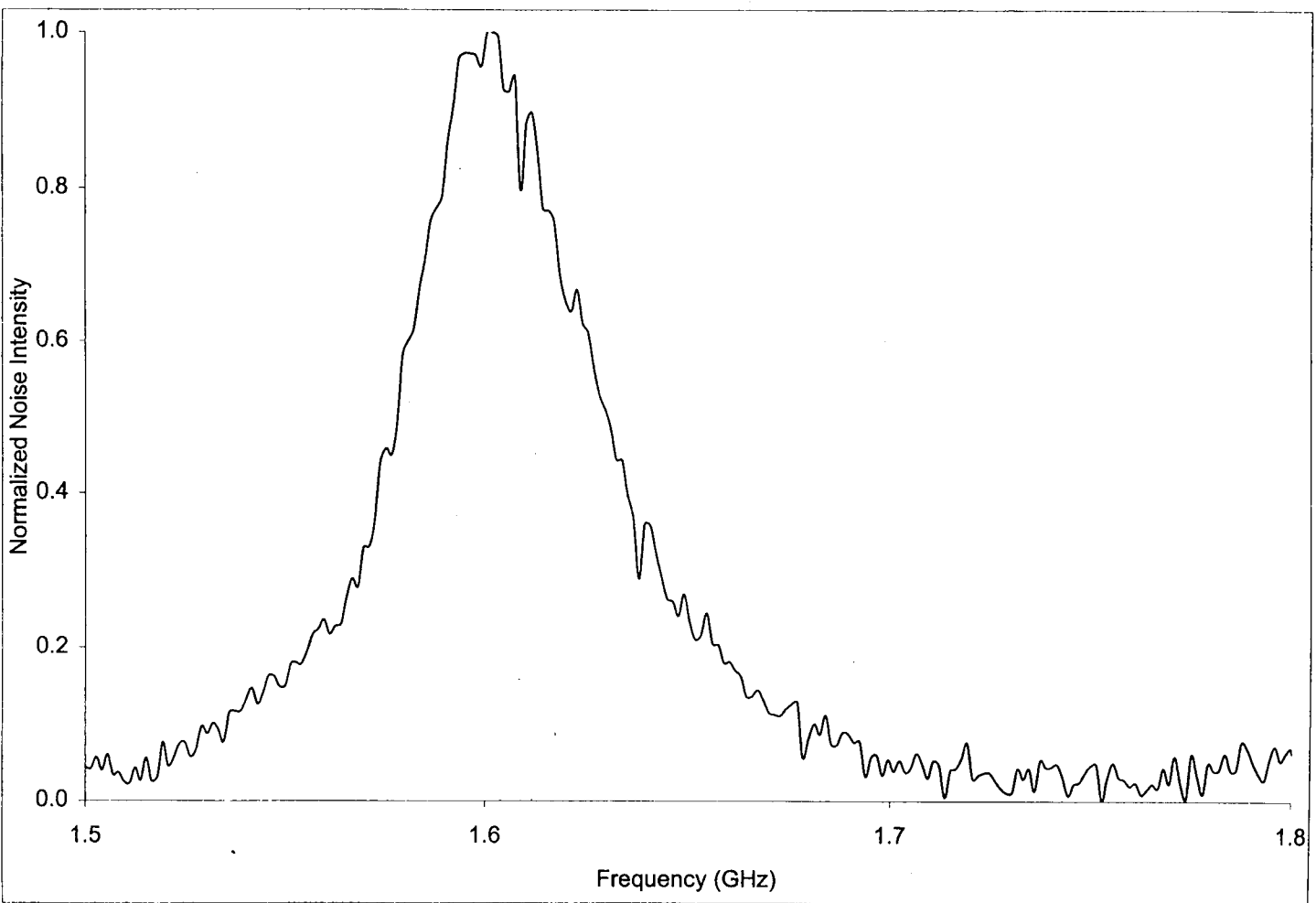


Figure 5.4 Amplitude noise spectrum for a 670 nm diode laser, operating at a power level of 6.6 mW.

5.1.2 Visible Diode Laser Spectra

For a general comparison to the LGI heterodyne spectrum of the NIR diode laser, LGI heterodyne spectra of the visible diode laser, the same one presented above, were measured for laser power levels ranging from 1 mW to 9.6 mW. Two of these spectra, at laser powers of 6 and 8 mW, respectively, are shown in Figure 5.5, along with the DC transmission spectrum. The spectrum analyzer was tuned to 10 MHz, with a bandwidth of .3 MHz. Relatively large linewidths, associated with noisy laser emission, are indicated in these heterodyne spectra several different ways. It is well-known that diode laser linewidths typically become narrower as the diode laser operating power is increased beyond its current threshold. Also, secondary longitudinal emission modes, of the diode laser, diminish as the power is increased. This is clearly seen by comparing the 6 and 8 mW spectra. In between the principal-mode fringes, secondary-mode fringes are present. Moreover, the secondary-mode fringes are more pronounced at the lower, 6 mW, emission power. These modes can also be seen in the emission spectrum of the diode laser, which was recorded during the measurements of Figure 5.5, shown in Figure 5.6. Also, across the spectrum the heterodyne signal is larger for the lower power, indicating an overall larger level of phase and amplitude noise for this operating power. Because of the complicated superposition of fringes, it is not obvious what affect the DC 'ghost' has on these heterodyne spectra.

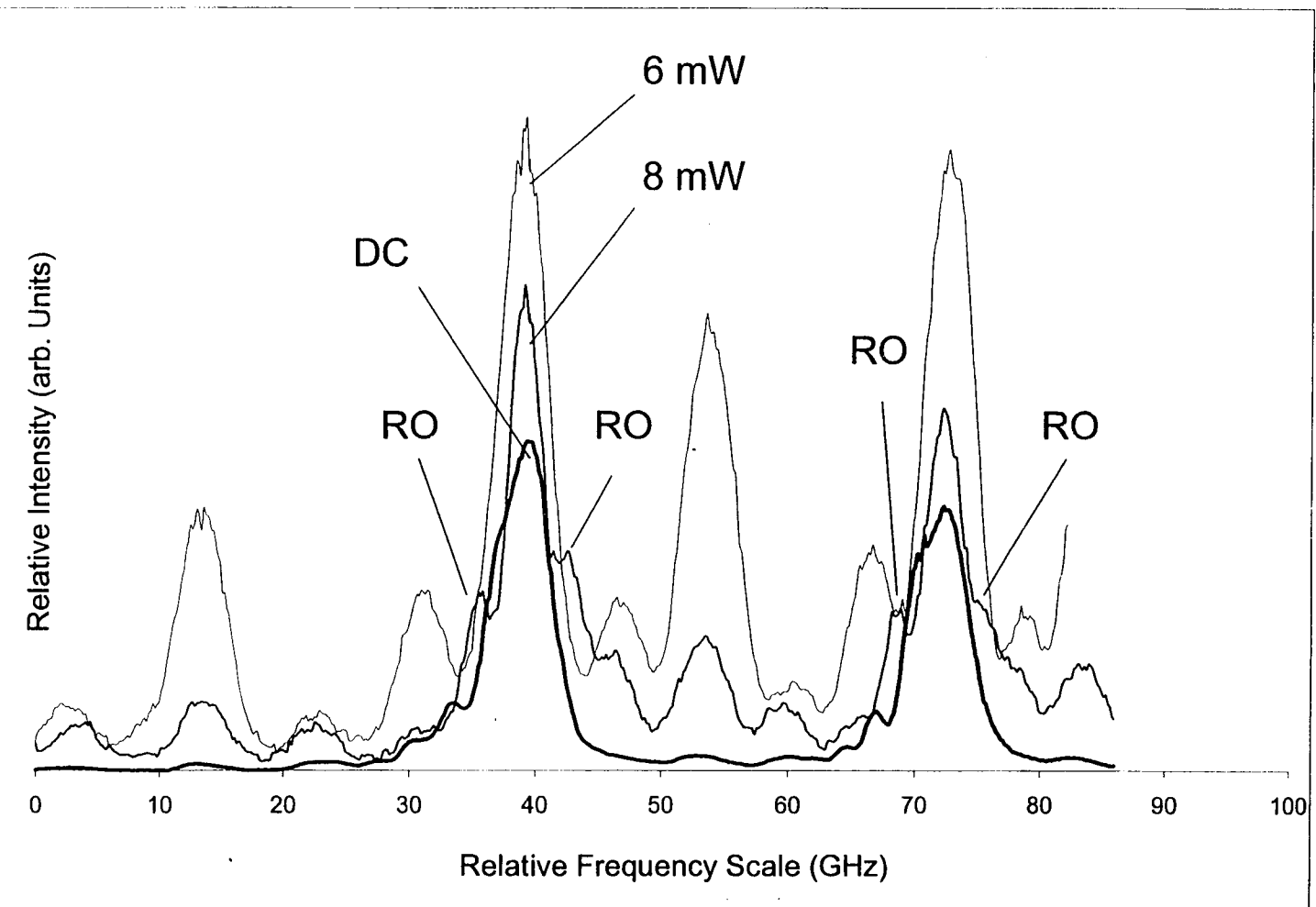


Figure 5.5 Heterodyne spectra for a 670 nm diode laser, for two emission power levels. The transmission spectrum (DC) of the LGI is also plotted. Relaxation oscillation (RO) peaks of the 8 mW spectrum are noted.

As is the case for both laser powers and emission modes in Figure 5.5, the lack of a central minimum in these heterodyne spectra may demonstrate that a relatively large amount of noise (large linewidth) exists in these laser emissions. This conclusion may be explained by noting that equation 3.6 only gives a small central minimum for small $\Delta\phi$, otherwise the small angle approximation cannot be used, and additional time-dependent terms will add to equation 3.6 which aren't zero at line center.

Due to the visible diode laser's emission containing many modes, the LGI spectra become a complicated superposition of primary and secondary transmission fringes. Difficulties arise since the free-spectral-range of the laser and LGI are near-multiples of one another, causing the consecutive laser modes' fringes to occur at, or close to, the same spectral locations, obscuring the true spectral widths and shapes of these fringes.

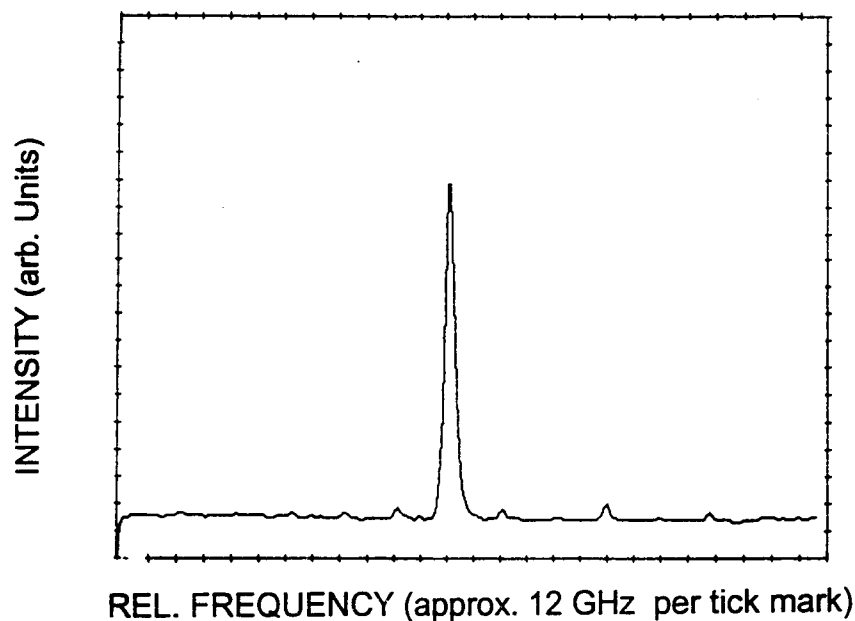


Figure 5.6 Diode laser emission spectrum for the case of Figure 5.5.

In Figure 5.5, relaxation oscillation (RO) peaks are observed on the shoulders of the 8 mW principal fringes. We have observed these RO peaks only at diode laser powers greater than 7 mW. Below this power, the RO frequency is small enough that the RO peaks exist within the main fringe, and they are obscured. At higher laser powers, the RO peaks move away from the fringe center, as the RO frequency increases. This behavior for RO's is expected [Vahala, et al., 1983, and Agrawal, et al., 1988], as will be recalled in section 2.5.3. This fact, along with the observation that these small peaks are larger on the high frequency side of the fringe, is convincing evidence that these are indeed RO's. The RO of the 8 mW spectrum is approximately 1.6 GHz away from fringe-center. This is the same frequency of the peak in the amplitude noise spectrum that was measured for this laser, operated at 8 mW, shown in Figure 5.4. This helps to verify the fact that the peaks on the shoulder of the fringes in Figure 5.5 are RO's.

5.2 Oxygen Heterodyne Spectra

The experimental apparatus for oxygen heterodyning is discussed in Chapter 4. We used a pressure of $\frac{1}{2}$ atm, as it has the best combination of heterodyne signal strength and freedom from excessive pressure broadening effects. Gas pressure in the sample cell is measured with an inexpensive mechanical manometer that has been calibrated using a mercury manometer.

For the work of the present paper, two absorption lines of the oxygen A-band are measured. These transitions, RR(15,15), and RQ(13,14) [For notation description, see Ritter, et al., 1987], separated by 14 GHz, are at 760.01 nm, and 760.05 nm, respectively. At room temperature, these lines have a Doppler width (FWHM) of 930 MHz. At $\frac{1}{2}$ atm, the pressure broadening gives a measured linewidth of 1.2 GHz (FWHM). This linewidth was measured using a DC absorption spectrum, as in Figure 5.7, from one of the heterodyne scans, which are presented below.

For each line, absorption of 9% was measured for the 2-meter long oxygen cell. The absorption contribution from oxygen outside the cell, but in the optical path of the laser, is estimated to be approximately 1%.

As for LGI measurements, to record spectra for oxygen, the RFSA frequency is fixed, so it acts as a tuned receiver. The diode laser is temperature-tuned close to the absorption region of interest, and the diode laser frequency is scanned across the absorption line, by current-tuning, in the same manner as for LGI measurements. For the data presented, the diode laser temperature is approximately 38.5°C.

Figure 5.7 shows a heterodyne spectrum of the RQ(13,14), and RR(15,15) oxygen transitions, and the reference absorption spectrum for comparison, for a 100 MHz RFSA frequency. The strength of the RR(15,15) heterodyne profile is less than the RQ(13,14) transition because the diode laser emission power is lower when at resonance with the former transition, since this transition is scanned at a lower drive current. However, the vertical scale has been adjusted

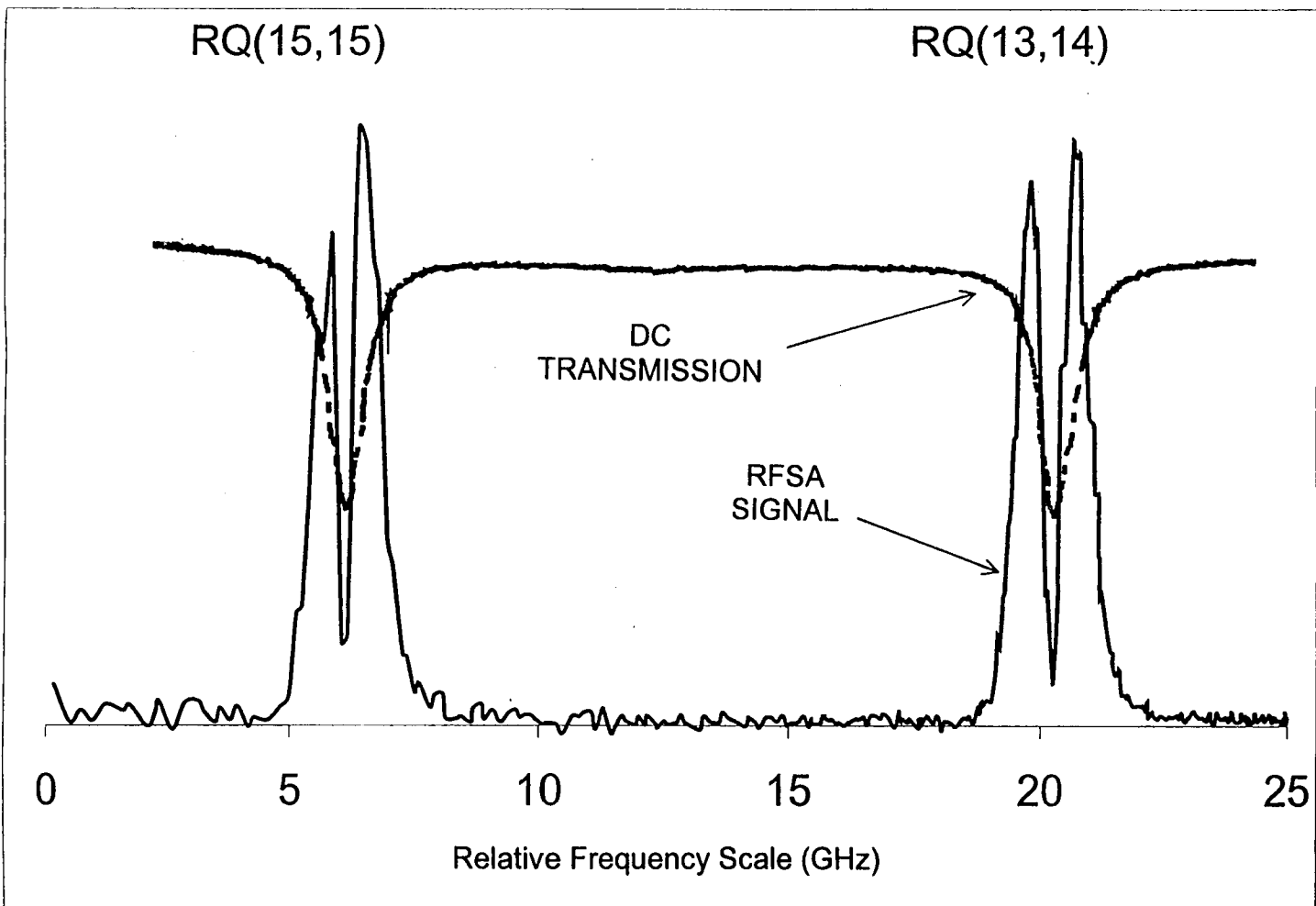


Figure 5.7 Heterodyne spectrum showing two oxygen transitions, as noted in the figure. The scanning resolution of the RQ(15,15) line is less than it is for the RQ(13,14) line, resulting in decreased apparent magnitude.

for the current-scanning affects as described in section 4.7. In addition, the spectral resolution of the two-transition scan is nonlinear, due to the current-changing scanning method, also mentioned earlier in section 4.7, for the case of LGI heterodyning. Thus, the spectral resolution of the RR(15,15) transition is less than it is for RQ(13,14) transition.

Several noteworthy features of the spectrum in Figure 5.7 are the relatively deep central minimum of the m-shape, the symmetry in the height of the two peaks of the m-shape, and the lack of RO peaks. These features become more striking when this spectrum is compared to the spectra of earlier measurements by other workers [McIntyre, et al., 1993, and Fairchild, et al., 1993], which is presented in figure 5.8. The heterodyne profile for oxygen, measured by Fairchild et al [1993], disagrees with the PDM theory, because its central minimum is greater than predicted, and there are subsidiary maxima in this spectrum. In addition, this spectrum clearly shows first order RO peaks, and perhaps even higher orders. The diode laser used for the Fairchild, et al., [1993] measurements is known to have a larger linewidth than the one used for the work of this thesis [Fairchild, private communication]. Consequently, more amplitude (and phase) noise is present in the emission of this earlier laser, as is demonstrated by the large RO's. In section 5.4, data will be presented that show qualitatively similar spectra for the case of Fresnel feedback into the diode laser. The m-shapes of McIntyre, et al., [1993], shown in Figure 5.8, have an asymmetry that is believed to be from the fact that the rubidium transition is not a two-level transition, and the PDM-based heterodyne theory assumes a two-level system, as explained in

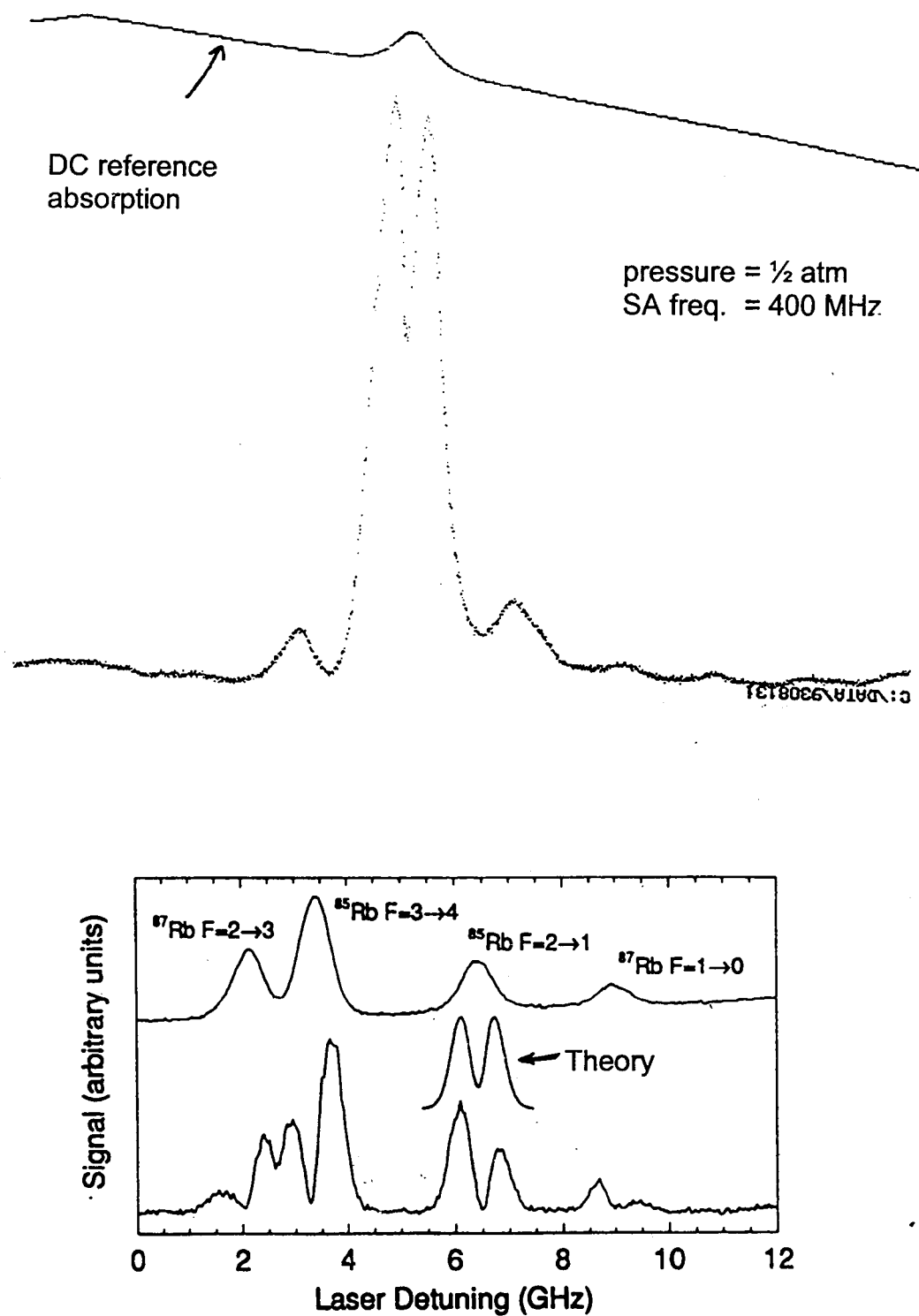


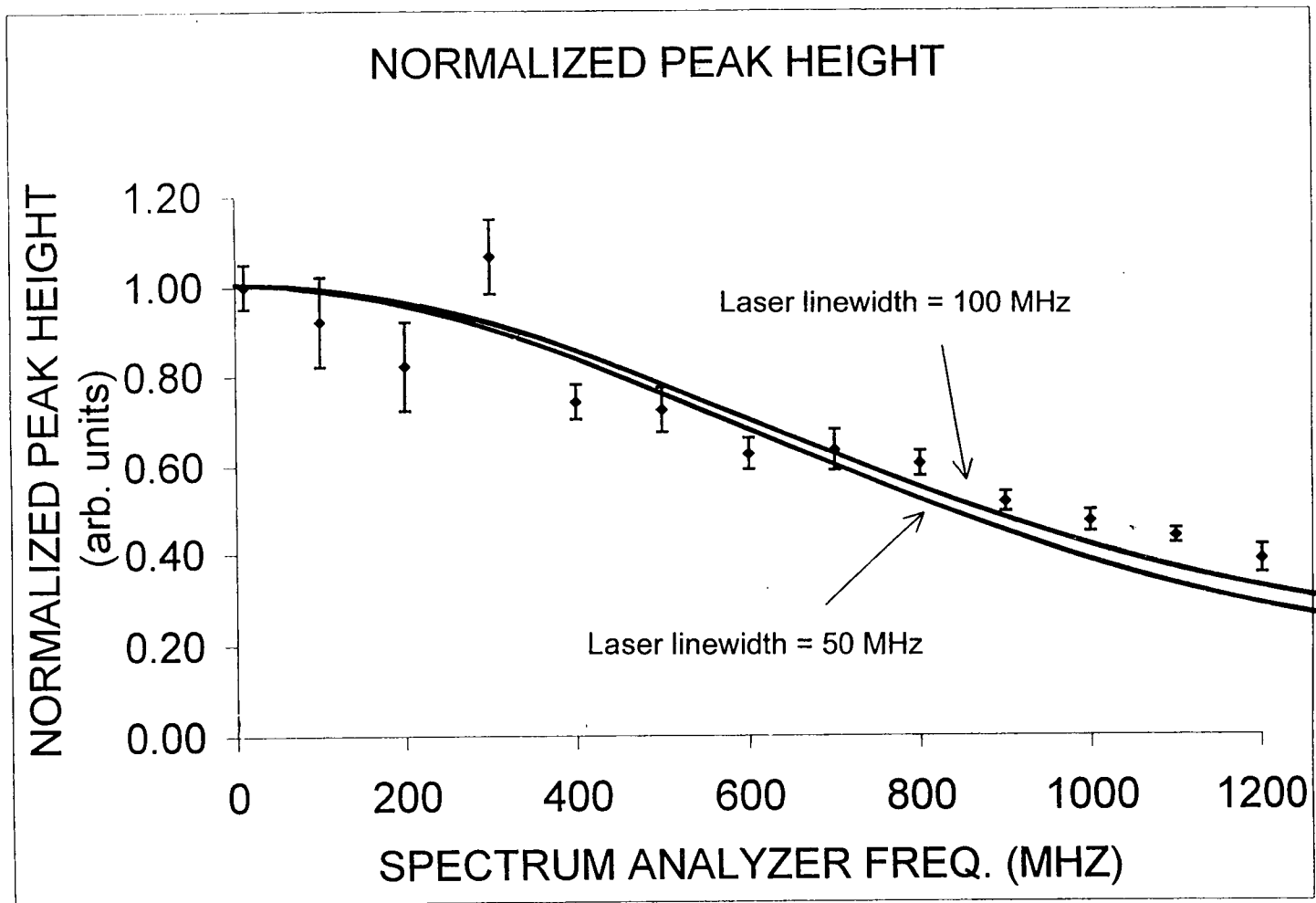
Figure 5.8 Previously reported heterodyne spectra for oxygen (Fairchild, et al., 1993), top, and rubidium (McIntyre, et al., 1993), bottom.

Chapter 1. Also reported in their work is asymmetry due to correlated intensity and phase noise. Their rubidium heterodyne spectrum also disagrees with the theoretical value for the central minimum, which is indicated by the theoretical lineshape shown in the figure.

For the following analysis of measured oxygen heterodyne spectra, we have concentrated on a single transition. The RQ(13,14) transition was used, since it has a stronger heterodyne signal, and higher resolution, than the other measured transition, RR(15,15). Spectra as a function of laser detuning were taken for values of the RFSA frequency from 10 to 1200 MHz. Each noise spectrum was characterized by the peak height, FWHM, center-to-peak-center width, central minimum height, and asymmetry of the heterodyne resonance. Before this analysis, the vertical scale of these spectra is adjusted for diode laser intensity changes during scanning, as explained in section 4.7. A Lorentzian curve-fit was used to determine these heterodyne parameters as follows. For a given m-shape, each of the individual peaks of the double-peaked heterodyne spectrum was best-fit to a Lorentzian by including only the portion of the peak that is equal to or above the central minimum value. For the resolution of the lab data, each best-fit included approximately 35 data points. From these best-fit curves, only the high-frequency peak of the m-shape was analyzed for all the parameters, with the exception of the asymmetry value. In analyzing this peak, the height was taken as the maximum value, the width is the FWHM, the center width is the

distance from the m-shape center to the center of this peak, and the central minimum height is the y-axis value of the m-shape at the center frequency. The asymmetry is defined as the ratio of the difference to the sum of the peak heights of the two peaks of the m-shape, with the leading term in the difference being the high-frequency peak height. Figures 5.9 through 5.13 summarize these results, and compare these experimental data to the PDM-based heterodyne theory for oxygen for two laser linewidths, presented in section 3.5.1, equation 3.27, except Figure 5.13, which has no theory with which to compare. In the plots, the theory curves go to RFSA frequencies near zero, although these frequencies are impossible to measure experimentally, because the background noise measured by the RFSA at these low frequencies is extremely large, obscuring any measurements. For comparison, the theoretical and experimental peaks heights, and central minimum heights, were each scaled to 1 at a SA frequency of zero. The theory curves for the center width and FWHM were scaled to an approximate best-fit among the experimental data. The scale of the curve for the 50 MHz laser linewidth is relative to the scale for the 100 MHz laser linewidth. The error bars of the experimental data points were determined by the quadratic summation of the error from the Lorentzian curve-fit and the standard deviation of the data values from the four data sets. The extra scatter in the experimental data at RFSA frequencies less than 300 MHz is due to the effect of excessive RFSA background noise at these lower frequencies. Also, as mentioned, the experimental values are derived from four sets of data, a relatively low number that reduces statistical accuracy. As much as a 10% variance of the heterodyne

Figure 5.9 Comparison of theory and experiment for heterodyne peak height.



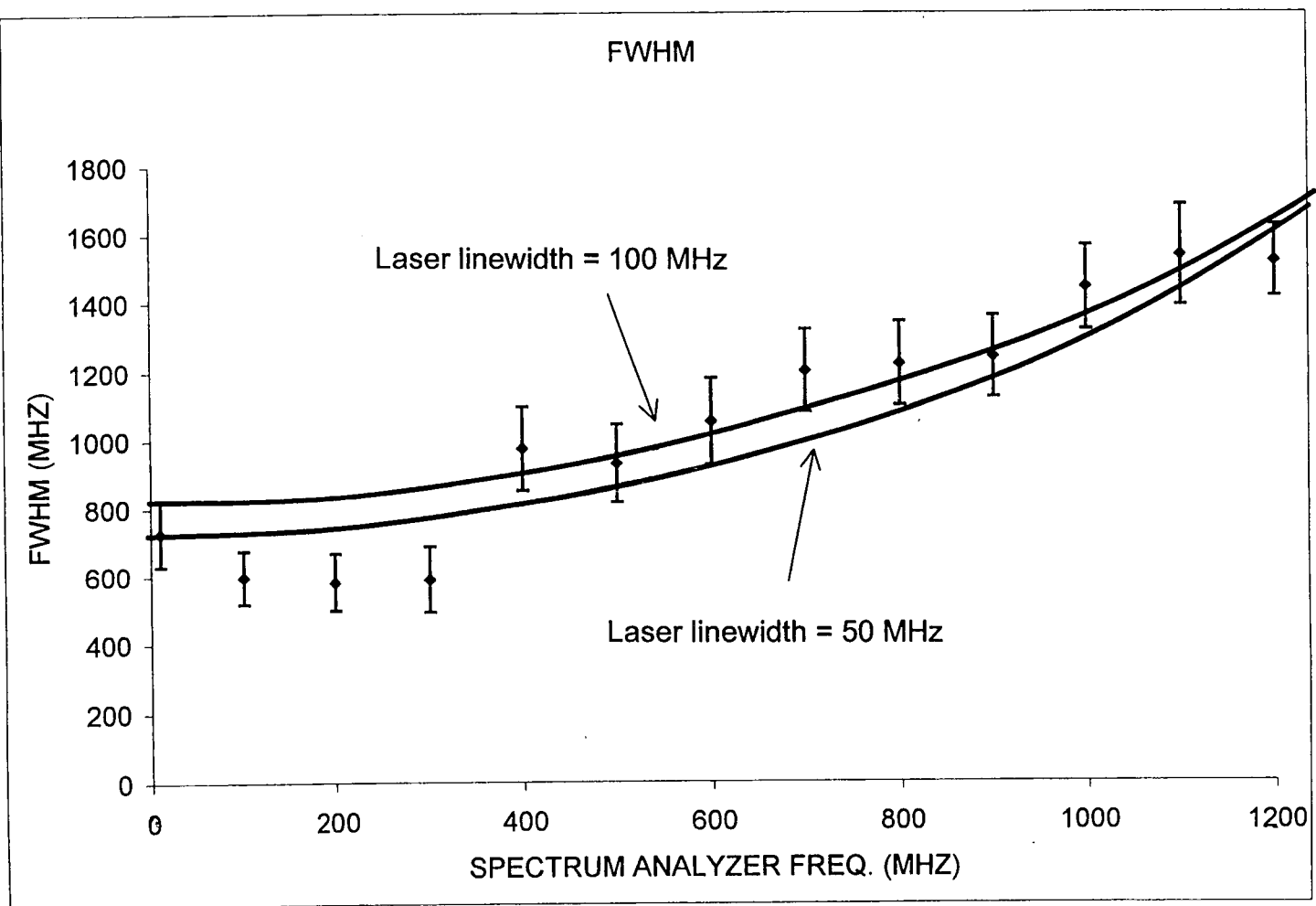


Figure 5.10 Comparison of theory and experiment for heterodyne FWHM.

signal strength can be attributed to this background noise, depending on the RFSA frequency. This scatter made it difficult to find a true normalization factor of the experimental data, a problem exemplified by the data point at the SA frequency of 300 MHz in Figure 5.9. In any case, the utility of the plots in Figure 5.9 through 5.13 is a general comparison of the PDM theory with the experiment. Although the agreement is difficult to accurately assess at the lower SA frequency values because of the data scatter, the general trends agree well for the plots of Figures 5.9 and 5.10. Apparently, the biggest discrepancy between theory and experiment is the center width, shown in Figure 5.11. This may be due to the presence of amplitude noise at the higher SA frequencies, along with the inaccuracy of not including Doppler integration in our theoretical equations, a consideration discussed in section 3.5.1, and shown in Figure 3.9b.

In Figure 5.12, the magnitude of the central minimum is plotted versus SA frequency. The data are scaled to unity, as they are for Figure 5.9. The scatter of the data is due to the graphical method of plotting the data from spectral lineshapes, resulting in a central minimum value that is very sensitive to only one or two data points at line center. As in Figure 5.10, the agreement between theory and experiment digresses slightly as the RFSA frequencies increase. This may be caused by amplitude noise that is more prevalent at higher frequencies, noting figure 2.4. Another reason, already mentioned above, may be the approximate nature of our theory, which ignores Doppler broadening. Figure 3.9a shows this affect.

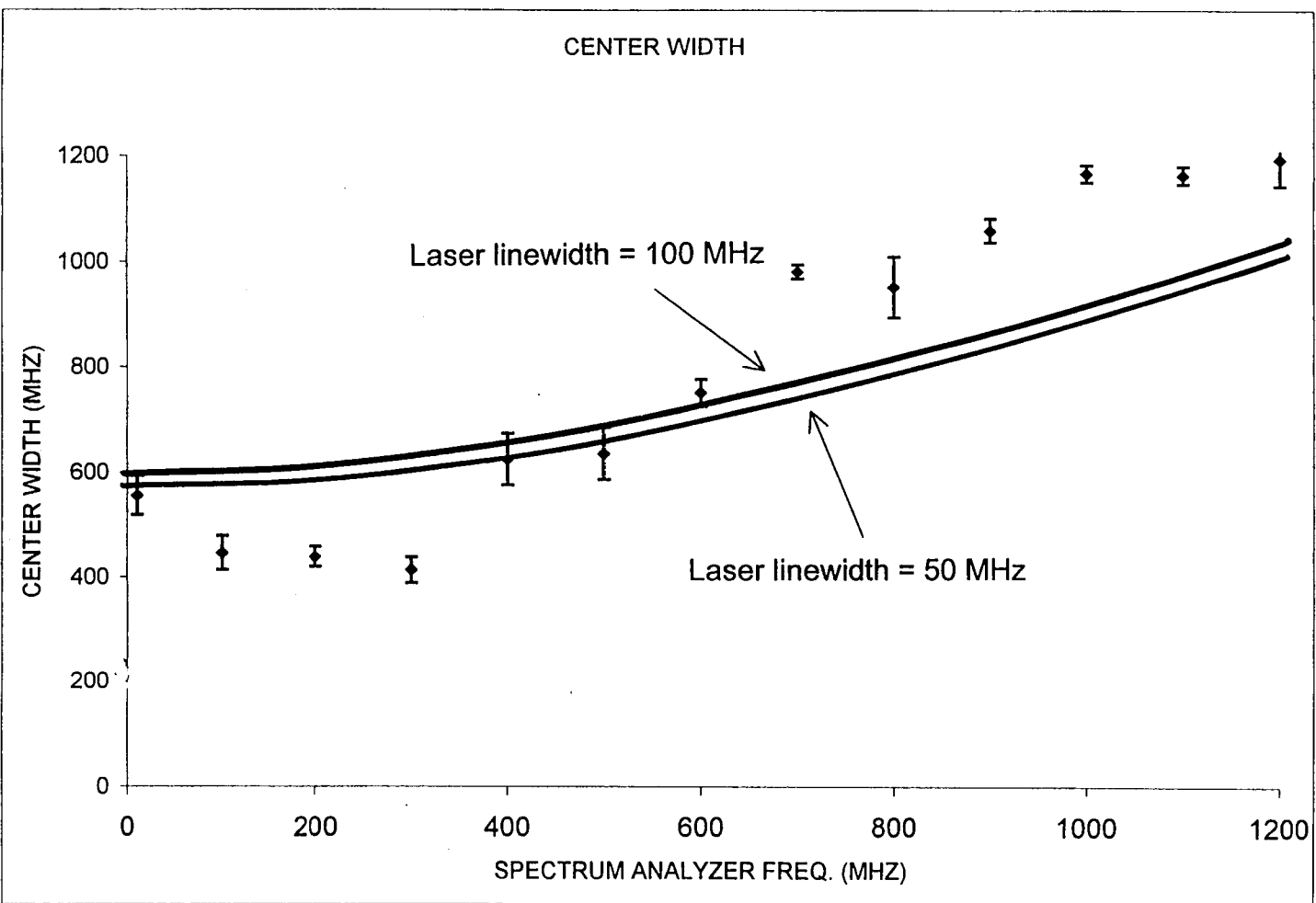


Figure 5.11 Comparison of theory and experiment for heterodyne center width.

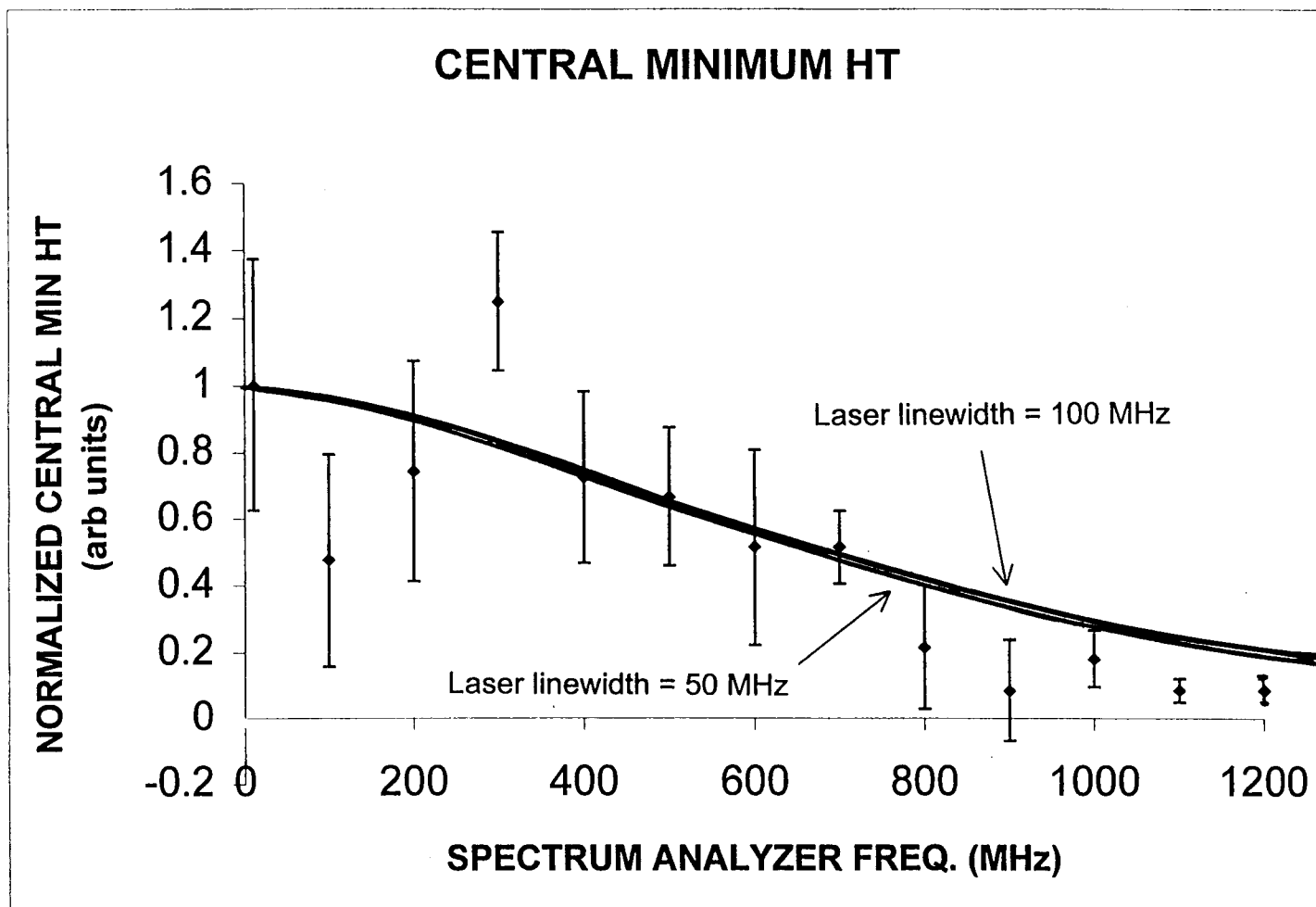


Figure 5.12 Comparison of theory and experiment for heterodyne central minimum height.

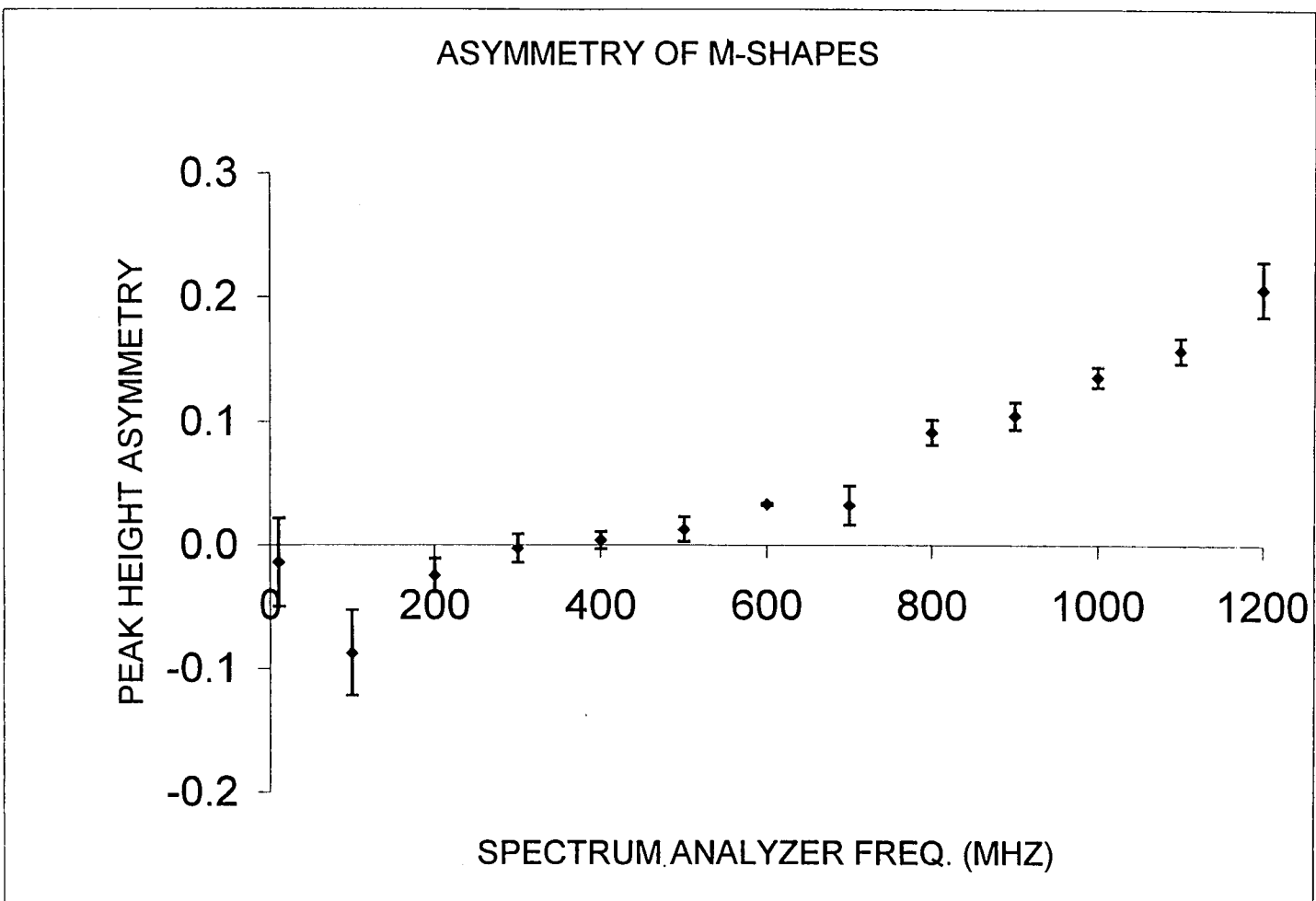


Figure 5.13 Heterodyne lineshape peak height asymmetry.

As the RFSA frequency increases, so does the asymmetry of the measured heterodyne m-shapes, shown in figure 5.12. The PDM, for all values of its parameters, never predicts any asymmetry. As mentioned earlier concerning the LGI spectra, the asymmetry may be caused by correlated amplitude and phase noise. If true then figure 5.12 is strong evidence for the increased presence of amplitude noise at higher frequencies. The lack of amplitude noise effects for the LGI measurements, in section 5.1.1, is due to the fact that only spectra at low SA frequencies could be measured, due to detector range limitations. There is a striking similarity between the asymmetry dependence on frequency, in Figure 5.12, and the intensity noise dependence on frequency in figure 2.4.

In order to ensure our diode laser emission obeys the PDM an experiment was performed to test for the influence of SR on the diode laser emission, which might affect our oxygen heterodyne measurements. The experimental apparatus is shown in Figure 5.14. Heterodyne measurements of the LGI were taken with, and without, the oxygen cell included in the optical path. For this experiment to work properly the oxygen resonance needs to occur at the center of the LGI resonance. We did this by coordinating the frequency of the diode laser scan with the detector position at the output of the LGI. The experiment assumed that the small amount of atmospheric oxygen in the optical path outside the oxygen cell can be neglected in terms of its contribution to SR. If the LGI heterodyne m-shapes were dissimilar for the cases with, and without the oxygen cell, then we would suspect the presence of SR effects. However, no such effects were detected. Unfortunately, this experiment could not be performed above a RFSA

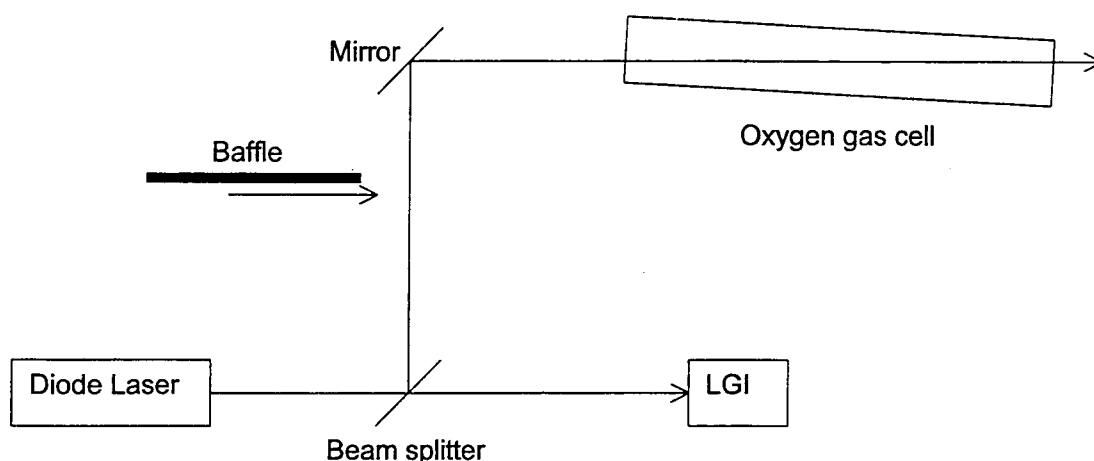


Figure 5.14 Apparatus for testing the presence of selective reflection effects.

frequency above 20 MHz, due to the limitation of the Thor Labs detector frequency range. The Antel detector, with a frequency range up to 3 GHz, can not be used for LGI measurements since not enough light from the LGI output can be focused onto the very small Antel detector, as mentioned in section 4.4. Because most of our oxygen data is above 20 MHz, this experiment which tests for the effects of SR is not conclusive, especially since intensity noise, caused by SR, is not expected to exist in this lower part of the frequency spectrum, as Figure 3.6 shows.

5.3 Oxygen Spectra for the case of a Diode Laser with Intentional Fresnel Feedback

In order to study the effects of mirror-type optical feedback into the diode laser we placed an uncoated thin glass plate 10 cm from the laser. We then monitored the RFSA, set for a full-scan from zero to 2GHz, to measure the amplitude noise of the laser. The diode laser was temperature tuned away from all atmospheric absorption lines.

At maximum reflection of the glass plate the amount of optical feedback should be about 5%. This high feedback creates a very chaotic output of the laser; the amplitude noise spectrum seems to rapidly, and randomly fluctuate. To prevent these conditions of chaotic diode laser behavior the glass plate's reflection is shifted away from the laser cavity direction by a small amount so that, geometrically, the amount of optical feedback is reduced. Using these crude methods does not allow us to know the amount of optical feedback that actually gets into the laser cavity. But by adjusting the mirror and simultaneously observing the amplitude noise spectrum, a fair judgement is to say that an upper limit to the amount of optical feedback into the laser is about one-third the maximum, or 2%. This judgement is based on the amplitude noise level having a linear relation with the amount of optical feedback, which may be very approximate. Figure 5.15 shows the amplitude noise spectrum with this much feedback. The light line is for a laser drive current of 50.7 mA, and the heavy line is for a current 55.5 mA. It can be seen that the amplitude noise peaks shift

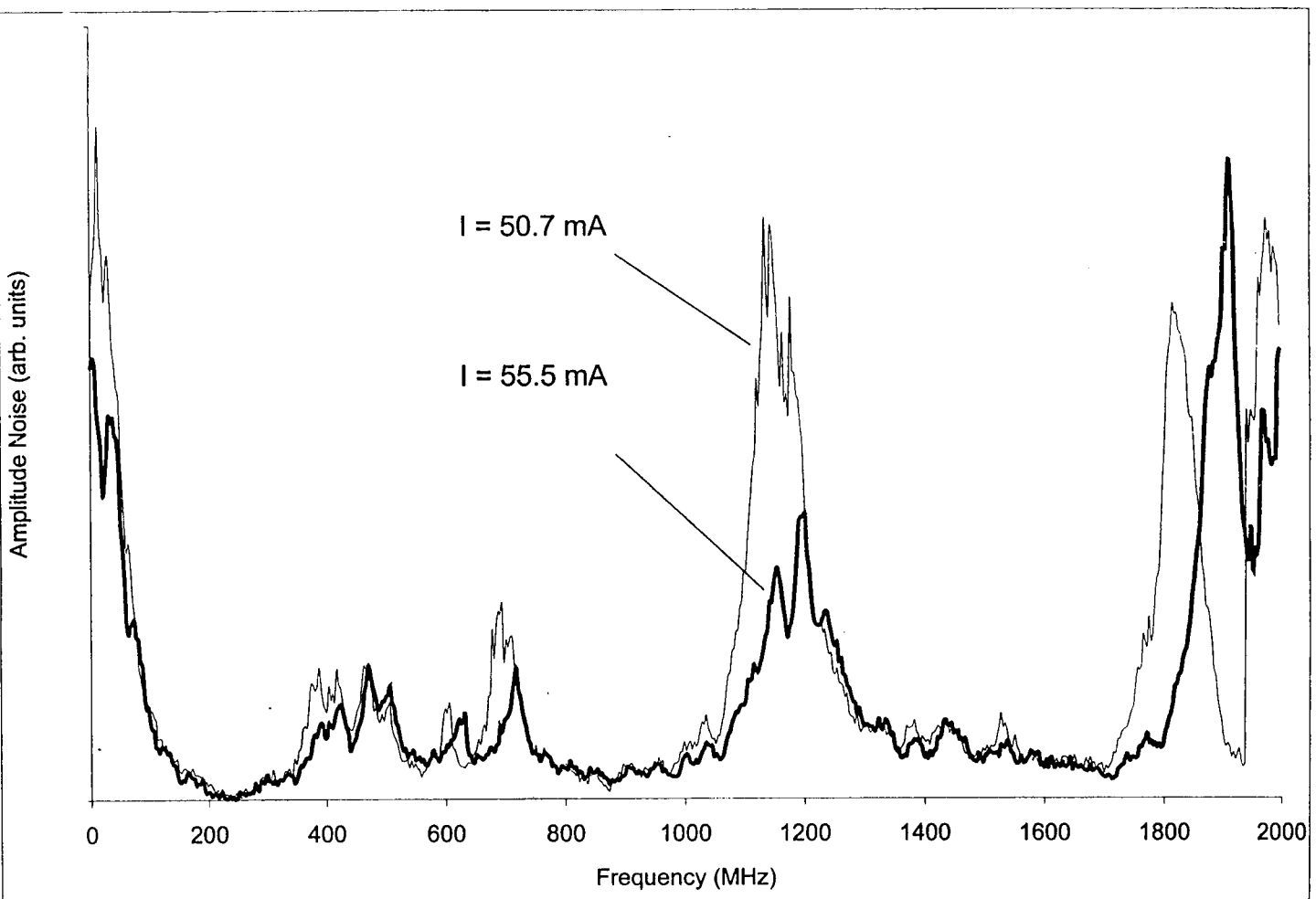


Figure 5.15 Amplitude noise spectra for two drive current values, of a 760 nm diode laser, subjected to optical feedback.

upward in frequency with increasing laser drive current. This is expected from general diode laser theory, as in figure 2.7. Also, the amount of amplitude noise is greater for the lower drive current. This is also expected from diode laser theory, as in figure 2.5.

Figure 5.16 shows a heterodyne spectrum of the RQ(13,14) line with the feedback from the glass plate. The RFSA is set to 100 MHz. In this situation there is so much amplitude noise present that the phase-diffusion model seriously fails. The m-shape is now a single peak. The other peaks are relaxation oscillations that we expect to see with this excessive amount of amplitude noise. When we take the glass plate away no amplitude noise is detected, a result discussed in section 5.1.1. Thus, we have demonstrated that amplitude noise exists as a result of feedback into our diode laser, otherwise the diode laser is free from amplitude noise.

5.4 Spectra of the Diode Laser with Unintentional Fresnel Feedback

An activity in the lab was to observe any effects of cooling the oxygen in the cell. This was done by placing dry ice in a jacket surrounding the cell. The cell is a PVC tube (2 1/2" diameter). During this particular experiment, the inside surfaces of the wedged end-windows of the cell were near perpendicular to the laser beam. At room temperature, the light reflected from this inside surface did not travel back into the diode laser cavity. However, upon cooling, the PVC tube

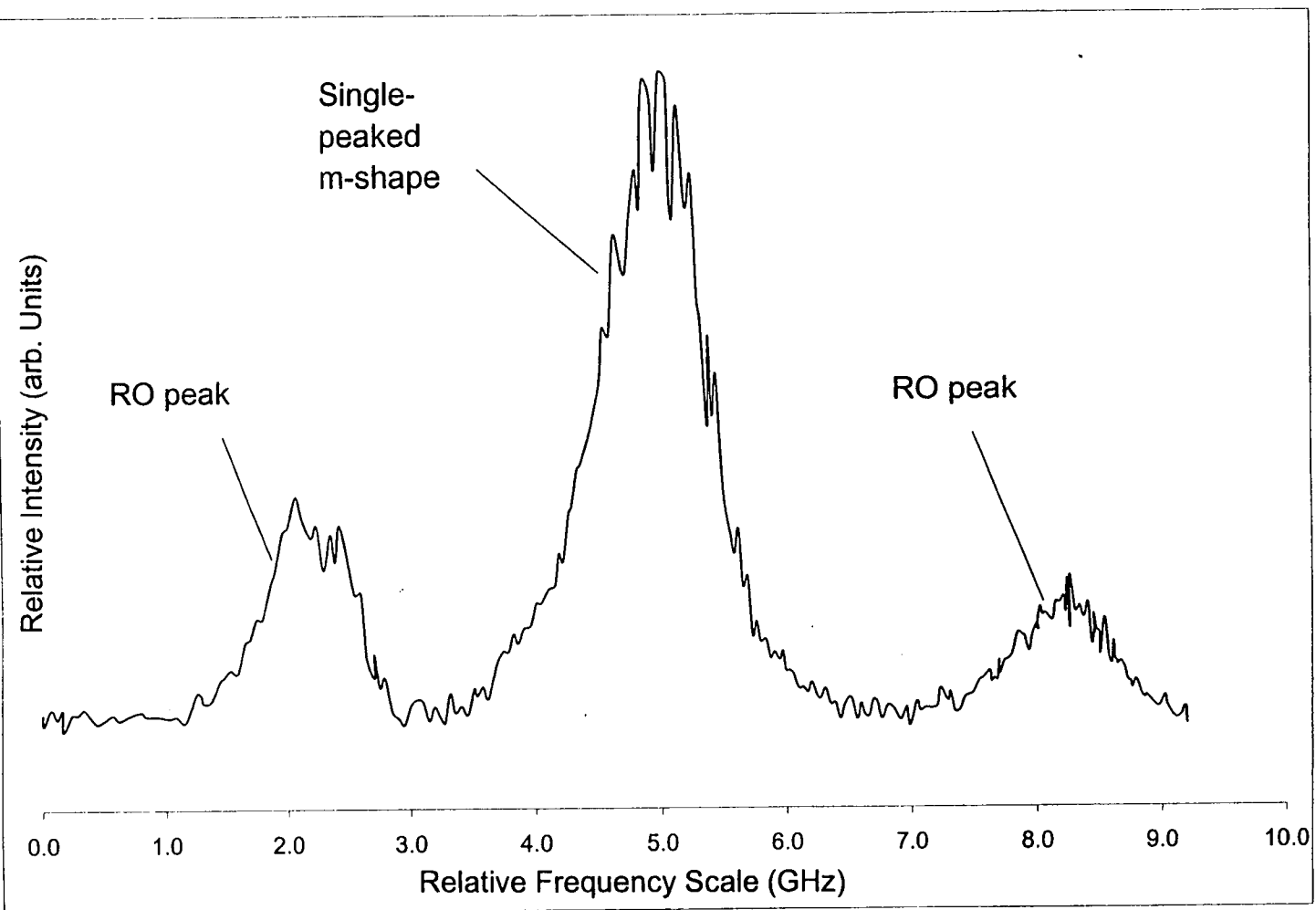


Figure 5.16 Heterodyne lineshape of 760 nm diode laser with optical feedback.

would contort enough to adjust the window surface to reflect light into the laser. This optical feedback was not intended. The results from these experiments are much different than planned; the cooling affects of oxygen were not observed, and the inadvertent reflection into the laser yielded some interesting characteristics of diode laser heterodyning. The slowly contorting oxygen cell resulted in slowly varying degrees of feedback into the laser. Figures 5.17a through 5.17f show heterodyne spectra with increasing amounts of feedback into the diode laser. These are shown for qualitative comparison only, since the amount of optical feedback into the diode laser was not measured. Also, the vertical scale of these spectra was not compensated for the changing diode laser intensity due to the scanning.

Figure 5.17a begins to show relaxation oscillation peaks. The central minimum is not as small as it is for the m-shape shown in Figure 5.7. Figure 5.17b shows the relaxation oscillations being larger with the increased feedback, and the central minimum is larger. Figures 5.17c and 5.17d show this trend continuing with increasing feedback. In Figure 5.17e, it appears that the m-shape central minimum has just become nonexistent, effectively resulting in a single peak. The relaxation oscillations are also larger. This situation may be compared to Figure 5.15 in the case for intentional mirror feedback. In Figure 5.17f there is enough lasing energy in the relaxation oscillations to affect the DC absorption signal, as shown in the figure. Again, the m-shape is single-peaked. Also in this figure, the second order relaxation oscillation peaks are visible. Second order relaxation oscillation amplitudes have been calculated using theory [Vahala, et

al., 1983], and are predicted to be about 1% the amplitude of the first order relaxation oscillations. The laser power of these second order relaxation oscillations are about one-ten thousandth the power of the main laser line. The fact that laser lines of this very small power are visible suggests a high sensitivity for heterodyne spectroscopy measurements.

It is no surprise that amplitude noise increases with increasing amounts of feedback into the diode laser, and we expect the RO's to also increase since RO's *are* amplitude noise. It follows that RO peaks grow with increased feedback.

The phase-diffusion model predicts larger central minima with increased spectral width of the probing laser. Increasing amounts of AM and FM noise are equivalent to increased laser linewidth. So we'd expect these central minima to increase with increasing feedback.

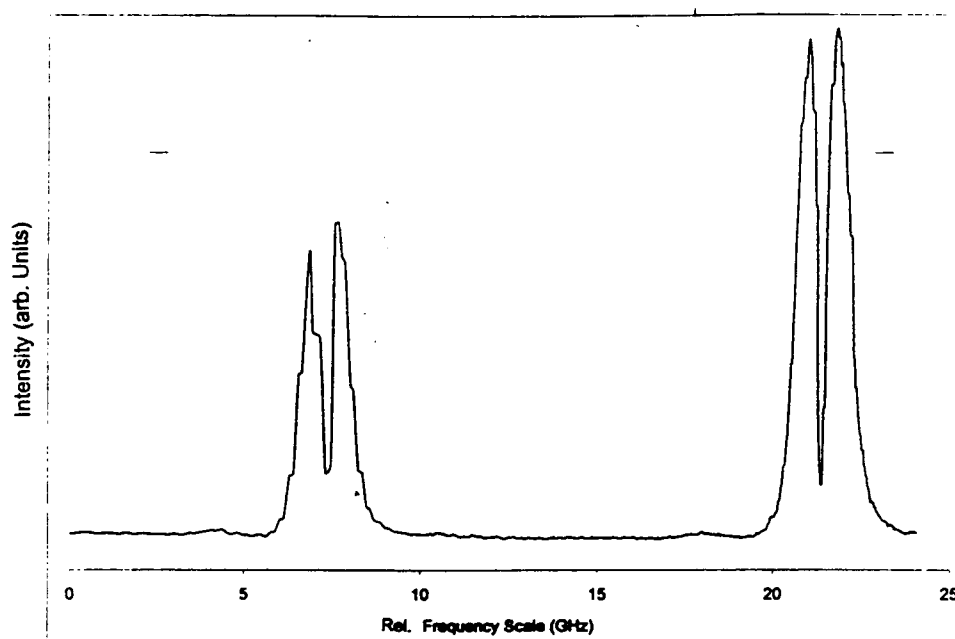


Figure 5.17a Heterodyne lineshapes of oxygen with a relatively small amount of diode laser optical feedback.

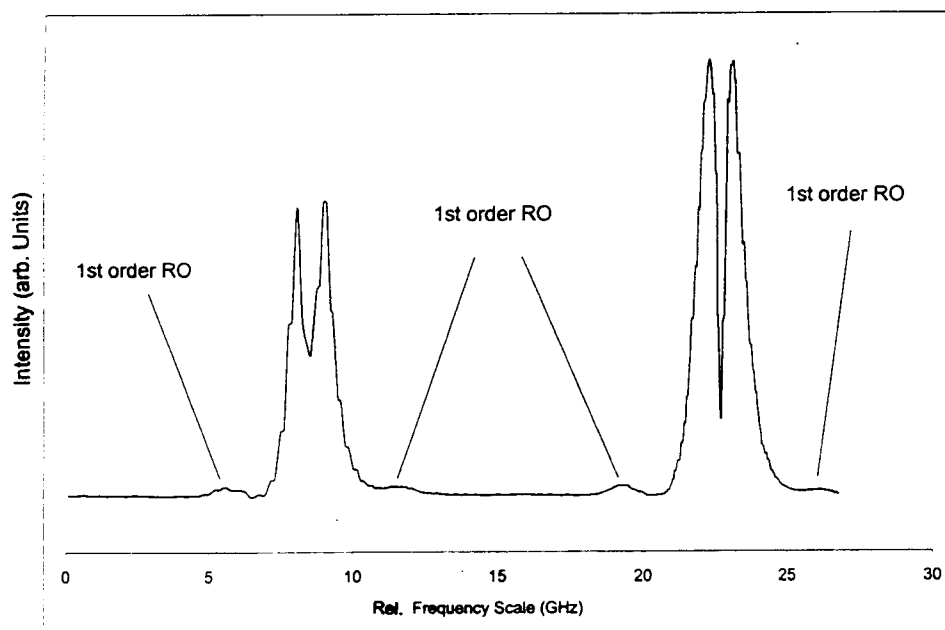


Figure 5.17b Heterodyne lineshapes of oxygen with an increasing amount of diode laser optical feedback.

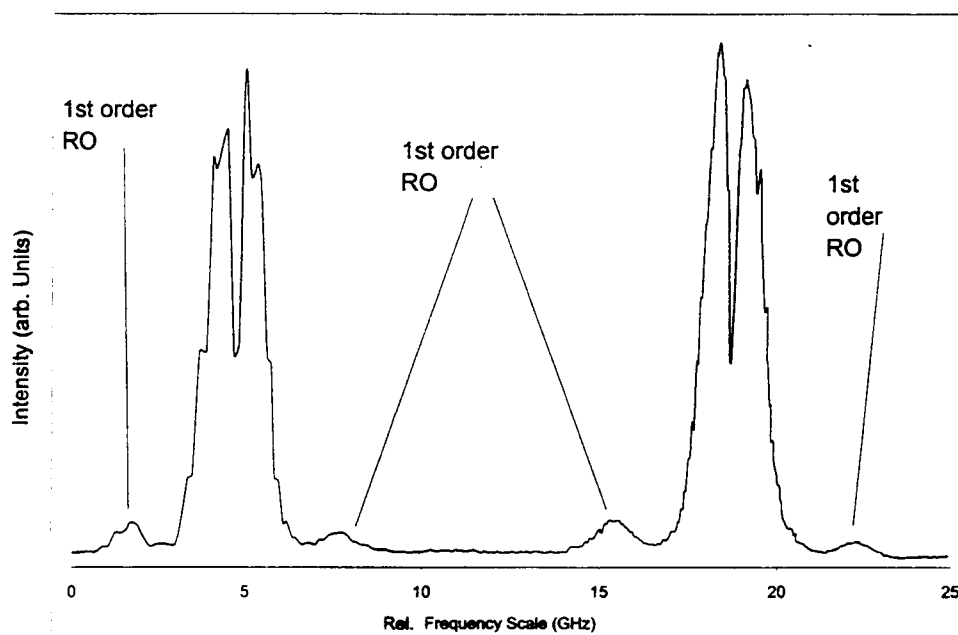


Figure 5.17c Heterodyne lineshapes of oxygen with slightly more diode laser optical feedback than in Figure 5.17b.

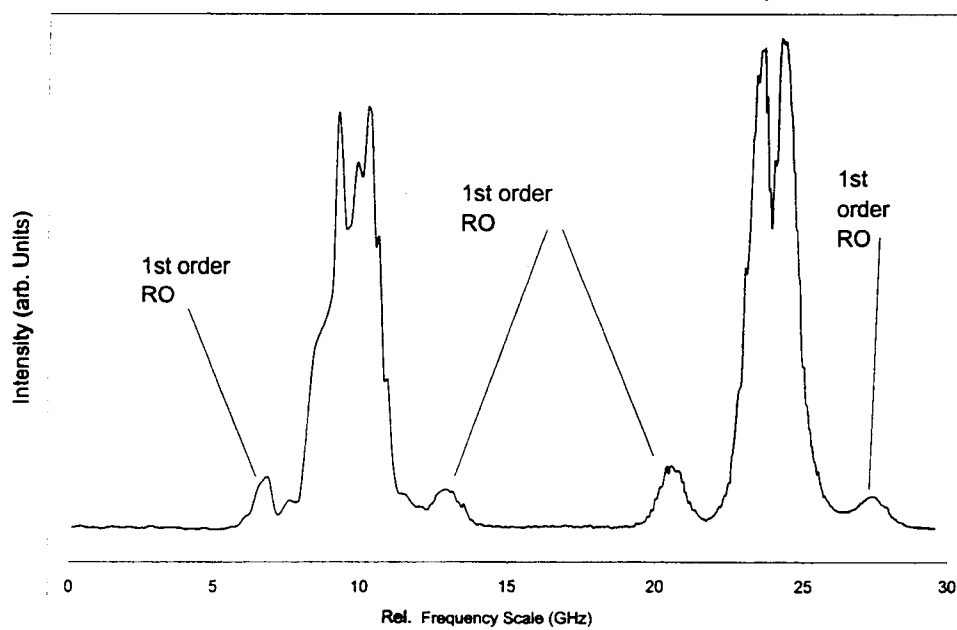


Figure 5.17d Heterodyne lineshapes of oxygen with slightly more diode laser optical feedback than in Figure 5.17c.

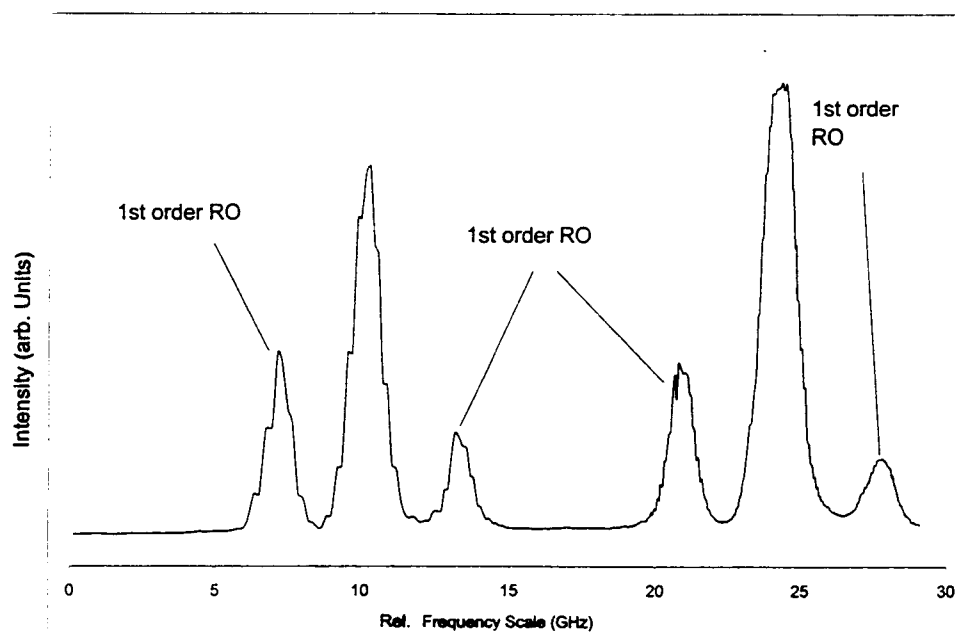


Figure 5.17e Heterodyne lineshapes of oxygen with slightly more diode laser optical feedback than in Figure 5.17d.

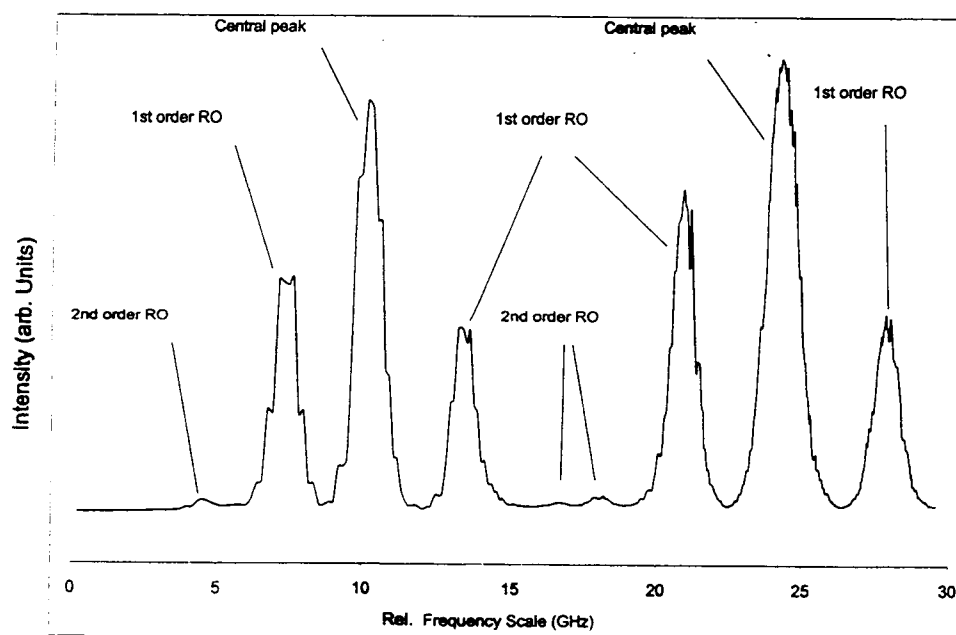


Figure 5.17f Heterodyne lineshapes of oxygen with slightly more diode laser optical feedback than in Figure 5.17e.

CHAPTER 6: SUMMARY AND CONCLUSION

The motivation of our work has been to measure heterodyne lineshapes that are at least qualitatively described by the heterodyne theory of the phase-diffusing laser field. Thus, our starting point was to choose heterodyne signal source, either an interferometer or the atomic/molecular vapor or gas, that fits the criteria of the theory. The oxygen A-band transitions are described as two-level atomic transitions, and their resonance wavelength is close to available diode laser wavelengths. The Lummer-Gehrcke Interferometer can be operated so that it will cause no optical feedback, and it can be operated as a two-beam system, leading to a much easier theoretical description than a confocal Fabry-Perot Interferometer.

It is believed that this thesis presents heterodyne m-shapes that match theoretical predictions better than previous work with interferometers and atomic/molecular vapors or gases. Measured heterodyne spectra of rubidium and oxygen, by other workers, fell short of matching theoretical predictions for an atomic/molecular vapor or gas in a phase-diffusing laser field. In the rubidium case, the measured transitions were known to not exactly obey the theoretical condition that the atomic/molecular system is a two-level, ground/excited state, and this resulted in an asymmetry of their measured m-shapes. In the oxygen case of the other workers, the measured heterodyne spectra of the A-band

transitions were not described by theory, even though these transitions are characterized as two-level atomic transitions. In contrast, our oxygen spectra of the A-band transitions match nicely to theory, implying that our experimental apparatus and technique is an improvement over their earlier work. We conjecture that our most important improvement in experimental technique is the reduction of optical feedback into the diode laser.

Our measured LGI m-shapes, for the NIR diode laser, match qualitative theoretical predictions very well, which indicates that this diode laser's emission obeys the phase-diffusing model. We also measured heterodyne spectra for a visible diode laser, knowing beforehand that this laser does not obey the phase-diffusing model. As expected, the heterodyne spectra for this laser did not come close to theoretical predictions. This contrast between the NIR and visible diode laser heterodyne spectra gives us confidence that we have at least a reasonably good qualitative theoretical description of interferometer heterodyning. A shortcoming in our interferometer work is our lack of a quantitative description of the LGI heterodyne problem. Nevertheless, we have been able to use our qualitative LGI results to help us characterize the diode laser emission, which was important for our subsequent oxygen work.

There are deviations of the data plotted in Figures 5.10 through 5.13 from theoretical predictions that we can expect, considering our theoretical model is only an approximation, because Doppler broadening is neglected. The plots in Figure 3.9 indicate how our non-Doppler theory deviates from the more complete PDM theory as applied to rubidium. This information may be extended to the

case of oxygen for an idea of how close we can expect this approximate theory to describe our experimental results. At the time of this writing, we are in the process of producing theoretical results that include Doppler broadening for the case of oxygen. These results will be presented in the near future.

Another reason for a discrepancy between theory and experiment is an increased presence of amplitude noise in the diode laser emission at higher RFSA frequencies that tend to undermine the accuracy of our theory at this part of the spectrum. In particular, increasing asymmetry of the m-shapes, as described by the data of Figure 5.13, indicates increasing amounts of correlated amplitude and phase noise.

An experiment was performed to test for any effects from selective reflection. Although we found no measurable effect, our experiment is inconclusive because apparatus limitations prevented us from looking for selective reflection in the higher-frequency spectral region where it's effects are most likely to occur.

Testing for selective reflection effects on heterodyne spectra is a topic of future research.

We have presented m-shapes that include relaxation oscillations peaks by introducing optical feedback to the diode laser. As the relaxation oscillation peaks increase, most likely from increased feedback, the central minimum increases, perhaps because the theory predicts an increasing central minimum value as the laser linewidth increases. Since a greater linewidth is concomitant with increased amplitude and phase noise, we may wonder why these m-shapes display no asymmetry. A possible explanation is that the optical feedback mechanism

producing the extra noise does not produce *correlated* amplitude and phase noise, which is a necessary condition for asymmetry. These m-shapes are very interesting, and it is unfortunate that they were measured during an experiment that did not specifically control the optical feedback. For this reason, future research will involve measurements that try to reproduce these m-shapes, while characterizing the optical feedback.

BIBLIOGRAPHY

G. P. Agrawal, N. K. Dutta, "Semiconductor Lasers", 2nd ed., Van Nostrand-Reinhold, New York, 1993.

Anderson, M.H., Jones, R.D., Cooper, J., Smith, S. J., Elliott, D. S., Ritsch, H., and Zoller, P., Phys. Rev. A., **42**, 11 (1990).

Bjorkland, G. C., Levenson, M. D., Lenth, W., Ortiz, C., Appl. Phys. B, **32**, 145 (1983).

Black, H. S., "Modulation Theory" D. Van Nostrand Company, Inc., 1953.

Bohler, C. L., and Marton, B. I., Optics Letters, **19**, 17 (1994).

Brewer, R. G., and Genack, A. Z., Phys. Rev. Letters, **36**, 959 (1976).

Brewer, R. G. and Shoemaker, R. L., Phys. Rev. A., **6**, 2001 (1972).

Born, M., Wolf, E. "Principles of Optics", Pergamon Press, 3rd (revised) edition, 1965.

Camparo, J.C., J. Opt. Soc. Am. B, **15**, 3 (1998).

Cojan, J. L., Ann. Phys. (Paris) **9**, 385 (1954).

Cooper, J., Joint Institute for Laboratory Astrophysics, University of Colorado at Boulder, Boulder, Colorado, 80309

Corney, A. "Atomic and Laser Spectroscopy", Oxford University Press, 1977.

Cuccia, C. L., "Harmonics, Sidebands, and Transients in Communication Engineering", McGraw-Hill, 1952.

De Angelis, M., Gagliardi, G., Gianfrani, L., and Tino, G. M., Phys. Rev. Lett. **76**, 2840 (1996).

Dixit, S. N., and Lambropoulos, P., Phys. Rev. A, **21**, 1289 (1980).

Dube, P., Levenson, M. D., and Hall, J. L., Optics Letters, **22**, 184 (1997).

- Ducloy, M., and Fichet, M., J. Phys. II France **1**, 1429 (1991).
- Elliott, D. S., and Smith, S. J., J. Opt. Soc. Am. B, **5**, No. 9 (1988).
- Fairchild, C.E., Dyson, P. L., McLean, R. J., and Hannaford, P., Bull. Am. Phys. Soc. **38**, 1757 (1993).
- Friedberg, R., Hartmann, S. R., and Manassah, Jamal T, Phys. Rev. A, vol. 42, number 9 (1990).
- Garstang, R. H. "Atomic and Molecular Processes", edited by D. R. Bates, Academic Press, pages 1 – 46 (1962)
- Goldstein, N., and Adler-Holden, S. M., Appl. Optics, **32**, 5849 (1993).
- Guo, J., Cooper, J., and Gallagher, A., Phys. Rev. A, vol. 53, 1130 (1996).
- Guo, J., Cooper, J., Gallagher, A., and Lewenstein, M., Optics Comm., **110**, 732 (1994).
- Haslwanter, Th., Ritsch, H., Cooper, J., and Zoller, J., Phys. Rev. A, **38**, 5652 (1988).
- Hilborn, R. C., and Yuca, C. L., Phys. Rev. Lett. **76**, 2844 (1996).
- Jacobs, S. F., Am. J. Phys., **56**, 3, (1988).
- Kitching, J. K., Boyd, A. Yariv, A., and Shevy, Y., Optics Lett., **19**, 1331 (1994).
- Kroll, M., McClintock, J. A., and Ollinger, O., Appl. Phys. Lett. **51**, 1465 (1987).
- Lenstra, D., Verbeek, B. H., and Den Boef, A. J., IEEE J. Quantum Electron., **QE-21**, 674 (1985).
- Li, Yong-quing, Burkett, W. H., and Xiao, Min, Optics Lett., **21**, 982 (1996).
- Macfarlane, R. M., and Zhu, M. Optics Letters, **22**, 16 (1997).
- McIntyre, D. H., Fairchild, C. E., Cooper J., and Walser, R. Optics Lett. **18**, 1816 (1993).
- McLean, R. J., Hannaford, P., Fairchild, C. E., and Dyson, P. L., Optics Lett. **18**, 1675 1993).
- Nienhuis, G., Schuller, F. and Ducloy, M., Phys Rev. A, **38**, 5197 (1988).

- Pedrotti, F. L., and Pedrotti, L. S., "Introduction to Optics", Prentice Hall, 1993.
- Petermann, K., "Laser Diode Modulation and Noise", Kluwer Academic Publishers, 1988
- Raymer, M. G., Mostowski, J., Carlsten, J. L., Phys. Rev. A, **19**, 2304 (1979).
- Ritsch, H., Zoller, P., and Cooper, J., Phys. Rev. A, **41**, 5, (1990).
- Ritter, K. J., and Wilkerson, T. D., J. Mol. Spectrosc. **121**, 1 (1987).
- Rowe, H. E., "Signals and Noise in Communication Systems, D. Van Nostrand Company, 1965.
- Sargent, M., III, Scully, M. O., and Lamb, W. E., Jr., "Laser Physics", Addison-Wesley Publishing Company, 1974.
- Schuller, F., Nienhuis, G., and Ducloy, M., Phys. Rev. A, **43**, 443 (1991).
- Schuurmans, M. F. H., Contemp. Phys., **21**, 463-482 (1980).
- Sharp Corporation, "Laser Diode User's Manual", 1988
- Silver, J. A., Applied Optics, **31**, 707 (1992).
- Takubo, Y., Muroo, K., Miwa, S., Yamamoto, K., Suzuki, K., and Yamamoto, M., J. Mol. Spectrosc. **178**, 31 (1996).
- Van Exter, M. P., Hamel, W. A., Woerdman, J. P., and Zeijlmans, B. R. P., IEEE J. Quantum Electron, **28**, 1470 (1992).
- Wang, P., Gallagher, A., and Cooper, J., Phys. Rev. A, **56**, 1598 (1997).
- Weiman C. E. and Hollberg, L. Rev. Sci. Instrum. **62**, 1 (1991).
- Woerdman, J. P., and Schuurmans, M. F. H., Opt. Commun. **14**, 248 (1975).
- Wood, R. W., Phil. Mag. **18** (1909) 187.
- Yabuzaki, T., Mitsui, T., and Tanaka, U., Phys. Rev. Lett. **67**, 2453 (1991).
- Yamamoto, Y., "Coherence, Amplification and Quantum Effects in Semiconductor Lasers", John Wiley & Sons, 1991.

APPENDICES

APPENDIX A: LUMMER-GERHRCKE INTERFEROMETER

For the Lummer-Gehrcke interferometer to function, the angle of incidence must be far from normal to the surface of the wedge entrance to the plate. This fact is taken as an advantage for the work of this thesis: The reflected light from this interferometer does not re-enter the laser.

In section A.1 the required angle of incidence, θ_i , for the operation of the LGI is derived. In section A.2, the LGI's free spectral range is determined.

A.1 Angle of Incidence of LGI

For the following derivation, refer to figure A.1.

The objective is to find the angle of incidence as a function of the wedge angle, and the index of refraction for the interferometer. Thus,

$$\theta_i = \theta_i(n, \phi) \quad \text{A.1}$$

Take the surrounding medium to be air, so that the index of refraction for the incident light is taken to be unity. Then

$$\sin \theta_i = n \sin \theta_t \quad \text{A.2}$$

By simple geometry,

$$\theta_t = 90^\circ - \phi - \theta_r \quad \text{A.3}$$

Combining equations (A.2) and (A.3),

$$\sin \theta_i = n \sin (90^\circ - \phi - \theta_r) \quad \text{A.4}$$

The sum of all interior angles of a closed triangle is 180 degrees. So,

$$\theta_r + \beta + 90^\circ - \phi = 180^\circ \quad \text{A.5}$$

By inspection,

$$\beta = \alpha + 90^\circ \quad \text{A.6}$$

Combining equations (A.5) and (A.6);

$$\theta_r = \phi - \alpha \quad \text{A.7}$$

Substitution of equation (A.7) into (A.4) yields

$$\sin \theta_i = n \sin (90^\circ - 2\phi + \alpha) \quad \text{A.8}$$

For the Lummer-Gehrcke interferometer to function properly, α must be close to the critical angle;

$$\alpha \approx \sin^{-1} (1/n) \quad \text{A.9}$$

Making this substitution into equation (A.8), and simplifying;

$$\theta_i = \sin^{-1}[n \cos(2\phi - \sin^{-1} (1/n))] \quad \text{A.10}$$

Equation (A.10) gives the correct angle of incidence to operate the Lummer-Gehrcke interferometer. For quartz ($n=1.5$), ϕ can never exceed 45 degrees, otherwise the argument of the arcsine will be greater than one.

As an example, the angle of incidence of a quartz interferometer is about 18 degrees, for a wedge angle of 60 degrees.

A.2 LGI Free Spectral Range

To derive the free spectral range for the Lummer-Gehrcke interferometer refer to figure A.1.

In order to determine the path difference between two consecutive exodus beams, consider the exodus angle to be 90 degrees. It will actually be only slightly less than this, so this is a fair approximation. For a thickness, t , the path difference, Δl is

$$\Delta l = \frac{2nt}{\cos \alpha} - 2t \cdot \tan \alpha = \frac{2t(n - \sin \alpha)}{\cos \alpha} \quad \text{A.11}$$

Therefore the free spectral range is

$$\text{FSR} = \frac{c \cdot \cos \alpha}{2t(n - \sin \alpha)} \quad \text{A.12}$$

where c is the speed of light in vacuum.

Figure A.2 is a plot of the free spectral range as a function of thickness for a quartz LGI, assuming that for a quartz-to-air interface, α is 41.8 degrees. It is clear that thin plates have large values of the free spectral range. The inherent problem, in this case, is that the stiffness of the plate is sacrificed for a thickness less than a centimeter. The flatness of these plates is extremely critical. For high finesse longer plates are best. The required combination of long and thin plates invites the difficulty of flatness over the length of the plate.

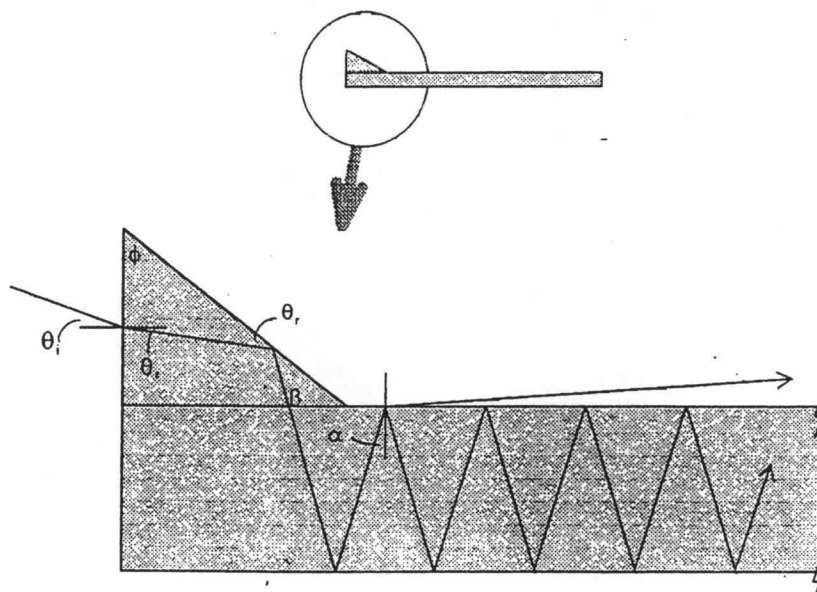


Figure A.1 LGI angles

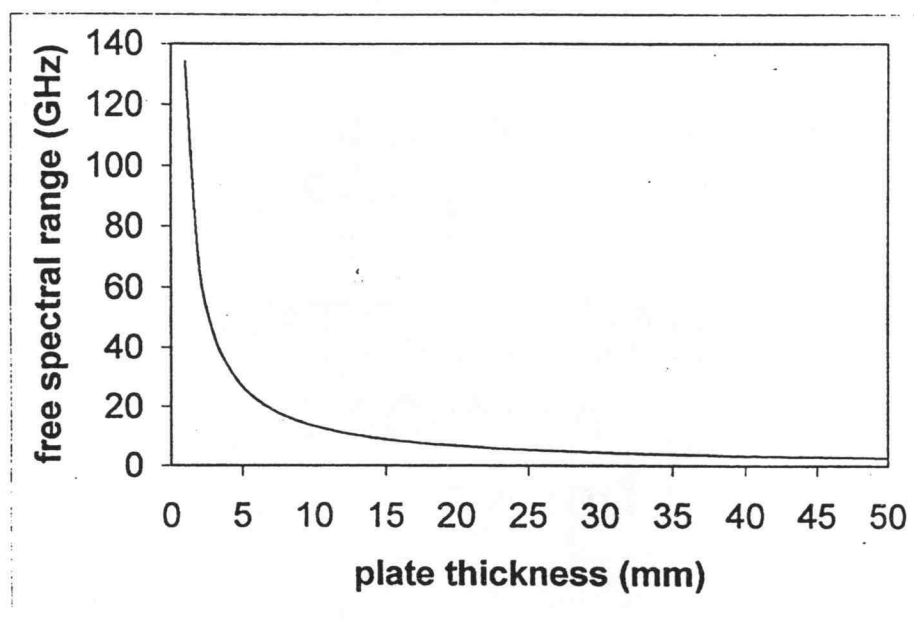


Figure A.2 LGI free-spectral range versus plate thickness

APPENDIX B: LGI n-BEAM CASE

The following is a derivation of a general expression for the case of n exiting beams of the LGI. Refer to section 3.1 for a similar approach for the two-beam case, and for the notation used here.

Express the LGI's emergent field as (with $N+1$ exiting beams)

$$E(t) = A(t) \cos[\omega(t) + \varphi(t)] + A'(t) \cos[\omega(t-\tau) + \varphi(t-\tau)] + \\ + A''(t) \cos[\omega(t-2\tau) + \varphi(t-2\tau)] + \dots + A^N(t) \cos[\omega(t-N\tau) + \varphi(t-N\tau)] \quad (1)$$

For ease of writing, make the following definitions:

$$\begin{aligned} t' &\equiv t - \tau \\ t'' &\equiv t - 2\tau \\ &\vdots \\ t^N &\equiv t - N\tau \end{aligned} \quad (2)$$

So

$$E(t) = A(t) \cos[\omega(t) + \varphi(t)] + A'(t) \cos[\omega(t') + \varphi(t')] + \\ + A''(t) \cos[\omega(t'') + \varphi(t'')] + \dots + A^N(t) \cos[\omega(t^N) + \varphi(t^N)]$$

$$\begin{aligned} \text{Again, for convenience, define: } \alpha &\equiv \omega(t) + \varphi(t) \\ \alpha' &\equiv \omega(t') + \varphi(t') \\ &\vdots \\ \alpha^N &\equiv \omega(t^N) + \varphi(t^N) \end{aligned} \quad \left. \begin{array}{l} \nwarrow (3) \\ \leftarrow (4) \end{array} \right\}$$

So

$$E(t) = A(t) \cos \alpha + A'(t) \cos \alpha' + A''(t) \cos \alpha'' + \dots + A^N(t) \cos \alpha^N \quad (5)$$

The time dependence of the amplitude coefficients will be understood :

$$E(t) = A \cos \alpha + A' \cos \alpha' + A'' \cos \alpha'' + \dots + A^N \cos \alpha^N \quad (6)$$

The photodetector squares and time-averages the field.

$$I(t) = \epsilon_0 c \langle E(t) \rangle^2 = \epsilon_0 c E^*(t) E(t) \quad (7)$$

Squaring eqn (6) and letting the A-coefficients absorb the $\epsilon_0 c$ factor :

$$\begin{aligned} I(t) = & |A|^2 \cos^2 \alpha + |A'|^2 \cos^2 \alpha' + |A''|^2 \cos^2 \alpha'' + \dots + |A^N|^2 \cos^2 \alpha^N + \\ & + A^* A' \cos \alpha \cos \alpha' + A^* A'' \cos \alpha \cos \alpha'' + A^* A''' \cos \alpha \cos \alpha''' + \dots + A^* A^N \cos \alpha \cos \alpha^N + \\ & + A A^* \cos \alpha \cos \alpha' + A A''^* \cos \alpha \cos \alpha'' + A A'''^* \cos \alpha \cos \alpha''' + \dots + A A^N^* \cos \alpha \cos \alpha^N + \\ & + A' A'' \cos \alpha' \cos \alpha'' + A' A''' \cos \alpha' \cos \alpha''' + A' A^N \cos \alpha' \cos \alpha^N + \dots + A' A^N^* \cos \alpha' \cos \alpha^N + \\ & + A' A''^* \cos \alpha' \cos \alpha'' + A' A'''^* \cos \alpha' \cos \alpha''' + A' A^N^* \cos \alpha' \cos \alpha^N + \dots + A' A^N^* \cos \alpha' \cos \alpha^N + \\ & + A'' A''' \cos \alpha'' \cos \alpha''' + A'' A^N \cos \alpha'' \cos \alpha^N + \dots + A'' A^N^* \cos \alpha'' \cos \alpha^N + \\ & + A'' A'''^* \cos \alpha'' \cos \alpha''' + A'' A^N^* \cos \alpha'' \cos \alpha^N + \dots \\ & + A'' A^N^* \cos \alpha'' \cos \alpha^N + \dots + A^{N-1} A^N \cos \alpha^{N-1} \cos \alpha^N + \dots \\ & + A^{N-1} A^N^* \cos \alpha^{N-1} \cos \alpha^N \end{aligned} \quad (8)$$

For the coefficients A^n assumed to be real, equation (8) becomes

$$\begin{aligned}
 I(t) = & A^2 \cos^2 \alpha + A'^2 \cos^2 \alpha' + A''^2 \cos^2 \alpha'' + \dots + A^N \cos^2 \alpha^N + \\
 & + 2AA' \cos \alpha \cos \alpha' + 2AA'' \cos \alpha \cos \alpha'' + 2AA''' \cos \alpha \cos \alpha''' + \dots \\
 & + 2AA^N \cos \alpha \cos \alpha^N + 2A'A'' \cos \alpha' \cos \alpha'' + 2A'A''' \cos \alpha' \cos \alpha''' + \dots \\
 & + 2A'A^N \cos \alpha' \cos \alpha^N + 2A''A''' \cos \alpha'' \cos \alpha''' + 2A''A^{N-1} \cos \alpha'' \cos \alpha^{N-1} + \dots \\
 & + 2A'A^N \cos \alpha' \cos \alpha^N + \dots + 2A^{N-1}A^N \cos \alpha^{N-1} \cos \alpha^N
 \end{aligned} \quad \leftarrow (9)$$

Write eqn (9) as

$$\begin{aligned}
 I(t) = & \sum_{n=0}^N A^n \cos^2 \alpha^n + 2 \left[\sum_{n=0}^{N-1} AA^{n+1} \cos \alpha \cos \alpha^{n+1} + \right. \\
 & \left. + \sum_{n=0}^{N-2} A'A^{n+2} \cos \alpha' \cos \alpha^{n+2} + \dots + \sum_{n=0}^{N-N} A^{N-1}A^{n+N} \cos \alpha^{N-1} \cos \alpha^{n+N} \right],
 \end{aligned} \quad \leftarrow (10)$$

with $\alpha^n = \alpha$ for $n=0$, and $A^n = A$ for $n=0$.

Working with familiar trig. identities:

$$\begin{aligned}
 I(t) = & \frac{1}{2} \sum_{n=0}^N A^n [1 + \cos 2\alpha^n] + 2 \left\{ \frac{1}{2} \sum_{n=0}^{N-1} AA^{n+1} [\cos(\alpha - \alpha^{n+1}) + \cos(\alpha + \alpha^{n+1})] + \right. \\
 & + \frac{1}{2} \sum_{n=0}^{N-2} A'A^{n+2} [\cos(\alpha' - \alpha^{n+2}) + \cos(\alpha' + \alpha^{n+2})] + \dots + \\
 & \left. + \frac{1}{2} \sum_{n=0}^{N-N} A^{N-1}A^{n+N} [\cos(\alpha^{N-1} - \alpha^{n+N}) + \cos(\alpha^{N-1} + \alpha^{n+N})] \right\}.
 \end{aligned} \quad \leftarrow (11)$$

The photodetector cannot respond to frequencies that are faster than the difference frequencies in eqn (11). So these too-high frequencies terms are averaged by the detector as a DC photocurrent. But the spectrum analyzer is not measuring DC. So these too-high frequency terms become zero as eqn (11) is simplified:

$$I(t) = \frac{1}{2} \sum_{n=0}^N A^{n^2} + \sum_{n=0}^{N-1} A A^{n+1} \cos(\alpha - \alpha^{n+1}) + \sum_{n=0}^{N-2} A' A^{n+2} \cos(\alpha' - \alpha^{n+2}) + \dots$$

$$+ \sum_{n=0}^{N-N} A^{N-1} A^{n+N} \cos(\alpha^{N-1} - \alpha^{n+N}) \quad (12)$$

To help clarify the following simplification process let the first cosine term of eqn. (12) (the second overall term) be named T_1 . The second cosine term is named T_2 , and so on, up to the last term, named T_N .

So

$$T_1 = \sum_{n=0}^{N-1} A A^{n+1} \cos(\alpha - \alpha^{n+1})$$

Now expand T_1 :

$$\begin{aligned}
 T_1 &= AA' \cos(\alpha - \alpha') + AA'' \cos(\alpha - \alpha'') + AA''' \cos(\alpha - \alpha''') + \dots \\
 &\quad + AA^N \cos(\alpha - \alpha^N) \\
 &= AA' \cos[\omega(t) + \varphi(t) - \omega(t') - \varphi(t')] + AA'' \cos[\omega(t) + \varphi(t) - \omega(t'') - \varphi(t'')] + \dots \\
 &\quad + AA^N \cos[\omega(t) + \varphi(t) - \omega(t^N) - \varphi(t^N)] \\
 &= AA' \cos[\omega(t) + \varphi(t) - \omega(t - \tau) - \varphi(t - \tau)] + AA'' \cos[\omega(t) + \varphi(t) - \omega(t - 2\tau) - \varphi(t - 2\tau)] + \dots \\
 &\quad + AA^N \cos[\omega(t) + \varphi(t) - \omega(t - N\tau) - \varphi(t - N\tau)] \\
 &\quad \quad \quad \nwarrow (13) \\
 &= AA' \cos[\omega\tau + \Delta\varphi] + AA'' \cos[2\omega\tau + 2\Delta\varphi] + \dots + AA^N \cos[N\omega\tau + N\Delta\varphi]
 \end{aligned}$$

Now expand T_2 :

$$\begin{aligned}
 T_2 &= A'A'' \cos(\alpha' - \alpha'') + A'A''' \cos(\alpha' - \alpha''') + \dots + A'A^N \cos(\alpha' - \alpha^N) \\
 &= A'A'' \cos[\omega(t') + \varphi(t') - \omega(t'') - \varphi(t'')] + A'A''' \cos[\omega(t') + \varphi(t') - \omega(t''') - \varphi(t''')] + \dots \\
 &\quad + A'A^N \cos[\omega(t') + \varphi(t') - \omega(t^N) - \varphi(t^N)] \\
 &= A'A'' \cos[\omega(t - \tau) + \varphi(t - \tau) - \omega(t - 2\tau) - \varphi(t - 2\tau)] + A'A''' \cos[\omega(t - \tau) + \varphi(t - \tau) - \omega(t - 3\tau) - \varphi(t - 3\tau)] + \dots \\
 &\quad + A'A^N \cos[\omega(t - \tau) + \varphi(t - \tau) - \omega(t - N\tau) - \varphi(t - N\tau)] \\
 &= A'A'' \cos[\omega\tau + \Delta\varphi] + A'A''' \cos[2\omega\tau + 2\Delta\varphi] + \dots + A'A^N \cos[(N-1)\omega\tau + (N-1)\Delta\varphi] \\
 &\quad \quad \quad \nwarrow (14)
 \end{aligned}$$

And now expand T_3 :

$$\begin{aligned}
 T_3 &= A'' A''' \cos[\omega(t'') + \varphi(t'') - \omega(t''') - \varphi(t''')] + \\
 &\quad + A'' A'''' \cos[\omega(t'') + \varphi(t'') - \omega(t''') - \varphi(t''')] + \dots \\
 &\quad + A'' A^N \cos[\omega(t'') + \varphi(t'') - \omega(t^N) - \varphi(t^N)] \\
 &= A'' A''' \cos[\omega(t-2\tau) + \varphi(t-2\tau) - \omega(t-3\tau) - \varphi(t-3\tau)] + \\
 &\quad + A'' A'''' \cos[\omega(t-2\tau) + \varphi(t-2\tau) - \omega(t-4\tau) - \varphi(t-4\tau)] + \dots \\
 &\quad + A'' A^N \cos[\omega(t-2\tau) + \varphi(t-2\tau) - \omega(t-N\tau) - \varphi(t-N\tau)] \\
 &= A'' A''' \cos[\omega\tau + \Delta\varphi] + A'' A'''' \cos[2\omega\tau + 2\Delta\varphi] + \dots + A'' A^N \cos[(N-2)\omega\tau + (N-2)\Delta\varphi]
 \end{aligned}$$

← (15)

Finally,

$$\begin{aligned}
 T_N &= A^{N-1} A^N \cos[\omega(t^{N-1}) + \varphi(t^{N-1}) - \omega(t^N) - \varphi(t^N)] \\
 &= A^{N-1} A^N \cos[\omega(t-(N-1)\tau) + \varphi(t-(N-1)\tau) - \omega(t-N\tau) - \varphi(t-N\tau)] \\
 &= A^{N-1} A^N \cos[\omega\tau + \Delta\varphi]
 \end{aligned}$$

← (16)

Define $\gamma \equiv \omega\tau + \Delta\varphi$

So

$$\begin{aligned}
 T_1 &= A A' \cos \gamma + A A'' \cos 2\gamma + \dots + A A^N \cos N\gamma \\
 T_2 &= A' A'' \cos \gamma + A' A''' \cos 2\gamma + \dots + A' A^N \cos (N-1)\gamma \\
 T_3 &= A'' A''' \cos \gamma + A'' A'''' \cos 2\gamma + \dots + A'' A^N \cos (N-2)\gamma \\
 &\quad \vdots \\
 T_N &= A^{N-1} A^N \cos \gamma
 \end{aligned}$$

(17)

Adding all terms from eqn. (12) we get

$$\begin{aligned}
 I(t) &= \frac{1}{2} \sum_{n=0}^N A^n + T_1 + T_2 + T_3 + \dots + T_N \\
 &= A_0 + (AA' + A'A'' + A''A''' + \dots + A^{N-1}A^N) \cos \gamma + \\
 &\quad + (AA'' + A'A''' + A''A'''' + \dots + A^{N-2}A^N) \cos 2\gamma + \dots + AA^N \cos N\gamma, \\
 \text{where } A_0 &\equiv \frac{1}{2} \sum_{n=0}^N A^n \quad \quad \quad (18)
 \end{aligned}$$

Again, For ease of wr.ing, define

$$\begin{aligned}
 A_1 &\equiv AA' + A'A'' + A''A''' + \dots + A^{N-1}A^N \\
 A_2 &\equiv AA'' + A'A''' + A''A'''' + \dots + A^{N-2}A^N \\
 &\vdots \\
 A_N &\equiv AA^N
 \end{aligned} \quad (19)$$

Then Eqn (18) becomes

$$\begin{aligned}
 I(t) &= A_0 + A_1 \cos \gamma + A_2 \cos 2\gamma + A_3 \cos 3\gamma + \dots + A_N \cos N\gamma \\
 &= A_0 + A_1 \cos(\omega t + \Delta\varphi) + A_2 \cos 2(\omega t + \Delta\varphi) + \\
 &\quad + A_3 \cos 3(\omega t + \Delta\varphi) + \dots + A_N \cos N(\omega t + \Delta\varphi) \quad (20)
 \end{aligned}$$

Using the trig. identity

$$\cos(A+B) = \cos A \cos B - \sin A \sin B$$

Eqn (20) becomes

$$\begin{aligned} I(t) = & A_0 + A_1 [\cos \omega t \cos \Delta \varphi - \sin \omega t \sin \Delta \varphi] + \\ & + A_2 [\cos 2\omega t \cos 2\Delta \varphi - \sin 2\omega t \sin 2\Delta \varphi] + \\ & + A_3 [\cos 3\omega t \cos 3\Delta \varphi - \sin 3\omega t \sin 3\Delta \varphi] + \dots \\ & + A_N [\cos N\omega t \cos N\Delta \varphi - \sin N\omega t \sin N\Delta \varphi] \end{aligned} \quad (21)$$

Expand $\cos \Delta \varphi$ and $\sin \Delta \varphi$: $\cos \Delta \varphi = 1 - \frac{(\Delta \varphi)^2}{2!} + \frac{(\Delta \varphi)^4}{4!} - \dots$

$$\sin \Delta \varphi = \Delta \varphi - \frac{(\Delta \varphi)^3}{3!} + \frac{(\Delta \varphi)^5}{5!} - \dots$$

So eqn. (21) becomes

$$\begin{aligned} I(t) = & A_0 + A_1 \left[\left(1 - \frac{(\Delta \varphi)^2}{2!} + \frac{(\Delta \varphi)^4}{4!} - \dots \right) \cos \omega t - \left(\Delta \varphi - \frac{(\Delta \varphi)^3}{3!} + \frac{(\Delta \varphi)^5}{5!} - \dots \right) \sin \omega t \right] + \\ & + A_2 \left[\left(1 - \frac{(2\Delta \varphi)^2}{2!} + \frac{(2\Delta \varphi)^4}{4!} - \dots \right) \cos 2\omega t - \left(2\Delta \varphi - \frac{(2\Delta \varphi)^3}{3!} + \frac{(2\Delta \varphi)^5}{5!} - \dots \right) \sin 2\omega t \right] + \\ & + \dots + A_N \left[\left(1 - \frac{(N\Delta \varphi)^2}{2!} + \frac{(N\Delta \varphi)^4}{4!} - \dots \right) \cos N\omega t - \left(N\Delta \varphi - \frac{(N\Delta \varphi)^3}{3!} + \frac{(N\Delta \varphi)^5}{5!} - \dots \right) \sin N\omega t \right] \end{aligned}$$

For small $\Delta \varphi$ we can drop all but the first term in the expansion:

$$\begin{aligned} I(t) = & A_0 + A_1 [\cos \omega t - \Delta \varphi \sin \omega t] \\ & + A_2 [\cos 2\omega t - 2\Delta \varphi \sin 2\omega t] + \dots + A_N [\cos N\omega t - N\Delta \varphi \sin N\omega t] \end{aligned}$$

$$I(t) = A_0 + \sum_{n=1}^N A_n (\cos n\omega t - n\Delta\varphi \sin n\omega t)$$

Keeping in mind that the spectrum analyzer effectively sees only positive values,

$$I(t) = A_0 + \sum_{n=1}^N A_n [\cos n\omega t + |n\Delta\varphi \sin n\omega t|]$$

APPENDIX C: COMPUTER PROGRAM

The following text is a description of the extensive computer program used to operate the laboratory equipment when taking measurements. The program is written in *Microsoft QuickBasic*, and will run on any PC that is loaded with that driver/compiler. In addition, the computer must be equipped with a *Data Translation*, model DT2801 input/output board. This board performs standard digital input/output, and digital-to-analog and analog-to-digital conversion. The parameters of A/D and D/A conversion, such as gain, are software enabled.

The first question that is posed when the program is first started is, "Is interface card installed on this computer?". Parts of the program can run on a PC without an interface card, namely the processing of data files. If the computer is not equipped with an interface card and a measurement application is chosen, then the computer will suffer a fatal crash and will need to be rebooted (this is due to the program asking for a queue that cannot be fulfilled without the interface card.).

If the answer to the above question is no then the next question will be "Display RF/DC data plot, or quit?". The chance to terminate the program is available here. Else plotting data files is the objective. After entering the name of the data file (with the drive designation), the question concerning the location of the PC has to do with the graphics parameter (screen resolution).

The data-smoothing routine takes an odd number (the number that is operator chosen) of ordinate data points, takes their average, and places the result at their center abscissa point. Entering unity will result in no data smoothing. Numbers greater than eleven tend to unnecessarily obscure plot characteristics. Five or seven is usually the optimum compromise.

At this point the program will plot the data linearly with the laser drive current using the on-board photo diode data. The assumption here is that the photo diode voltage is directly proportional to the laser drive current. So even though the data is taken and stored nonlinearly with drive current this, plotting routine linearizes it for plotting. However the data file is left unchanged. Different smoothing parameters can be chosen to optimize results. Next, the plot can be printed from the screen only if such a printer driver exists.

If the operator chooses to run the laboratory measurement routine, and an interface card is installed in the computer, then A/D gains and plot-scale factors for each channel must be entered. Channel 0,1, and 2 is the DC photo diode input, diode laser's on-board photo diode, and the RF spectrum analyzer's output, respectively.

There are three principle modes of data measurement: Individual data points, full screen sweep, or laser current modulation. The last mode listed in the program (mode 4) is actually the same as the plot routine described above.

Mode 1, individual data points, is the routine that allows the data input and motion of two photo diodes mounted on a vertically traveling stage operated by a stepper motor. This is used for the Lummer-Gerhcke spectra measurements.

The first choice of mode 1 is whether to use automatic stepper motor control, or control the individual steps of the motor by pressing the keyboard's spacebar. The parameters to enter for automatic stepper motor control are the stepper motor's steps per revolution, and the distance of vertical travel per revolution, which is a characteristic of the traveling-stage micrometer. Next, the initial position of the stage can be set. The final choices to be made are the total vertical travel distance, travel up or down, and the number of times the A/D input lines should be sampled per stage position. While the data collecting routine is running, the DC and RF signals are plotted on the screen as the data is being collected. After the screen is full (640 pixels left to right) the data taking terminates and the option is to record the data, start over, or quit.

If automatic stepper motor control is not the option chosen then a single set of data per position of the stage will be taken per press of the spacebar, while stepping the motor once.

Mode 2 is essentially a screen dump for the RF spectrum analyzer. Mode 3 is the routine used to scan the laser through resonance lines by controlling laser-drive current. This mode is used for all the oxygen spectroscopy.

Running in mode 3, the first thing that has to be done is that the current-sweep endpoints must be chosen. These are chosen by correctly positioning the stepper motor, since the stepper motor turns the current-controlling variable resistor. During this setting procedure, the operator must visually monitor the ammeter in the diode laser drive circuit. The drive current range can be chosen

by changing a specific resistor in the drive circuit. The choice for range also determines the frequency resolution of the scan.

Next, the two parameters sweep rate and current resolution, are the delay between motor steps and the number of motor steps taken between measurements, respectively.

Upon choosing the number of scans in a data run (cycles), data collecting begins. At the end of a scan the data for that scan is averaged with the data of the previous scan. This allows for greater signal-to-noise. Another related choice to determining signal-to-noise is the number of data points collected and averaged per current step.

All data collected can be stored in files on a hard disk and floppy disk. In addition to the spectroscopic data, the drive current parameters of a run are recorded.

Although the data can be plotted using this program (mode 4), the data is usually evaluated and plotted using common applications, such as *Microsoft Excel*.

For additional information concerning the lab software, the comments among the lines of the program can be consulted. The lab software follows:

'The following program allows computer control of external lab parameters, 'gathers spectroscopic data, performs data processing and plotting, and 'simplifies the transfer of data files from the lab computer to other off-site 'computers.

'This program requires the input/output computer board, Data Translation, 'model DT2801. This board performs standard digital input/output, and 'digital-to-analog and analog-to-digital conversion. The parameters of A/D 'and D/A conversion, such as gain, are software enabled.

'This program was written and run on a '286 IBM compatible personal

'computer. It will also run on newer generation PC's, if MicroSoft QuickBasic
'is installed on that computer. A difficulty may occur with purchasing
'MicroSoft QuickBasic, because MicroSoft has abandoned this application for
'VisualBasic. This program will have to be modified significantly for this
'newer application.

'set constant values, and array dimensions;

```
CLS
BASE.ADDRESS = &H2EC
COMMAND.REGISTER = BASE.ADDRESS + 1
STATUS.REGISTER = BASE.ADDRESS + 1
DATA.REGISTER = BASE.ADDRESS
COMMAND.WAIT = &H4
WRITE.WAIT = &H2
READ.WAIT = &H5
CSTOP = &HF
CCLEAR = &H1
CERROR = &H2
EXT.TRIGGER = &H80
CSOUT = &H5
CDIOOUT = &H7
CADIN = &HC
FACTOR# = 4096: RANGE = 10: OFFSET = 0
DIM DATA.VALUE(1200, 3)
DIM SUMNUM(1200, 3)
DIM TEMPV(1200, 3)
DIM DATSUM(1200, 3)
DIM NINTPD(1000)
DIM INTPD(1000)
DIM Y(660)
del = 100: l = 0
```

'Many subroutines of this program will crash the computer (require full
'reboot) if the interface board is not installed. Exception is the plotting
'subroutine, mode 4

```
11 INPUT "IS INTERFACE CARD INSTALLED ON THIS COMPUTER (Y OR
N)"; I$
IF I$ = "N" THEN
12 INPUT "DISPLAY RF/DC DATA PLOT (D) OR QUIT (Q)"; I$
IF I$ = "D" THEN GOTO 9004
IF I$ = "Q" THEN GOTO 11111
```

```

    GOTO 12
  END IF
  IF I$ <> "Y" THEN GOTO 11

```

'CHECK FOR LEGAL STATUS REGISTER;

```

    STATUS = INP(STATUS.REGISTER)
    IF NOT ((STATUS AND &H70) = 0) THEN GOTO 9800

```

'STOP AND CLEAR THE DT2801;

```

    OUT COMMAND.REGISTER, CSTOP
    TEMP = INP(DATA.REGISTER)
    WAIT STATUS.REGISTER, COMMAND.WAIT
    OUT COMMAND.REGISTER, CCLEAR

```

'SET DIGITAL PORT 0 TO BE OUTPUT;

```

    WAIT STATUS.REGISTER, COMMAND.WAIT
    OUT COMMAND.REGISTER, CSOUT

```

```

    WAIT STATUS.REGISTER, WRITE.WAIT, WRITE.WAIT
    OUT DATA.REGISTER, 0

```

GOSUB 2000

```

    PRINT "Choose a mode..."
    PRINT "MODE 1: INDIVIDUAL DATA POINTS"
    PRINT "MODE 2: FULL SCREEN SWEEP (Spectrum Analyzer SCREEN
DUMP)"
    PRINT "MODE 3: LASER CURRENT MODULATION"
    PRINT "MODE 4: DISPLAY PLOT OF RF/DC FILE"
    INPUT "MODE 1,2,3, OR 4"; MODE
    IF MODE = 1 THEN GOTO 90
    IF MODE = 3 THEN GOTO 700
    IF MODE = 4 THEN GOTO 9004

```

'Mode 2: the spectrum analyzer display will be digitized and loaded
 'into the computer. The time delay below must be made compatible with the
 'spectrum analyzer scan rate.

'FULL SCREEN SWEEP (Spectrum Analyzer SCREEN DUMP)...

```

INPUT "ENTER TIME DELAY"; DELAY
FOR I = 1 TO 639
  GOSUB 1000
  FOR TIME.DELAY = 1 TO DELAY
    NEXT TIME.DELAY
  NEXT I

```

'PLOT RESULTS OF MODE 2;

```

CLS : SCREEN 2
FOR X = 1 TO 639
  FOR CHANNEL = 0 TO 1
    PSET (X, 195 - SCALE(CHANNEL) * DATA.VALUE(X, CHANNEL))
  NEXT CHANNEL
NEXT X
GOTO 10000

```

'To be used for the LUMMER-GEHRCKE INTERFEROMETER this mode allows the

'collection of spectroscopic data at a point-by-point

'rate, or a full scan. During the scans the stepper motor, which controls

'the position of photodetectors on a translation stage, must be stepped an

'appropriate number of times for the spectral resolution and range.

'The spacebar is pressed for every data point if done by hand (choice H,

'below) otherwise the scan is automatic.

'MODE 1 ROUTINE;

```

90 INPUT "MOTOR(M) OR HAND(H)"; TYPE$
   IF TYPE$ = "H" OR TYPE$ = "h" THEN GOTO 100
   IF I > 0 THEN GOTO 91
   IF TYPE$ <> "M" AND TYPE$ <> "m" THEN GOTO 90

```

'Collect data automatically - full scans. Enter parameters of stepper
'motor used. Scan up or down. 'z' is vertical travelling distance of
'photodetectors.

```

INPUT "ENTER STEPPER MOTOR'S STEPS PER REVOLUTION";
STEPREV

```

```

INPUT "ENTER DELTA-Z PER REVOLUTION"; ZREV
91 ' values used for the present lab apparatus; STEPREV = 600: ZREV = .5

```



```

INPUT "POSITION MOTOR (Y/N)"; a$ '---set initial spectral condition
IF a$ = "Y" THEN
95  GOSUB 5000
    INPUT "POSITION MOTOR AGAIN (Y/N)"; a$
    IF a$ = "Y" THEN GOTO 95
END IF

INPUT "CHANGE GAIN PARAMETERS (Y/N)"; a$ '---another chance...
IF a$ = "Y" THEN GOSUB 2000
97  INPUT "ENTER DELTA-Z PER MEASUREMENT"; DELZ '---resolution

CLS : PRINT "PREPARE TO TAKE DATA;"
STEPS = STEPREV * DELZ / ZREV
INPUT "ENTER TOTAL Z"; TOTZ '---total spectral range
INPUT "TRAVEL UP(U) OR DOWN(D)"; TRAV$ '---scan up or down in freq.
IF TRAV$ = "U" OR TRAV$ = "u" THEN DIREC = 1
IF TRAV$ = "D" OR TRAV$ = "d" THEN DIREC = 0
INPUT "ENTER NUMBER OF DATA POINTS PER STEP"; NUMDAT '---
S/N value

```

'if the combination of spectral range and resolution is too large to
'fit on a screen, then redo these parameters...

```

LIMIT = INT(TOTZ / DELZ)
IF LIMIT * NUMDAT > 639 THEN
    PRINT : PRINT : PRINT : PRINT
    PRINT "...FATAL SCREEN LIMITATION..."
    PRINT "INCREASE STEP-SIZE AND/OR REDUCE NUMBER OF DATA
POINTS"
    GOTO 97
END IF

```

```

93  I = 0: MOVFLAG = 0: CLS : SCREEN 2
    GOSUB 2500

```

```

FOR N = 0 TO LIMIT
    FOR NN = 1 TO NUMDAT
        I = I + 1
        GOSUB 1000      'READ DATA ON A/D
        IF I = 1 THEN GOSUB 80
        LOCATE 3, 1
        PRINT "DELTA-Z="; INT(I / NUMDAT) * DELZ
        FOR CHANNEL = 0 TO 1
            PSET (I, 195 - SCALE(CHANNEL) * DATA.VALUE(I, CHANNEL))
        NEXT CHANNEL
    NEXT NN
NEXT N

```

```

NEXT NN
GOSUB 1100          'MOVE STEPPER MOTOR
a$ = INKEY$
IF a$ = "q" OR a$ = "Q" THEN GOTO 10000

NEXT N
GOTO 10000

```

'This section measures and records spectral data on a point-by-point basis.
 'The spacebar is pressed for each data point. For each data the stepper
 'motor is moved an appropriate number of steps depending on the chosen
 'resolution.

```

100  CLS : SCREEN 2
      GOSUB 2500
      I = 0: FLAG = 0
110  a$ = INKEY$
      IF a$ = "Q" OR a$ = "q" THEN GOTO 10000
      IF a$ = "G" THEN
          GOSUB 2000
          GOTO 100
      END IF
      IF a$ = "A" OR a$ = "a" THEN GOTO 300 '----scan automatically instead
      IF a$ = "R" OR a$ = "r" THEN GOTO 100 '----reset scan
      IF a$ <> " " THEN GOTO 110

      I = I + 1
60   LOCATE 3, 1
      PRINT "X="; I
      a$ = INKEY$
      IF a$ = "G" THEN
          GOSUB 2000
          GOTO 100
      END IF
      GOSUB 1000
      IF I = 1 THEN GOSUB 80
      X = I
      FOR CHANNEL = 0 TO 1
          PSET (X, 195 - SCALE(CHANNEL) * DATA.VALUE(X, CHANNEL))
      LOCATE 5 + CHANNEL, 1
      PRINT "CHANNEL"; CHANNEL; "=";
      PRINT USING "###.###"; DATA.VALUE(X, CHANNEL)
      NEXT CHANNEL
      IF FLAG = 1 THEN GOTO 400

```

GOTO 110

'This section allows the scan to be automatic, just like mode 'M' above.
'The choices 'F' and 'S', below, make the scan run Faster or Slower. The
'F or S keys may be hit repeatedly to strengthen the affect.

```
300 FLAG = 1: i.temp = I
   FOR I = i.temp TO 639
     FOR time.del = 1 TO del
       NEXT time.del
       B$ = INKEY$
       IF (B$ = "f" OR B$ = "F") AND del > 20 THEN del = del - 20
       IF (B$ = "s" OR B$ = "S") AND del < 300 THEN del = del + 20
       IF B$ = "q" OR B$ = "Q" THEN GOTO 10000
       IF B$ = "r" OR B$ = "R" THEN GOTO 100
     GOTO 60
400 NEXT I
   GOTO 10000 ' <---done. record data?
```

'This subroutine records the RAM data into a permanent file on the hard disk,
'and the floppy disk, if so chosen. The name of the last saved file for
'the present session is repeated for convenience.
'Parameters of the scan are also recorded, such as maximum and minimum
'drive currents of the diode laser.

```
500 IF FIFLAG = 1 THEN ' <---if not then this is a first run.
   PRINT "LAST SAVED FILE IS "; FILENAME$
   END IF
   INPUT "ENTER NEW FILE NAME (.DAT IS AUTOMATICALLY
APPENDED)"; FILENAME$
   FIFLAG = 1
   INPUT "IS DISK IN DRIVE A"; a$
   IF a$ = "Y" THEN
     OPEN "A:" + FILENAME$ + ".DAT" FOR OUTPUT AS #1
   END IF
   OPEN "C:" + FILENAME$ + ".DAT" FOR OUTPUT AS #2
   IF a$ = "Y" THEN
     WRITE #1, DATA.VALUE(3, 1), DATA.VALUE(B / 2, 1), HIGHC, LOWC,
DATA.VALUE(MMIN, 1) ' <---continued line
   END IF
   WRITE #2, DATA.VALUE(3, 1), DATA.VALUE(B / 2, 1), HIGHC, LOWC,
DATA.VALUE(MMIN, 1) ' <---continued line

   FOR K = 1 TO B - 1
```

```

    FOR CHANNEL = 0 TO 1
      DATA.VALUE(K, CHANNEL) = INT(DATA.VALUE(K, CHANNEL) * 10000)
/ 10000
    NEXT CHANNEL
    IF a$ = "Y" THEN
      WRITE #1, DATA.VALUE(K, 0), DATA.VALUE(K, 1), DATA.VALUE(K, 2)
    END IF
    WRITE #2, DATA.VALUE(K, 0), DATA.VALUE(K, 1), DATA.VALUE(K, 2)
    NEXT K
  CLOSE
  RETURN

```

'This is the mode used for GAS SPECTROSCOPY. The diode laser drive current 'is scanned through a range chosen below. The limit of the range is 'determined by the choice of a certain resistor in the drive circuit. There 'is a trade-off between range and spectroscopic resolution. 'The scans may be repeated for improved S/N. 'The drive current is scanned by the use of a potentiometer in the diode 'laser drive circuit, which is adjusted by the use of a stepper motor which 'is interfaced with the computer and controlled by this program.

```

700 'MODE 3;
    GOSUB 7700 'ESTABLISH CURRENT-SWEEP RANGE
701 CLS : SCREEN 2

```

```

'determine signal-to-noise...
    INPUT "ENTER NUMBER OF A/D SAMPLES PER CURRENT VALUE";
AVNUM
    CLS
    GOSUB 2500 ' <---GRAPHICS
    FLAGD = 0
    B = 0
    C = 0
    FLAGB = 0
    FOR CHANNEL = 0 TO 2
      FOR a = 1 TO 940
        SUMNUM(a, CHANNEL) = 0
        DATSUM(a, CHANNEL) = 0
        DATA.VALUE(a, CHANNEL) = 0
      NEXT a
    NEXT CHANNEL
    INPUT "ENTER NUMBER OF CYCLES"; CYCLE ' <---determines S/N

```

```

'MOVE MOTOR TO MINC POSITION

```

```

DIREC = 0
FOR X = CSTEP TO MINC STEP -1
  FOR NNN = 0 TO 2 * RESOL STEP 2
    BITTOTAL = NNN + DIREC
    GOSUB 6000
  NEXT NNN
NEXT X

I = 0
DIREC = 1
703 FOR I = 1 TO 639
  B = B + 1
  a$ = INKEY$
  IF a$ = "Q" THEN GOTO 10000

```

'The following section allows the scan to be halted until the operator
'wishes to continue. During pause, the elapsed time is displayed.
'Press 'T' to pause, and press 'S' to restart.

```

  IF a$ = "T" THEN
    Z = INT(TIMER)
    LOCATE 10, 10
    PRINT "WAITING... PRESS S TO RESTART"
704   a$ = INKEY$
    LOCATE 11, 10
    PRINT "ELAPSED TIME: "; INT(TIMER) - Z; "SECONDS"
    IF a$ = "S" THEN
      LOCATE 10, 10
      PRINT "          "
      GOTO 702
    END IF
    GOTO 704
  END IF

```

```

  IF a$ = "G" THEN
    GOSUB 2000 'INPUT A/D GAIN
    INPUT "RESTART SCREEN (Y OR N)?"; a$
    IF a$ = "N" THEN GOTO 702
    GOTO 701
  END IF
702  LOCATE 3, 1
    PRINT "X="; I; " B="; B
    FOR AVEAD = 1 TO AVNUM

```

```

GOSUB 1000 '---READ VALUES ON A/D INPUT LINES
FOR CHANNEL = 0 TO 2
    SUMNUM(B, CHANNEL) = SUMNUM(B, CHANNEL) + DATA.VALUE(B,
CHANNEL)
NEXT CHANNEL
NEXT AVEAD
FOR CHANNEL = 0 TO 2
    DATA.VALUE(B, CHANNEL) = SUMNUM(B, CHANNEL) / AVNUM
NEXT CHANNEL
CSTEP = CSTEP + DIREC - 1 * (1 - DIREC) 'COUNTS UP OR DOWN
' PRINT DIREC, CSTEP, MAXC, MINC <----debug statement...

```

'The following section places a dot if the current changes from decreasing
'to increasing, and two dots if the current changes the other way...

```

IF (CSTEP > MAXC) AND (DIREC = 1) THEN
    DIREC = 0
    FLAGA = 1
    PSET (I, 195): PSET (I, 194) '---PLACE CURRENT-CHANGE
MARKER
END IF
IF (CSTEP < MINC) AND (DIREC = 0) THEN
    DIREC = 1
    PSET (I, 195) '---PLACE CURRENT-CHANGE MARKER

```

```

IF FLAGA = 1 THEN 'Already been to max current. now manipulate data
GOSUB 708 'find minimum value of this run
IF FLAGB = 1 THEN GOSUB 709
FLAGB = 1
FOR CHANNEL = 0 TO 2
    FOR a = 1 TO 2 * STEPS
        DATSUM(a, CHANNEL) = DATSUM(a, CHANNEL) + DATA.VALUE(a,
CHANNEL)
        IF a = 100 AND CHANNEL = 0 THEN
            LOCATE 10, 30
            PRINT DATSUM(a, CHANNEL), DATA.VALUE(a, CHANNEL)
        END IF
    NEXT a
NEXT CHANNEL
C = C + 1
GOSUB 713
IF C = CYCLE THEN
    BEEP: BEEP: BEEP
    CLS
    FOR CHANNEL = 0 TO 2

```

```

    FOR a = 1 TO 2 * STEPS
      DATSUM(a, CHANNEL) = DATSUM(a, CHANNEL) / CYCLE
      DATA.VALUE(a, CHANNEL) = DATSUM(a, CHANNEL)
      PSET (a, 195 - SCALE(CHANNEL) * DATA.VALUE(a, CHANNEL))

    NEXT a
  NEXT CHANNEL
  GOTO 10000
END IF

B = 0
END IF

END IF
FOR NNN = 0 TO 2 * RESOL STEP 2
  BITTOTAL = NNN + DIREC
  GOSUB 6000
NEXT NNN
IF I = 1 THEN GOSUB 80
FOR CHANNEL = 0 TO 2
  PSET (I, 195 - SCALE(CHANNEL) * DATA.VALUE(B, CHANNEL))
  LOCATE 5 + CHANNEL, 1
  PRINT "CHANNEL"; CHANNEL; "=";
  PRINT USING "##.###"; DATA.VALUE(B, CHANNEL);
  PRINT " VOLTS"
NEXT CHANNEL
FOR TIME = 1 TO DELAY
NEXT TIME
IF DIREC = 1 THEN
  PRINT "CURRENT IS INCREASING"
ELSE
  PRINT "CURRENT IS DECREASING"
END IF
NEXT I
CLS : GOSUB 2500: GOSUB 713
GOTO 703

' GOTO 10000

```

'Some of the following sections are used to find the center of the
'spectroscopic feature, such as the center of an atomic line, like a
'transmission dip. This point may be used to synthetically align the scans
'of the different cycles in order to counter the effects of parameter-drift
'with time, such as drive current range, etc.

```

708  'FINDS MINIMUM VALUE OF RUN
      IF FLAGD <> 1 THEN
        INPUT "IS THIS A BASELINE MEASUREMENT (NO O2)"; a$
        IF a$ = "Y" THEN
          AMIN = 1
          AMAX = 0
        ELSE
          INPUT "ENTER AMIN"; AMIN
          INPUT "ENTER AMAX"; AMAX
        END IF
        FLAGD = 1
      END IF
      FLAGC = 0
      FOR a = AMIN TO AMAX
        ' FOR TIMM = 1 TO 500
        ' NEXT TIMM
        IF FLAGC = 0 THEN 'very first loop through this subroutine
          F = DATA.VALUE(a, 0): LOCATE 1, 1: PRINT "F="; F
        END IF
        IF FLAGC = 1 THEN
          F = DATA.VALUE(MMIN, 0)
        END IF
        IF FLAGC = 2 THEN
          F = DATA.VALUE(MIN, 0)
        END IF
        G = DATA.VALUE(a + 1, 0): LOCATE 2, 2: PRINT "G="; G
        IF G < F THEN
          IF FLAGB = 0 THEN 'very first time through this subroutine
            FLAGC = 1
            MMIN = a + 1
          END IF
          IF FLAGB = 1 THEN
            FLAGC = 2
            MIN = a + 1
          END IF
        END IF
      NEXT a
      RETURN '708

```

709 DELTA = MMIN - MIN '----difference between consecutive cycles

'COPY VARIABLE SO DATA-ARRAY SHIFT DOWNWARD CAN OCCUR
(DELTA>0)...


```

FOR CHANNEL = 0 TO 2
  FOR a = 1 TO 2 * STEPS + DELTA
    TEMPV(a, CHANNEL) = DATA.VALUE(a, CHANNEL)
  NEXT a
NEXT CHANNEL

FOR CHANNEL = 0 TO 2
  FOR a = 1 TO 2 * STEPS + DELTA
    IF (a - DELTA) < 0 THEN
      DATA.VALUE(a, CHANNEL) = 0
      GOTO 710
    END IF
    DATA.VALUE(a, CHANNEL) = TEMPV(a - DELTA, CHANNEL)
710  NEXT a
NEXT CHANNEL
RETURN '709

713  LOCATE 3, 65
PRINT "RUN #"; C + 1; "/"; CYCLE
RETURN '713

```

'The following section runs if any run-time errors occur with the IO board.

```

9800 PRINT "FATAL ERROR - ILLEGAL STATUS REGISTER VALUE"
PRINT "STATUS REGISTER VALUE IS "; HEX$(STATUS); "
HEXIDEIMAL"

```

'At the end of scans the following question is asked...

```

10000 INPUT "record data (y or n)"; R$
IF R$ = "y" OR R$ = "Y" THEN GOSUB 500
IF R$ <> "N" AND R$ <> "Y" THEN GOTO 10000

10010 PRINT "QUIT (Q) OR RESTART IN MODE 1 (1), OR MODE 3 (3)"
INPUT "OR DISPLAY FINAL OUTPUT (D)"; C$
IF C$ = "3" THEN
8989 INPUT "CONTINUE WITH THE SAME CURRENT PARAMETERS (Y OR
N)?"; a$
IF a$ = "Y" THEN GOTO 701
IF a$ = "N" THEN GOTO 700
GOTO 8989
END IF
IF C$ = "q" OR C$ = "Q" THEN GOTO 11111

```

```

IF C$ = "1" THEN GOTO 90
IF C$ = "D" AND R$ = "Y" THEN GOTO 9005
IF C$ = "D" THEN
  PRINT "YOU NEED TO RECORD DATA INTO A FILE ON C:"
  GOTO 10000
END IF
GOTO 10010

```

'The following subroutine deals with the gain parameters for the IO board,
'as well as vertical scaling on the screen.

```

2000 'GET A/D GAIN FOR ALL CHANNELS;
    FOR CHANNEL = 0 TO 2
2001 PRINT "ENTER GAIN (ENTER ZERO FOR DEFAULT VALUES) FOR
CHANNEL"; CHANNEL;
    INPUT GAIN(CHANNEL)
    IF GAIN(CHANNEL) = 0 THEN
      GAIN(0) = 3: GAIN(1) = 3: GAIN(2) = 3
      SCALE(0) = 100: SCALE(1) = 100: SCALE(2) = 100
      GAINA(0) = 8: GAINA(1) = 8: GAINA(2) = 8
      GOTO 2002
    END IF
    GAINA(CHANNEL) = GAIN(CHANNEL)
    IF GAIN(CHANNEL) <> 1 AND GAIN(CHANNEL) <> 2 AND
GAIN(CHANNEL) <> 4 AND GAIN(CHANNEL) <> 8 THEN GOTO 2001

    IF GAIN(CHANNEL) = 1 THEN GAIN(CHANNEL) = 0
    IF GAIN(CHANNEL) = 2 THEN GAIN(CHANNEL) = 1
    IF GAIN(CHANNEL) = 4 THEN GAIN(CHANNEL) = 2
    IF GAIN(CHANNEL) = 8 THEN GAIN(CHANNEL) = 3
    ' GAIN(0) = 3: GAINA(0) = 8      'THIS IS BEST VALUE FOR S/A
    INPUT "ENTER VERTICAL SCALE"; SCALE(CHANNEL) '=100 FOR S/A
    NEXT CHANNEL
2002 RETURN '2000

2500 LINE (0, 25)-(639, 25)
    LINE (0, 27)-(639, 27)
    LOCATE 1, 1: PRINT "CHANNEL GAIN/SCALE==>CH 0, CH 1, CH 2   ";
    PRINT GAINA(0); "/"; SCALE(0); ", ";
    PRINT GAINA(1); "/"; SCALE(1); ", ";
    PRINT GAINA(2); "/"; SCALE(2)
    RETURN '2500

```

1000 'THIS SUBROUTINE PERFORMS THE A/D CONVERSIONS FOR ALL CHANNELS.

'CH. 0 IS DC, CH. 1 IS DL'S PHOTO DIODE, AND CH. 2 IS RF.

```

FOR CHANNEL = 0 TO 2
  WAIT STATUS.REGISTER, COMMAND.WAIT 'WRITE READ A/D
IMMED. COMMAND
  IF CHANNEL = 0 AND I = 1 AND MODE = 2 THEN
    OUT COMMAND.REGISTER, CADIN + EXT.TRIGGER
  ELSE
    OUT COMMAND.REGISTER, CADIN
  END IF
  WAIT STATUS.REGISTER, WRITE.WAIT, WRITE.WAIT 'WRITE A/D
GAIN BYTE
  OUT DATA.REGISTER, GAIN(CHANNEL)
  WAIT STATUS.REGISTER, WRITE.WAIT, WRITE.WAIT 'WRITE A/D
CHAN. BYTE
  OUT DATA.REGISTER, CHANNEL

```

'READ TWO BYTES OF A/D DATA FROM THE DATA OUT REGISTER AND
COMBINE
'THE TWO BYTES INTO ONE WORD

```

IF CHANNEL = 0 AND I = 1 AND MODE = 2 THEN
  PRINT "WAITING FOR TRIGGER..."
  WAIT STATUS.REGISTER, READ.WAIT
  PRINT : PRINT :
  PRINT "TRIGGER RECEIVED. COLLECTING DATA..."
ELSE
  WAIT STATUS.REGISTER, READ.WAIT
END IF
LOW = INP(DATA.REGISTER)
WAIT STATUS.REGISTER, READ.WAIT
HIGH = INP(DATA.REGISTER)
DUMMY = HIGH * 256 + LOW
' IF MODE = 3 THEN I = B
DATA.VALUE(B, CHANNEL) = RANGE * DUMMY / FACTOR# /
GAINA(CHANNEL)
LOCATE 14, 10
' PRINT "THIS DATA.VALUE IS "; DATA.VALUE(B, CHANNEL); "MODE=";
MODE
NEXT CHANNEL
RETURN '1000

```

80 'The following section assists in the determination of which trace

'is RF and DC.

```

LOCATE 3, 25
IF SCALE(0) * DATA.VALUE(1, 0) > SCALE(1) * DATA.VALUE(1, 2) THEN
  PRINT "DC > RF AT START"
ELSE
  PRINT "RF > DC AT START"
END IF
RETURN '80

```

1100 'MOVE STEPPER MOTOR A CERTAIN NUMBER OF STEPS IN THE
CORRECT DIRECTION

```

FOR NNN = 0 TO 2 * STEPS
  R = NNN / 2
  BITTOTAL = (R - INT(R)) * 4 + DIREC
  LOCATE 2, 1
  PRINT "STEPS="; INT(R)
  GOSUB 6000
NEXT NNN
RETURN '1100

```

'This subroutine deals with stepper motor direction of rotation and
'other motor drive considerations...

```

5000  CLS
      INPUT "DIRECTION (U/D)"; a$
      IF a$ = "U" THEN DIREC = 1
      IF a$ = "D" THEN DIREC = 0
      INPUT "ENTER DISTANCE IN MILLIMETERS"; DIST
      STEPS = STEPREV * DIST / ZREV
      IF DIST < 1 THEN
        LOCATE 1, 1
        PRINT "HIT SPACEBAR FOR EACH MOTOR STEP"
        PRINT "TYPE C TO CHANGE DIRECTION"
        PRINT "TYPE D IF DONE"
        PRINT "TYPE Q TO QUIT PROGRAM"
5025  a$ = INKEY$
      IF a$ = "C" THEN DIREC = 1 - DIREC
      IF a$ = "D" THEN GOTO 5050
      IF a$ = "Q" THEN GOTO 10010
      IF a$ = " " THEN
        FOR NNN = 0 TO 2 STEP 2

```

```

        BITTOTAL = NNN + DIREC
        GOSUB 6000
    NEXT NNN
END IF
GOTO 5025
END IF
GOSUB 1100
5050 RETURN '5000

```

'This subroutine deals with establishing the diode laser drive current range.
 'The operator follows the instructions while observing an ammeter that is a
 'part of the drive circuit.

```

7700 PRINT "STABILIZE TEMPERATURE. NEXT, CENTER
POTENTIOMETER."
    PRINT "STRIKE ANY KEY WHEN READY..."
7701 a$ = INKEY$
    IF a$ = "" GOTO 7701
    CSTEP = 300 '----DEFINE CENTER POSITION AS 300
    PRINT "ADJUST MASTER CURRENT CONTROL(the rheostat)."
77 PRINT "NEXT, USING THIS PC, ADJUST CURRENT TO DESIRED
MAXIMUM."
    PRINT "USE R (RAISE), L (LOWER), AND D (DONE) KEYS."
    FLAG = 10
    GOSUB 7000
    INPUT "ENTER THIS MAXIMUM CURRENT VALUE"; HIGHC
    PRINT "FINALLY, ADJUST CURRENT TO DESIRED MINIMUM."
    FLAG = 20
    GOSUB 7000
    INPUT "ENTER THIS MINIMUM CURRENT VALUE"; LOWC
    STEPS = MAXC - MINC
79 PRINT "CHOOSE MODE:"
    PRINT "MODE 1; SWEEP CURRENT UP AND DOWN" 'start scanning
    PRINT "MODE 2; ADJUST CURRENT" '----redo current range if needed
    INPUT "MODE"; MODE2
    IF MODE2 = 2 THEN
        FLAG = 30
        GOTO 77
    END IF
    IF MODE2 = 1 GOTO 78
    GOTO 79
78 INPUT "ENTER SWEEP RATE (1-10)"; RATE '----anything below 10
gives
'
                                a time delay
    DELAY = (10 - RATE) * 100

```

```
INPUT "ENTER CURRENT RESOLUTION (1-10)"; RESOL '<---(10-number)
of
'
' steps per
' measurement
```

```
RESOL = (11 - RESOL) * 2 - 1
RETURN '7700
```

```

7000  a$ = INKEY$
      IF a$ = "R" THEN
          CSTEP = CSTEP + 1
          DIREC = 1
          GOTO 7010
      END IF
      IF a$ = "L" THEN
          CSTEP = CSTEP - 1
          DIREC = 0
          GOTO 7010
      END IF
      IF a$ = "D" THEN GOTO 7030
      GOTO 7000

```

```

7010   FOR NNN = 0 TO 2 STEP 2
        BITTOTAL = NNN + DIREC
        GOSUB 6000
    NEXT NNN
    GOTO 7000

7030   IF FLAG = 10 THEN MAXC = CSTEP
        IF FLAG = 20 THEN MINC = CSTEP
        RETURN '7000

```

```

9004 'THIS SUBROUTINE PLOTS THE MODIFIED DATA. ALSO, LINEARIZES
CURRENT AXIS.

```

'SUBROUTINE STARTS HERE IF DATA IS FROM PREVIOUS MEASUREMENT

```

      (DATA FROM DISK). BUT IF DATA WAS JUST GATHERED THEN
SUBROUTINE

```

'ACTION STARTS AT LINE NUMBER 9005.

```
CLS
LOCATE 1, 55
PRINT ".DAT"
LOCATE 1, 1
INPUT "ENTER FILE NAME INCLUDING DRIVE DESIGNATION";
FILENAME$
9005 LOCATE 12, 12
```

```

PRINT "LOADING DATA..."
OPEN FILENAME$ + ".DAT" FOR INPUT AS #1
INPUT #1, Z1, Z2, Z3, Z4, Z5
FOR X = 1 TO 1000
  IF EOF(1) THEN GOTO 9008
  INPUT #1, Y0, Y1, Y2
  INTPD(X) = Y1
NEXT X
9008 INPUT "ARE YOU AT OSU-LAB PC (3) OR AT HOME (2)"; PC
IF PC = 2 THEN SCREEN 2
IF PC = 3 THEN SCREEN 3
IF PC <> 2 AND PC <> 3 THEN GOTO 9008
XPIXEL = 600
LISTNUM = X

9010 'THIS SECTION SMOOTHS THE DATA CURVE BY AVERAGING EVERY
CONSECUTIVE SET
'OF DATA. THE SIZE OF THE SET IS CHOSEN BY THE INPUT FOR NUM,
BELOW.

CLS
INPUT "ENTER NUMBER OF POINTS TO BE AVERAGED (ODD
NUMBER)"; NUM
LOCATE 12, 12
PRINT "SMOOTHING INT. PHOTODIODE DATA CURVE..."
FOR J = 0 TO LISTNUM / 2 STEP NUM
  SUM = 0
  FOR I = (J + 1) TO (NUM + J)
    SUM = SUM + INTPD(I)
  NEXT I
  NINTPD(J + (1 + NUM) / 2) = SUM / NUM
NEXT J

FOR J = 0 TO LISTNUM / 2 STEP NUM
  ARRAY = J + (1 + NUM) / 2
  DELTA1 = (NINTPD(ARRAY + NUM) - NINTPD(ARRAY)) / NUM
  FOR I = 1 TO (NUM - 1)
    NINTPD(ARRAY + I) = DELTA1 * I + NINTPD(ARRAY)
  NEXT I
NEXT J

I = 1
CLOSE #1
OPEN FILENAME$ + ".DAT" FOR INPUT AS #1
INPUT #1, PDLOW, PDHIGH, HIGHC, LOWC, RESONC

```

```

PDDIFF = PDHIGH - PDLOW
CLS
FOR X = 1 TO LISTNUM / 2
  IF EOF(1) THEN GOTO 100
  INPUT #1, DC, PDVALUE, RF
  PDOFFSET = (NINTPD(X) - PDLOW) / PDDIFF * XPIXEL
  IF PC = 2 THEN
    PSET (PDOFFSET, 190 - 100 * DC)
    PSET (PDOFFSET, 190 - 200 * RF)
  END IF
  IF PC = 3 THEN
    PSET (PDOFFSET, 330 - 200 * DC)
    PSET (PDOFFSET, 330 - 300 * RF)
  END IF
NEXT X
LOCATE 1, 1
PRINT "SMOOTHING PARAMETER="; NUM;
CLOSE #1: CLOSE #2

9100 IF PC = 3 THEN
  LINE (0, 312)-(600, 312)
ELSE
  LINE (0, 180)-(600, 180)
END IF
RESONC = (RESONC - PDLOW) / PDDIFF * XPIXEL
IF PC = 3 THEN
  LINE (RESONC, 311)-(RESONC, 313)
ELSE
  LINE (RESONC, 179)-(RESONC, 181)
END IF
CDIFF = HIGHC - LOWC
INTERVAL = CDIFF / 10
FOR I = 1 TO 601 STEP 60
  IF PC = 3 THEN
    LINE (I, 310)-(I, 314)
    LINE (I - 2, 314)-(I + 2, 314)
  ELSE
    LINE (I, 178)-(I, 182)
    LINE (I - 2, 182)-(I + 2, 182)
  END IF
NEXT I
LOCATE 24, 1: PRINT LOWC;
LOCATE 25, 32: PRINT "LASER CURRENT (mA)";
LOCATE 24, 72: PRINT HIGHC;
LOCATE 2, 1
9012 PRINT "PRINT SCREEN (P), OR ";

```



```

INPUT "REDO PLOT WITH DIFFERENT SMOOTHING PARAMETER (Y OR
N)"; Q$
IF Q$ = "P" THEN
  LOCATE 2, 1: PRINT "FILE: "; FILENAME$; "      ";
  PRINT "      ";
  FOR TIMMER = 1 TO 5000
  NEXT TIMMER
  BEEP: BEEP
  GOTO 9012
END IF
IF Q$ = "Y" THEN GOTO 9010
IF Q$ = "N" THEN
  CLS
  GOTO 10010
END IF
GOTO 9012

```

'STEP MOTOR...

```

6000  WAIT STATUS.REGISTER, COMMAND.WAIT
      OUT COMMAND.REGISTER, CDIOOUT
      WAIT STATUS.REGISTER, WRITE.WAIT, WRITE.WAIT
      OUT DATA.REGISTER, 0
      WAIT STATUS.REGISTER, WRITE.WAIT, WRITE.WAIT
      OUT DATA.REGISTER, BITTOTAL
      RETURN '6000

```

11111 END